ANALYSIS OF THE WAKE BEHIND A PROPELLER USING THE FINITE ELEMENT METHOD WITH A TWO-EQUATION TURBULENCE MODEL

by

Seung J. Kim

Dissertation submitted to the Faculty of the
Virginia Polytechnic Institute and State University
in partial fulfillment of the requirements for the degree of
DOCTOR OF PHILOSOPHY
in
Aerospace Engineering

APPROVED:

Dr. Paul Kaplan, Chairman

Dr. Joseph A. Schetz

Dr. Bernard Grossman

Dr. J. N. Reddy

Dr. Wayne L. Neu

July, 1988

Blacksburg, Virginia

ANALYSIS OF THE WAKE BEHIND A PROPELLER USING THE FINITE ELEMENT METHOD WITH A TWO-EQUATION TURBULENCE MODEL

by

Seung J. Kim

Dr. Paul Kaplan, Chairman

Aerospace Engineering

(ABSTRACT)

The finite element method in the form of the weak Galerkin formulation with the penalty function method was applied to several problems of axisymmetric turbulent flows including flow through a sudden pipe expansion, the stern region flow of a slender body, and flows past ducted and nonducted propellers in action. The coupled set of the Reynolds time-averaged Navier-Stokes equations and two turbulence transport equations for the turbulent kinetic energy and its rate of dissipation was solved by L/U decomposition and successive substitution with relaxation. An existing finite element code was modified with a low Reynolds number form for an appropriate treatment of wall influences on turbulence transport, which produces a better solution and provides an easier imposition of boundary conditions by solving up to wall with no slip boundary conditions. The two-equation turbulence model with the wall modification was first successfully tested by solving the turbulent flow through a sudden pipe expansion. The numerical simulation of the stern region flow of a streamlined body resulted in an excellent agreement with the measured data in terms of the mean-flow and turbulence quantities. Turbulent shear flows past a propeller at the rear end of the same slender body, modeled by an actuator disk, were successfully solved at two rotational speeds, self-propelled and 100% over-thrusted, using the same two-equation model. And finally,

comparisons of the wake behind a propeller were made for the self-propelled conditions of a ducted and nonducted propeller on the same streamlined body.

Acknowledgements

I would like to thank Dr. P. Kaplan for all the help and guidance he has given to me as the chairman of the advisory committee. I am much indebted to Dr. J. A. Schetz, who introduced me into the subject of turbulence. Without him this work could not have been completed. I owe a lot to Dr. B. Grossman for building up the theoretical and numerical sides of fluid dynamics through many invaluable lectures. Thanks are also due to Dr. J. N. Reddy for his excellent lectures on the finite element methods and to Dr. W. L. Neu for his valuable suggestions.

I wish to acknowledge the help and friendship from and , and a consultant at the computing center, . And I would like to thank all the graduate students for good days and bad days we shared together.

Special thanks should be given to my wife, and children, their patience and encouragement over many years. Thanks are due to my parents for their support and concern.

Table of Contents

List of Symbols

a ..... pipe radius

a_1 ..... empirical constant in Bradshaw's one-equation model

A_P ..... propeller disk area

B ..... computational domain occupied by fluid

C_1 ..... empirical constant in pressure-strain correlation term

C_2 ..... empirical constant in pressure-strain correlation term

c_D ..... empirical constant in Prandtl energy method

C_f ..... skin friction coefficient

c_S ..... empirical constant in diffusion term of Reynolds stress equation

C_{T0} ..... nominal thrust coefficient

C_{Th} ..... thrust disk loading coefficient

c_{Z1} ..... empirical constant in equation for length scale

c_{Z2} ..... empirical constant in equation for length scale

$c_{\varepsilon 1}$ ..... empirical constant in rate of dissipation equation

$c_{\varepsilon 2}$ ..... empirical constant in rate of dissipation equation

c_μ ..... empirical constant, 0.09

D ..... pipe diameter

D_0 ..... axisymmetric body diameter

D_{ij} ..... turbulence production tensor due to anisotropy

D_L ..... larger pipe diameter

D_P ..... propeller diameter

e ..... extra strain rate

f ..... frequency or external force

F ..... global load vector

f_1, f_2, f_μ ..... modification factors for $c_{\varepsilon 1}$, $c_{\varepsilon 2}$, c_μ

f_i ..... external force per unit mass in the x_i -direction

f_q ..... dimensionless body force due to propeller torque

f_t ..... dimensionless body force due to propeller thrust

f_{th} ..... thrust deduction fraction

f_x, f_r, f_θ ..... external force components per unit mass in cylindrical coordinates

H ..... step height

I ..... variational functional

k ..... mean turbulent kinetic energy per unit mass

K ..... stiffness matrix

K_{ij} ..... (i,j) component of stiffness matrix K

K_Q ..... torque coefficient

K_T ..... thrust coefficient

l_m ..... mixing length

L ..... length scale of large eddies or Laplacian operator

M ..... pressure-mass matrix

n ..... number of revolution of propeller per second or number of iteration

N ..... number of revolution of propeller per minute

n_i ..... direction cosine of unit vector normal to boundary

p ..... fluctuation part of pressure

P ..... time-averaged pressure

P_{ij} ..... turbulence production tensor due to anisotropy

P_k ..... production of turbulent kinetic energy

q ..... propeller torque per unit volume

Q ..... propeller torque

q_m ..... maximum value of radial distribution of propeller torque per unit volume

q_r ..... radial distribution of propeller torque per unit volume

Re ..... Reynolds number

R_i ..... gradient Richardson number

R_{ij} ..... Reynolds stress tensor

R_p ..... propeller radius

R_T ..... turbulent Reynolds number ($= \frac{k^2}{\nu \varepsilon}$)

r^* ..... nondimensional radial distance from wall

S ..... secondary source term in length scale equation or boundary enclosing B

t ..... time or propeller thrust per unit area

T ..... time interval or augmented thrust

T_0 ..... thrust in the absence of interaction

t_m ..... maximum value of radial distribution of propeller thrust per unit area

t_r ..... radial distribution of propeller thrust per unit area

t_x, t_r, t_θ ..... boundary traction vectors along x, r, θ directions

x_i ..... i-th componant in the Cartesian coordinates

U,V,W ..... velocity components

u_i ..... fluctuation part of velocity component in the x_i -direction

U_i ..... time-averaged velocity component in the x_i -direction

U_i' ..... instantaneous velocity component in the x_i -direction

U_x, U_r, U_θ ..... velocity components in cylindrical coordinates

U_∞ ..... mean velocity in free steam

u_* ..... friction velocity ($= \sqrt{\frac{\tau_w}{\rho}}$)

v' ..... root-mean-square value of v($= \sqrt{\overline{v^2}}$)

w_f ..... wake fraction

x, r, θ ..... cylindrical coordinates

x, y, z ..... Cartesian coordinates

y^+ ..... dimensionless normal distance from wall ($= \frac{u_*}{\nu} y$)

Z ..... variable in length scale equation or number of blades of a propeller

Greek Symbols

α ..... acceleration or relaxation parameter of successive substitution

Γ ..... radial distribution of circulation around propeller blade

δ ..... boundary layer thickness, or width of jet, or variational notation

δ_{ij} ..... Kronecker delta

Δ ..... global vector of unknowns

ε ..... rate of dissipation of turbulent kinetic energy

$\tilde{\varepsilon}$ ..... rate of dissipation variable for wall treatment

ε_{ij} ..... anisotropic rate of dissipation of turbulent kinetic energy

η ..... propeller efficiency

κ ..... von Karman constant, 0.41

λ ..... penalty parameter or Lagrange multiplier

μ ..... molecular viscosity of fluid

μ_t ..... turbulent or eddy viscosity

μ_∞ ..... fluid viscosity in free stream

ν ..... kinetic viscosity of fluid

ν_t ..... kinematic eddy viscosity

ρ ..... fluid density

σ_{ij} ..... stress tensor

σ_k ..... turbulent Prandtl number for diffusion of k

σ_Z ..... turbulent Prandtl number for diffusion of Z

σ_ε ..... turbulent Prandtl number for diffusion of ε

τ_w ..... wall friction

ϕ_I ..... interpolation function for velocity, k, and ε associated with node I

ϕ_{ij} ..... pressure-strain correlation

$\phi_{ij,1}$ ..... pressure-strain due to interaction of fluctuating velocities

$\phi_{ij,2}$ ..... pressure-strain due to interaction of mean strain and fluctuating velocities

ψ_I ..... interpolation function for pressure associated with node I

ω ..... vorticity

Subscripts

∞ ..... free stream condition

$*$ ..... nondimensionalized variable

Superscripts

$'$ ..... time derivative or instantaneous quantity

$\bar{}$ ..... vector notation

* ..... nondimensionalized quantity

1. INTRODUCTION

1.1 Description of Problem

Turbulent shear flows with significant swirling motion arise in many practical and interesting flows in mechanical and aero/hydrodynamic devices. They are present in flows over compressor and turbine blades of both radial and axial types; in the boundary layer on a spinning disc; in flow over a solid body with a propeller in motion; and in flow through a pump, etc. An analysis of a turbulent swirling flow over a streamlined body with a propeller operating, ducted or nonducted, can be very valuable, and it can be extended to a variety of practical engineering applications.

The analysis contains many important aspects that have to be considered: A propeller generates a strong wake and interacts with solid boundaries nearby; inviscid and turbulent flow regions are concurrent, which requires a large domain to stretch into the free stream region; turbulence modeling with treatments for the effects of solid

boundaries, swirling motion, and streamline curvature should be made; and a robust way to numerically solve the nonlinear elliptic system of equations is necessary.

The resultant velocity profile produced by a propeller should be appropriately predicted, so that it gives a good basis for obtaining an effective wake inflow which is crucial in designing ship propellers [1,2,3]. A ducted propeller interacts with its mounting system and nozzle and thus generates a complex flow situation. Fig. 1 shows the vortex system of a propeller in a nozzle diagrammatically. According to the Helmholtz theorem, the vortex lines must be closed, so that the vortex system has been completed with the starting vortices. The different vortices are indicated as follows:

Γ_p = bound vortices around propeller blades

Γ_d = bound vortex around nozzle ring

Γ_t = trailing helicoidal vortices from blade tips

Γ_b = trailing-boss vortex

These vortices generate turbulence which is transported downstream. But more importantly, the presence of a duct and wake downstream of the duct crucially affects the mean flow and turbulence fields. Other important aspects are a high accelerated motion past the propeller combined with a large pressure jump, flow entrainment from the free stream, and the interference between inviscid and turbulent flows. The region of turbulent flow is bounded by an inviscid flow, with the latter providing boundary conditions for the former.

To accomodate all these complex phenomena analytically it is a natural decision to adapt the Navier-Stokes equations while holding simplifying assumptions and approximations to a minimum. The incompressible Navier-Stokes equations are treated

by the Reynolds time-averaging process for the description of the equations of motion for turbulent flows. The time-averaging process produces new unknowns, called the apparent or Reynolds stresses, from the nonlinear convective term, which must be determined in some way to close the system of equations. The nonlinearity of the equations causes interactions between fluctuations of different wavelengths and directions, and, as a result, the wavelengths of the motion usually extend all the way from a maximum set by the width of the flow to a minimum set by the viscous dissipation of energy. The mechanism that spreads the motion over a large range of wavelengths is vortex stretching. Energy enters the turbulence if the vortex elements are aligned in the right sense to be stretched by mean velocity gradients. Naturally, the part of the motion that can best interact with the mean flow is that whose length scales are not too small compared to the mean-flow width, and this large-scale motion carries most of the energy and Reynolds stresses in the turbulence. The lifetime of the large eddies is long enough so that they may travel downstream for a distance many times the width of the flow. Therefore, the Reynolds stresses at a given position depend significantly on the upstream history, and are not uniquely specified by the local mean velocity gradient(s) as the viscous stress in laminar flows. This is why one needs transport equations to describe turbulence.

To account for the transport of the Reynolds stresses the $k-\varepsilon$ turbulence closure model can be utilized. This model is currently considered to be the best in predicting complex turbulent flows such as boundary layers, jets, wakes, and flows with pressure gradient, swirl, separation, heat transfer, and many three-dimensional flows[31,132-139]. This two-equation model is correct only at high Reynolds numbers, because the definition of the rate of dissipation is valid only when local isotropy prevails. Therefore, these raw equations cannot be directly applied to flows with solid boundaries. A

modification for the low Reynolds number region near a wall should be made[121,140]. Also, an abrupt large swirling component gives extra straining, and therefore the treatment for its effect should be included.

The success of the simulation for flows past a propeller depends largely on the proper discription of propeller effects. The momentum theory[4,5], lifting line theory[6-8], and variable-load actuator disk[9,10] have been used as mathematical models. In this study the actuator disk is used to model the propeller, which can avoid the periodic time-dependent, three-dimensional analysis when each blade is considered. The propeller is modeled by a disk with constant radius and thickness equal to the propeller radius and thichness. The thrust and torque are allowed to vary radially and arbitrarily, but which sum up to the global values of the total thrust and torque. This thrust and torque are converted into body forces, distributed appropriately into the actuator disk volume and acting at the location of the propeller[81-83].

The finite element method is, in principle, applicable to any well-posed equation set. Its general procedure is as follows: An approximate functional representation for each element variable is chosen. These approximations are then substituted into the governing equations in place of the original variables. This replacement produces a set of equations for the unknowns at nodal points. These approximate representations are then each multiplied by linearly independent set of weighting functions and integrated over the solution domain. The Galerkin approach, used in this study, is distinguished from other weighting methods by employing the same approximation functions in both the functional representation and the weighting functions. At least for a symmetric positive-definite system characterizing elliptic equation sets, this approach is known to produce the best solution from the chosen family of approximate solutions[11]. Using

this approach, one can select a nonuniformly graded computational mesh, seek solutions in irregular flow domains and avoid difficulties in applying boundary conditions.

FIDAP[12], a general purpose fluid dynamics code using the finite element method, was modified for the treatment of the wall and extra straining effects. To illustrate the performance of the $k-\varepsilon$ turbulence model with these modifications, four problems were solved and compared with available measurements. They are a flow through a sudden pipe expansion, the wake behind an axisymmetric slender body, and shear flows past a propeller, ducted and nonducted. It is hoped that this investigation will produce not only a good demonstration of the performance of the two-equation model, but also a few steps into future studies on general complex turbulent flow problems.

1.2 Literature Review

The survey and review of the previous work in the same field is of importance to computational investigations. Here four major topics are considered which are closely related to the content in this work:

1. flow over a sudden pipe expansion,
2. nonducted propeller,
3. ducted propeller,
4. finite element method applied to turbulent flow problems.

Each of these is now discussed in detail.

1.2.1 Flow through a Sudden Pipe Expansion

Flow through a sudden pipe expansion has drawn much interest of workers in the field of turbulence modeling. This specific problem, with the companion problem of a backward facing step, has not only many practical applications to sudden-dump combustion chambers, diffusers, buildings, airfoils with separation bubbles, and human vascular system, etc, but also many physically interesting features. The flow is suddenly separated from a wall and adjusts itself to newly found surroundings. It demonstrates the complicated nature in the reattachment region and its effect on the slow recovery to the ordinary boundary layer flow. A key feature of the flow is the splitting of the shear layer at reattachment, where one part of the flow is deflected upstream into the recirculating flow region to supply the entrainment; the other part continues downstream and is developed slowly.

Many workers have dealt with this separating, recirculating, and redeveloping flow problem. Experimental investigations for the flow over a sudden enlargement of pipe diameter were made by Back *et al.*[13] and Moon *et al.*[14]. The former was restricted to low Reynolds numbers. The latter successfully compared their predictions for the mean flow variables and reattachment distance with their measurements by solving the Navier-Stokes equations with the $k-\varepsilon$ turbulence model. They compared their measured reattachment distance with other investigations also[13,15,16]. The reattachment distance was shown to be consistantly between 6 and 9 step heights.

It was clearly demonstrated in the 1968 Stanford conference[17] that the boundary layer calculation methods would not cope with this flow around the separated and reattached regions, where the boundary layer approximation was violated. Since then,

most numerical investigations into the sudden pipe expansion problem have used the Navier-Stokes equations with the two-equation or higher-order model. Besides Moon, *et al.*'s numerical prediction, Smith applied the finite element formulation for the Navier-Stokes equations with the $k-\varepsilon$ or $q-f$ turbulence model to solve and to test his own two-equation model[18,19], where q denotes the square-root of k and f the characteristic frequency of large scale motion. He decoupled the two equations for the turbulence transport quantities from the mean flow equations. His alternating Newton-Raphson method experienced convergence difficulties. Chieng *et al.*[20] employed the $k-\varepsilon$ model of turbulence with a two-layer wall function method to simulate the flow and heat transfer in the separated flow region created by an abrupt pipe expansion. The calculated reattachment point was 8 step heights downstream of the expansion. A similar wall treatment was adapted by Amano[21,22] for the $k-\varepsilon$ model of turbulence to predict heat transfer in the separated flow region. The predicted reattachment distance was reported at around 7 step heights. Later, he utilized a Reynolds stress model[23] for the same problem and compared the predicted results of the $k-\varepsilon$ turbulence model with experimental data. To incorporate wall effects into the Reynolds stress model, the wall redistribution term was used for the low-Reynolds number form, which was proposed by Launder *et al.*[24]. It was shown that the inference of the necessity of using the Reynolds stress computations in this complex flow field, rather than the isotropic turbulence model of using the $k-\varepsilon$ model was weakened by a lack of substantial improvement in the predictions.

Flow over a backward facing step, physically similar to the flow past a sudden pipe expansion, has been an even more attractive problem to many workers. This problem has been investigated in many experiments[25-27] and by many numerical

predictions[28-35]. There are also good reviews for general two-dimensional separating and reattaching flows[25,36-38].

1.2.2 Nonducted Propeller

Early approaches to solving axisymmetric flow problems for the case of a propeller on a slender body aimed at the prediction of the effective wake inflow. The effective wake inflow is defined to be the apparent wake profile with propeller in operation minus the propeller-induced velocity profile. This effective wake profile is an important input to propeller design and is essential for the correct prediction of power, cavitation performence, and unsteady forces. The first theoretical attack to obtaining the effective wake inflow past a body of revolution was done by Nelson[39] in 1972, who developed a computer program to calculate the effective wake from the measured nominal wake and the static pressure distribution across the boundary layer. The nominal wake is the velocity profile at the location of a propeller in the absence of the propeller.

This was followed by Huang *et al.*[1-3], field over axisymmetric bodies using linearized potential theory and boundary layer approximations. They compared theoretical results with their own experimental data, and the agreement was satisfactory before separation occurred. In 1981, Huang and Groves[3] successfully predicted the effective wake of a propeller on axisymmetric bodies for five different cases using the same linearized theory.

In 1982, some related analysis work was applied in the process of propeller cavitation prediction[40]. The method of Huang and Groves was used to modify the circumferential mean velocity field. The assumed method predicts not only the

circumferential mean effective wake velocity, but also the amount of the contraction of the stream tubes which occurs forward of the propeller disk. The analysis produced curves of the effective wake in terms of radial distance and blade angles, and also obtained the Fourier coefficients of the harmonic series with respect to the blade angle.

The first attempt to solve the Navier-Stokes equations with turbulence modeling applied to the combination of a body and propeller was done by Schetz and Favin[41,42]. The stern-mounted propeller on a slender axisymmetric body was modeled as an actuator disk which could be arbitrarily arranged in space with arbitrary radial distributions of thrust and torque. The turbulence exchange processes were described by an integrated turbulent kinetic energy equation. The unsteady equations were cast in terms of vorticity and a stream function. Since an unsteady formulation was employed to develop a desired steady-state solution, the number of iterations to get the converged solution was shown to depend very much on the initial guess. Their prediction was compared with experimental data measured by Schetz and Jakubowski[43], who made extensive measurements for the turbulent intensities and the Reynolds stresses for three cases: 1) pure drag body, 2) self-propelled by axial fluid injection, and 3) self-propelled by a propeller. All of their cases are for an identical axisymmetric fore-body.

The predictions revealed several shortcomings as listed below:

1) The details of the near-wall region of the body boundary layer were not treated explicitly because the propeller was assumed to dominate the flow development.
2) The predicted average values of the turbulent kinetic energy at two locations were about 35% higher than the measured values.

3) The computed axial velocity distribution obtained at two propeller diameter downstream was found to be good, but showed discrepancy near the axisymmetric line.

4) The absolute level of the maximum swirl velocity predicted was low.

5) An integrated form of the turbulent kinetic energy equation does not account in detail for the radial transport of the turbulent kinetic energy and the Reynolds stresses.

As a result of all of these, a suggestion of a more elaborate model for turbulence transport including wall and swirl effects was made.

Recently, Thomas[83] solved the three-dimensional, incompressible Navier-Stokes equations for the predictions of wake field downstream of a propeller-driven slender body with an appendage on top. The turbulence transport was modeled by the integrated turbulent kinetic energy model for an inner boundary layer, the mixing-length model for an outer boundary layer, and a planar wake model. Slip condition was imposed on the body surface. Actuator disk theoty was used for modeling a propeller, which radially distributed the equivalent body forces on the propeller volume. Predictions resulted in a good agreement with measurements[198]. However, they showed some room for improvement near wall region.

1.2.3 Ducted Propeller

A ducted propeller is essentially an ordinary propeller, which is enclosed circumferentially by a thin circular fairing whose cross section along the principal direction is of an airfoil shape. The diameter of the fairing is usually considerably

smaller than that of the corresponding normal propeller with similar performance, and the number of blades is increased. Through the effect of the duct wall, the occurrence of the trailing vortices at the blade tips is restricted or even avoided for a sufficiently small clearance between blade tips and the duct.

The first serious experiments on a ducted propeller were made in Italy by L. Stipa[44] in 1931. He conducted systematic wind tunnel tests which indicated the benefits to be gained by shrouding propellers for static operation and low speed flight. For some reason, however, credit for the invention of a ducted propeller has generally been given to Kort[45] in Germany in 1934. In fact, the ducted propeller is frequently referred to as the "Kort nozzle" if it accelerates flow.

Since the 1930's, interest in the ducted propeller has become more widespread. By choosing the proper type of duct, the velocity at a propeller can be increased(Kort nozzle) or decreased(pump-jet). The first type is used for thrust augmentation of heavily loaded propellers, e.g., in hovering flight and V/STOL aircraft, and in tugs, pushboats, and trawlers. The second is also widely used for increasing Mach number of the propeller in air and for increasing cavitation inception speed for a propeller in water. For naval ships a reduction in noise level can be obtained which may be of importance for tactical reasons.

Theoretical investigations of ducted propellers have been concentrated to a large extent on the linearized theory for an axisymmetric duct in a uniform flow[46,47]. In the design process, the propeller and duct are treated separately, and a process of iteration is used to obtain the mutual interaction. For the linearized theory[48,49], the following assumptions were generally made:

1) The fluid is inviscid and no separation occurs on the duct.

2) The duct can be represented mathematically by a distribution of ring vortices and ring sources along a cylinder of constant diameter.

3) The trailing vortex system of the duct, if it exists, has the constant diameter of the duct and extends to infinity.

These foregoing assumptions apply only to the duct. The propeller alone is modeled by either the momentum theory, lifting line theory, or an actuator disk.

There were a few investigations of the nonlinear theory of ducted propellers which were applied to the duct only and not to the propeller. A nonlinear approximation, based on the second-order airfoil theory, was tested by Morgan[50], Chaplin[51], and Meyerhoff[52]. Some difficulty was reported in obtaining solutions for arbitrary duct shapes with the numerical approximations of the type used by Chaplin and Meyerhoff.

The theoretical predictions have been satisfactory if no separation occurs on the duct and if viscous effects are negligible. The nonlinear theory has been known better than the linearized theory[48]. Very recently, the panel method was applied to a problem of two-dimensional hydrofoil, a propeller with hub and axisymmetric duct in uniform flow [53].

1.2.4 Finite Element Method for Turbulent Flows

In the past, the numerical solution of the Navier-Stokes equations has mainly been achieved by the finite difference technique. The alternative finite element method, well proven in the structural mechanics field, has certain advantages over the finite difference

methods. These are the ease with which irregular geometries, non-uniform meshes, and imposition of appropriate boundary conditions can be applied. Numerous successful attempts have been made to solve the Navier-Stokes equations for a variety of laminar flows by the finite element method[54-63]. Theoretical aspects are well discussed in references[11] and [63-66].

The application of the finite element method to the Navier-Stokes equations for turbulent flows is relatively new. It has been pursued by several groups. A group of workers at Swansea, U. K., used the finite element method to solve both fully developed and developing turbulent flows in pipes[67]. A modified Van Driest model for effective viscosity was used and a logarithmic element was developed for use near a wall region, such that the element shape function depicted a typical velocity profile in this region. The results with the special element compared favorably with experimental results, but the use of conventional elements resulted in appreciable errors. This problem was solved again by adapting a wall damping function near the wall[68].

The same group used the mixing-length model for the simulation of turbulent coaxial jet flow. The results of the finite element analysis compared favorably with the results of experiment and of a finite difference method. They found that the empirical determination of a length scale was difficult, and therefore eliminated the need to specify the length scale by implementing the transport equations for k and kl into the same finite element code, where k is the turbulent kinetic energy and l is the characteristic length scale. This two-equation model was successfully applied to fully developed pipe and channel flows. A similar approach, based on the mixing length model, was utilized for the formulations of the boundary layer and the Navier-Stokes equations for the prediction of the wake behind a prolate spheroid[69]. The latter formulation produced

better agreement with experimental data than the former. This was probably due to the fact that the inflow boundary was located at the stern of the body where the validity of the boundary layer approximation was questionable. The application of the same $k-kl$ model to fully developed pipe flow was presented in reference[70]. The general formulation for k and $k-kl$ models was reviewed in the paper. The predictions of the one- and two-equation models do not show notable difference in the mean flow quantities. This is due to the use of a very accurate expression for the length scale in the pipe flow.

In reference[71] it was illustrated that the finite element method can be used to analyze turbulent flows, in the presence of a prescribed pressure gradient, by means of the two-equation model by solving the boundary layer equations for a fully developed channel flow and a plane mixing layer. Mean flow variables and turbulent intensity compared favorably with experiments. However, convergence difficulties were experienced and the iteration scheme of the underrelaxed successive substitution was essential to ensure convergence.

Recirculating flow downstream of a backward facing step by the finite element method was analyzed with the one-equation model and the Navier-Stokes equations [35]. The effect of streamline upwind was investigated for both laminar and turbulent flows. It was claimed that the use of upwind elements was necessary for some laminar flow problems, but that their use was not required in the turbulent flow regime. The same authors employed the $k-\varepsilon$ model to solve the same problem[33,34]. A special treatment of the wall shear stress near the reattachment point required a priori knowledge of the location of this point. The model was found to be underpredictive with regard to the

reattachment distance although the velocity distribution and the turbulent kinetic energy were predicted within a reasonable agreement.

Baker *et al.* at the University of Tennessee is one of the very active groups of using the finite element method for turbulent flows. Three-dimensional, steady, Reynolds time averaged Navier-Stokes equations for compressible heat-conducting fluid are parabolized by deleting the diffusion terms parallel to the direction of the incoming flow[72]. A general statement of the finite element solution algorithm was derived, based on the Galerkin weighted residual and on an implicit integration algorithm. The Poisson equation for pressure is cast into complementary and particular parts[73], yielding an iterative interaction algorithm formulation. Accuracy and convergence of the algorithm were extensively tested for many problems. They applied their algorithm with good agreement to predict the perturbation velocity field around an airfoil[72,74], turbulent boundary layer flow[75], flow past an airfoil trailing edge[76], and three-dimensional subsonic V/STOL jet in a cross flow[77], all using the $k-\varepsilon$ turbulence model with a damping function for the wall treatment. The parabolized formulation of the Navier-Stokes equations was also utilized for turbulent boundary layer flows with the use of the mixing length model and for three-dimensional turbulent flow in a square duct with the use of the algebraic Reynolds stress model[78]. Qualitative agreement was reported for the flow in the square duct.

Smith and Sutton at Berkeley, U. K., used the Van Driest eddy viscosity to solve fully developed and developing pipe flows[79]. The linear element was found to be satisfactory in the analysis of the fully developed flow, but it gave rise to an oscillatory behavior in the axial velocity and wall shear stress in the developing flow. This instability could be eleminated by adapting a quadratic rather than a linear streamline

variation in effective viscosity. Later, they solved the fully developed pipe flow using the $k-\varepsilon$ model with a wall function method[80]. An inconveniently good initial guess was found necessary to achieve the convergence of the Newton-Raphson method. Extension to more complicated flows was attempted in reference[18], where the recirculating flow in a sudden pipe expansion was explored. The convergence difficuty experienced with the Newton-Raphson method was reported again.

An alternative two-equation turbulence model, the $q-f$ model, was suggested by Smith[19], which was designed to overcome the difficulty reported in reference[18]. Here q is the square-root of k and f is the characteristic frequency of large scale motion which can be interpreted also as the vorticity of large scale eddies. The agreement with experiment was shown better for the sudden pipe expansion. However, the existence of a real solution for q and f on any node, for any grid and any set of boundary conditions, could not be guaranteed.

Schetz *et al.* at Virginia Tech have concentrated mainly on the three-dimensional turbuent flow past a propeller. In reference[81] the Navier-Stokes equations are solved for the simulation of the three-dimensional flow past a propeller in a shear flow. Turbulence transport was modeled by an integrated turbulent kinetic energy eqation[82] and the actuator disk theory was used for modeling the propeller. Mean flow quantities compared favorably with measured data. The prediction of swirl component was a major improvement over the same kind of previous analyzes[7,41,42]. Later in reference[83] the above method was modified for the prediction of wake field from a propeller-driven slender body with an appendage on top. The turbulence model included the integrated turbulent kinetic energy model for an inner boundary layer, the

mixing-length model for an outer boundary layer, and a planar wake model. Good correlation of the theory with the measurements was reported[83]

One other notable group in this area is Larock and Schamber at the Univeristy of California in Davis, California. In reference[85] the steady Navier-Stokes equations , treated by the Galerkin weighted residual precedure, were solved for fully developed channel and pipe flows. Two $k-\varepsilon$ turbulence models, proposed by Hanjelic and Launder[86] and Gibson and Launder[87], were compared with measurements and finite difference solutions. Wall boundary conditions were applied at the edge of the turbulent flow regime away from the wall. The Hanjelic and Launder model results compared better with Hanjelic and Launder's experiments and the finite difference solution than the Gibson and Launder model. However, both models revealed some discrepancy in turbulence parameters. Later the same authors extended their applicaiton of the $k-\varepsilon$ model to the determination of the flow pattern in a circular sedimentation basin. The performance of the Newton method, in combination with the flip-flop method between two sets of equations for mean variables and turbulence transport quantities, was shown to be very sensitive to the closeness of an initialization vector to the ultimate solution vector. They closed with a suggestion of three other solution schemes that would offer some intriguing possibilities as replacement candidates for the Newton method.

2. TURBULENCE MODELING

In turbulent flow, studies we have a complete set of the equations of motion, the Navier-Stokes equations, which can describe the motion of fluid flows at any instant of time. But, the full three-dimensional, time-dependent equations for turbulent flows cannot be solved numerically with present computer facilities. For engineering purposes, the instantaneous values may not be nesessary, and therefore time-averaged values and global descriptions for the flow characteristics are sought. However, the time-averaging process eliminates some of the information to be contained in the Navier-Stokes equations and increases the number of unknowns larger than the number of equations by substituting the apparent Reynolds stresses for the actual transfer of momentum due to the velocity fluctuations. Now, the problem is how to supply the information lost during the time averaging for the time-averaged Reynolds equations. The Reynolds stresses, $-\rho\,\overline{u_i u_j}$, should be modeled in a proper way that the missing information be recovered. A transport equation for each of the Reynolds stresses can be constructed, but this only increases the unknowns, and the set of equations would not be closed in this way. An alternative is to use a finite number of equations and supply the missing

information from experiments. This makes the basis of the turbulence transport modeling.

2.1 *Reynolds Time-Averaged Navier-Stokes Equations*

The governing differential equations for the mean quantities of incompressible turbulent flows, the following Reynolds time-averaging process[88-93], are expressed in terms of tensor notation:

continuity equation

$$\frac{\partial U_i}{\partial x_i} = 0 \tag{2.1}$$

momentum equations

$$\frac{\partial U_i}{\partial t} + U_j \frac{\partial U_i}{\partial x_j} = -\frac{1}{\rho} \frac{\partial P}{\partial x_i} + \frac{\partial}{\partial x_j}(\nu \frac{\partial U_i}{\partial x_j} - \overline{u_i u_j}) + f_i \tag{2.2}$$

Here, the quantities of the capital letters indicate the time-averaged values, which are defined as

$$U_i \equiv \lim_{T \to \infty} \frac{1}{T} \int_{t_0}^{t_0+T} U_i'(\vec{x}, t)\, dt \tag{2.3}$$

while the instantaneous velocity component in the x_i – direction, U_i', is decomposed as

$$U_i' = U_i + u_i \tag{2.4}$$

where u_i is the fluctuation quantity in the same direction. Pressure is also decomposed similarly. The Reynolds equations are an exact description of the mean flow quantities since no assumption has been made in deriving them. However, the equations cannot be solved as they are because of the correlations of the fluctuating velocities, $\overline{u_i u_j}$, which must be considered as new unknowns. It should be noted that the turbulence correlations come from the convective derivative of the momentum equations during the averaging process. Physically, these correlations, multiplied by the density ρ, represent the transport of momentum by turbulent fluctuations; they act similar to stresses on the fluid and are, therefore, called the apparent turbulent or Reynolds stresses. The term $-\rho\overline{u_i u_j}$ is the transport of the x_i-momentum in the direction x_j or vice versa.

To proceed further, the new unknowns must be determined in some way. Exact transport equations can be derived for $\overline{u_i u_j}$, but these equations include turbulence correlations of the next higher order. Therefore, the equations cannot be closed in this way. A turbulence model must be introduced which makes assumptions regarding the relationships between the turbulence correlations and the time-mean flow variables. These relationships may be expressed as differential and/or algebraic equations which together with the mean flow equations, (2.1) and (2.2), form a closed set of equations. This need has spurred the development of numerous mathematical models for turbulent flows, especially

in the past two decades; review of these modeling efforts describing the several major approaches and different levels of complexity should refer to references[94-105].

2.2 *Eddy-Viscosity Concept*

The concepts of various models can be classified into the eddy viscosity models, the Reynolds stress models, and the large eddy simulations. The main features that distinguish models come from the particular closure technique that expresses the modeled quantities in terms of the mean velocity field, the mean turbulent field, or the large eddy structures as well as the small scale turbulence.

The eddy viscosity concept was originated at the suggestion of Boussinesq[107]. It assumes that the turbulent stresses are the products of an effective viscosity and the mean velocity gradients. In general, for high Reynolds number flows this idea is expressed as

$$-\overline{u_i u_j} = \nu_t \left(\frac{\partial U_i}{\partial x_j} + \frac{\partial U_j}{\partial x_i}\right) - \frac{2}{3} k \delta_{ij} \tag{2.5}$$

where k denotes the turbulent kinetic energy , and the effective viscosity, ν_t, is the turbulent or eddy viscosity, which is not a fluid property but a field variable. The eddy viscosity is interpreted as being a product of the local length scale and the local velocity scale characteristic of the large scale turbulent motion. Hence, the eddy viscosity can be written as

$$\nu_t \sim v' L \tag{2.6}$$

where $v' (= \sqrt{\overline{v^2}})$ is the root-mean-squared transverse fluctuation velocity with which the eddies move in relation to the surrounding fluid.

The subtraction of the second part of Eq. (2.5) assures that the sum of the normal stresses is equal to $2k$. It is necessary to make the expression valid also for the normal stresses. When $i = j$ for an incompressible fluid,

$$\overline{u_i u_i} = -2\nu_t \frac{\partial U_i}{\partial x_i} + 2k = 2k \tag{2.7}$$

hence

$$k = \frac{1}{2}\overline{(u_1^2 + u_2^2 + u_3^2)} \tag{2.8}$$

Eq.(2.7) indicates that the summation of all the normal stresses, which substantially act like the pressure force, is twice the turbulent kinetic energy. The expression for $\overline{u_i u_j}$ in Eq.(2.5) is used to replace $\overline{u_i u_j}$ in the momentum equation, and the turbulent kinetic energy term is implicitly added to the pressure gradient term so that the static pressure effectively becomes $P + \frac{2}{3}k$. Therefore, the appearence of k in Eq.(2.5) does not necessitate the determination of k.

There can be many kinds of closure models with Boussinesq's idea according to the way of determination of the velocity and length scales. They are often referred to as the zero-, one-, and two-equation models in reference to the number of the supplementary transport equations used for closure. The zero-equation models are those that rely on specifying the velocity and length scales in terms of the mean flow quantities. The one- and two-equation models obtain the velocity scale from a solution of the modeled form of the turbulent kinetic energy equation, and a specified length scale in the one-equation approach or a solution of the modeled length scale equation in the two-equation approach.

2.3 *Turbulence Closure Models*

2.3.1 Zero-Equation Models

In 1925 Prandtl[107] suggested the mixing-length hypothesis similar to the mean free path of the kinetic gas theory[89,90]. He explained that velocity fluctuations are induced by the transverse motion due to the axial momentum difference as

$$v' = \sqrt{\overline{(v^2)}} \sim l_m \left| \frac{dU}{dy} \right| \tag{2.9}$$

Hence the velocity correlation is expressed as

$$-\overline{uv} \sim l_m^2 \left| \frac{dU}{dy} \right| \frac{dU}{dy} \tag{2.10}$$

where the sign of $-\overline{uv}$ is determined by that of dU/dy. Since the Reynolds stresses are expressed in terms of only the mixing length and the local mean velocity gradient, the resultant governing equations use partial differential equations only for the mean flow variables and no transport equations for the fluctuating quantities. This, with an algebraic eddy viscosity model, is so-called the mean flow model.

These models assume that the flow is in local equilibrium or nearly in a state of self-preservation and that the turbulence is isotropic. A self-preserving flow is one in which the profiles of mean velocity and of other quantities like the Reynolds stresses, when measured from a suitable origin, are geometrically similar at all streamwise positions. Turbulent flows usually take up the self-preserving forms if the boundary

conditions allow. For instance, the outer region of the boundary layer on a flat plate at high Reynolds number is very close to the self-preservation with

$$\frac{U - U_\infty}{u_*} = f_1(\frac{y}{\delta})$$
$$\frac{\tau}{\tau_w} = f_2(\frac{y}{\delta}) \tag{2.11}$$

where the boundary layer thickness δ is a function of x and u_* is the friction velocity($= \sqrt{\frac{\tau_w}{\rho}}$). These expressions and the definitions of the eddy viscosity and the mixing length give

$$\frac{\nu_t}{u_* \delta} = f_3(\frac{y}{\delta})$$
$$\frac{l_m}{\delta} = f_4(\frac{y}{\delta}) \tag{2.12}$$

By local equilibrium, it is meant that the turbulent kinetic energy is dissipated at the same rate as it is generated, so that there cannot be any influence of the turbulent fluctuations at other points or at earlier times at the same point in the flow. The logarithmic part of the inner region of a boundary layer in pressure gradient and at any Reynolds number is close to local equilibrium where the only relevant length scale is y. In this case

$$\nu_t = \kappa u_* y$$
$$l_m = \kappa y \tag{2.13}$$

But, these simple formulae for ν_t and l_m are the results solely of the dimensional analysis. Any dimensionally-correct theory with a disposable constant would give the same results irrespective of its physical correctness.

The zero-equation models are valid only when the convective and diffusive transports are neglible as in the local equilibrium flow, Eq.(2.13), or when the ratio of the generation or destruction of the Reynolds stress is a function of $\frac{y}{\delta}$ only as in the self-preserving flow, Eqs.(2.11)-(2.12). The simple behavior of the eddy viscosity and mixing length in a simple, thin shear layer is not maintained in more complicated cases like multiple shear layers, flows with a significant extra rate of strain, recirculating flows, and three-dimensional flows.

An attempt to obtain a generally valid relation for the mixing length to maintain nonzero shear stress with zero velocity gradient was made as von Karman's similarity hypothesis[108], which is based on the supposition that the structure of the turbulent motion is similar everywhere and that the length scale at any point is determined by the distribution of the mean velocity in the immediate neighborhood of the point. With these assumptions, the relation

$$l_m = \kappa \left| \frac{\partial U/\partial y}{\partial^2 U/\partial y^2} \right| \tag{2.14}$$

was derived for the mixing length in a two-dimensional mean shear flow, where κ denotes an empirical constant. This formula agrees with experiments for flows near the wall, but it has no general validity. In jets and wakes the velocity profiles have inflection points so that Eq.(2.14) yields an infinite mixing length. Little use has, therefore, been made of von Karman's formula.

There have been several attempts to improve the algebraic eddy viscosity model to account for extra strain, but these attempts have had limited success. Bradshaw[109]

made corrections for the length scale for flows with streamline curvature or with buoyancy, which are given by

$$\frac{L}{L_0} = 1 + \frac{\beta e}{\partial U/\partial y} \tag{2.15}$$

for the curved flows and

$$\frac{L}{L_0} = 1 - \beta R_i \tag{2.16}$$

for the bouyancy. Here L_0 is the length scale of a simple shear layer, β an empirical constant, e the extra strain rate, and R_i the gradient Richardson number. For example, $e = 2U/R$ for flows with a longitudinal curvature R and $e = 2\omega$ for flows with a rotation. A detailed discussion is given in Bradshaw[110].

An extention to three-dimensional flows was carried by Rotta[111]. He wrote

$$\begin{aligned} -\overline{uv} &= \nu_t\left(a_{xx}\frac{\partial U}{\partial y} + a_{xz}\frac{\partial W}{\partial y}\right) \\ -\overline{vw} &= \nu_t\left(a_{xz}\frac{\partial U}{\partial y} + a_{zz}\frac{\partial W}{\partial y}\right) \end{aligned} \tag{2.17}$$

where $a_{xx} = 1 - (1 - T)\sin^2\beta$, $a_{xz} = (1 - T)\sin\beta\cos\beta$, $a_{zz} = 1 - (1 - T)\cos^2\beta$, and T is a prescribed constant, and $\tan\beta = W/U$. This model has been used by Cousteix and Mueller[112] for a three-dimensional shear flow. The model has not been very successful; the value of T had to be varied from one flow to another for a good prediction.

Nakkasyan and Rhyming[113,112] have introduced an anisotropic eddy viscosity model for three dimensional flows, given by

$$-\overline{uv} = \nu_t E_s(\frac{\partial U}{\partial y}), \qquad -\overline{vw} = \nu_t E_n(\frac{\partial W}{\partial y}) \tag{2.18}$$

where E_s and E_n are functions of the mean velocity shear stresses and the curvature of the streamline.

2.3.2 One-Equation Models

2.3.2.1 Prandtl energy method

The simplest models accounting for the transport and history effects of turbulence use a transport equation for a suitable velocity scale of the turbulent motion. Generally, $\sqrt{k}$ is taken as such a scale, where k is the turbulent kinetic energy per unit mass, which is a good measure of the intensity of the turbulent fluctuations in the three directions. Kolmogorov[114] and Prandtl[115] used this velocity scale with the eddy viscosity concept, which is expressed as

$$\nu_t = c_\mu \sqrt{k}\, L\,, \tag{2.19}$$

where c_μ is a constant which needs to be determined empirically, and L is a length scale similar to, but not equal to, the mixing length l_m. The equation for the turbulent kinetic energy is obtained by multiplying the Navier-Stokes equations by the three fluctuation components of velocity respectively and then taking average and summing with the use of the continuity of Eq.(2.1). This equation reads as

$$\frac{\partial k}{\partial t} + U_i \frac{\partial k}{\partial x_i} = -\frac{\partial}{\partial x_i}\left[\overline{u_i(k + \frac{p}{\rho})}\right] - \overline{u_i u_j}\frac{\partial U_i}{\partial x_j} - \nu \overline{\frac{\partial u_i}{\partial x_j}\frac{\partial u_i}{\partial x_j}} \qquad (2.20)$$

The terms in the left-hand side are the time rate of change and the convective derivative of the turbulent kinetic energy. The first term in the right-hand side is the diffusive transport term due to velocity and pressure fluctuations. The second, $-\overline{u_i u_j}\frac{\partial U_i}{\partial x_j}$, the only term connecting the mean motion and the fluctuating motion, is the production term. Large eddies obtain energy from the mean shearing motion and supply energy to smaller eddies, which lose energy to even smaller eddies in their turn, and so on until the eddies are so small that they lose so much energy by direct action of viscous stresses that no smaller eddies can be formed. The last term in the right-hand side is the rate of energy dissipation lost by the smallest eddies.

With the diffusion and the dissipation terms modeled and with the eddy-viscosity formula, the turbulent kinetic energy equation becomes

$$\frac{\partial k}{\partial t} + U_i \frac{\partial k}{\partial x_i} = \frac{\partial}{\partial x_i}\left(\frac{\nu_t}{\sigma_k}\frac{\partial k}{\partial x_i}\right) + \nu_t\left(\frac{\partial U_i}{\partial x_j} + \frac{\partial U_j}{\partial x_i}\right)\frac{\partial U_i}{\partial x_j} - c_D \frac{k^{3/2}}{L} \qquad (2.21)$$

where σ_k is a turbulent Prandtl number of order 1 and c_D is an empirical constant of the same order. The equation (2.21) is valid only for high Reynolds numbers. Values of the empirical constants, $c_\mu c_D \simeq 0.8$ and $\sigma_k = 1$, were suggested by Launder and Spalding[91].

2.3.2.2 Bradshaw et al's model

In 1967 Bradshaw *et al.*[116] developed an one-equation model for two-dimensional flows which does not employ the eddy-viscosity concept. Their model converts the

turbulent kinetic energy equation into a differential equation for the turbulent shear stress. They made assumptions that the turbulent intensity is directly proportional to the local shear stress, and that the energy diffusion is also directly proportional to the local shear stress with a factor depending on the maximum value of the shear stress, and also that the dissipation rate is determined by the local shear stress and a length scale depending on $\frac{y}{\delta}$ which is similar to the assumption made by Prandtl. The modeled equation is

$$U\frac{\partial}{\partial x}\left(\frac{\overline{uv}}{a_1}\right)+V\frac{\partial}{\partial y}\left(\frac{\overline{uv}}{a_1}\right)=-\sqrt{\overline{uv}_{\max}}\,\frac{\partial}{\partial y}(G\,\overline{uv})+\overline{uv}\,\frac{\partial U}{\partial y}-\frac{\overline{uv}^{3/2}}{L} \tag{2.22}$$

where

$$\begin{aligned} a_1 &= \frac{\overline{uv}}{k}\simeq 0.3 \\ G &= \frac{\sqrt{(\overline{uv})_{\max}}}{U_l}f_1\left(\frac{y}{\delta}\right) \\ \frac{L}{\delta} &= f_2\left(\frac{y}{\delta}\right) \end{aligned} \tag{2.23}$$

This model was intended only for wall boundary layer flows; whence the approxmations made in the derivation of the equation are (i) the boundary-layer approximation, which implies that there is no pressure gradient normal to the wall and (ii) that a_1, L, and G change much more slowly than $\overline{uv}$ and U in the primary direction, so that they can be regarded as well-behaved coefficients rather than variables, which is supposed to be true in the boundary layer before separation. It should be noted that they did not employ the gradient-diffusion form, $\frac{\partial^2\overline{uv}}{\partial y^2}$, but the present form of the first term on the right hand side of Eq.(2.22), which renders the system of equations for the mean motion to

become hyperbolic. Therefore, the method of characterics is used to solve reduced ordinary differential equations containing gradients along the characteristic lines.

The model works fairly well in many wall boundary-layer calculations. But it does not work for jets and wakes and even for wall bounded shear flows through channels and pipes, where $\frac{\overline{uv}}{k} = 0.3$ is not true, since $\overline{uv}$ changes its sign somewhere in the flow region. This model is only for unconfined wall boundary layer flows.

2.3.2.3 General features

Conceptual advantages of the treatment of the transport and the history effects in one-equation models over the zero-equation models are nullified because the length scale L appearing in Eqs. (2.21) and (2.22) is usually determined empirically as the mixing length l_m. This empirical specification works quite well for many simple shear flows. In complex flows, however, L is equally difficult to prescribe as the mixing length l_m. Therefore, the application of the one-equation models is restricted mainly to simple shear flows. And the empirical constants, c_μ and c_D, contained in the Prandtl energy equation are applicable only to flow regions with high Reynolds numbers locally. Hence, they are not valid very near the wall and the introduction of the wall functions is inevitable. Hassid and Poreh[117] and Reynolds[96] have proposed low Reynolds-number versions for Prandtl's and Bradshaw *et al.*'s one-equation models that allow an integration right to the wall. Their modications suffer from either poor predictions or additional restrictions.

Generally speaking, one-equation models do not show better performance than the zero-equation models in predicting general complex flows even with additional

computational effort. For simple flows, the zero-equation models work as well as the one-equation models do. Hence, most workers have abandoned the one-equation model in favor of the two-equation or Reynolds-stress models.

2.3.3 Two-Equation Models

The length scale of a turbulent motion is subject to the transport and history processes in a similar way to the turbulent kinetic energy. In order to account for these processes and to turn around the difficulties in finding generally valid formulae for prescribing or calculating L, several models were suggested that use a transport equation for the length scale. However, the variable need not necessary be the length scale itself; any combination with k will suffice, since k can be determined by the transport equation for k. The equation for the variable, say Z, which is a function of k and L,

$$\frac{\partial Z}{\partial t} + U_l \frac{\partial Z}{\partial x_l} = \frac{\partial}{\partial x_l}\left(\frac{\sqrt{k}\,L}{\sigma_z} \frac{\partial Z}{\partial x_l}\right) + c_{z1} \frac{Z}{k} P_k - c_{z2} Z \frac{\sqrt{k}}{L} + S \quad (2.24)$$

where σ_z, c_{z1} and c_{z2} are empirical constants, P_k is the production of the turbulent kinetic energy defined in Eqs.(2.20) and (2.21), and S represents a secondary source term which is different according to the choice of Z.

The earliest and least used equation is for a frequency ($=\sqrt{k}/L$) by Kolmogorov[114]. Chou[118], Davidov[119], Harlow and Nakayama[120], and Jones and Launder[121] suggested an equation for the dissipation rate $\varepsilon(=k^{3/2}/L)$. Rotta[122] proposed an equation for kL, which was used later by Rodi and Spalding[123] for free jets and by Ng and Spalding[124, 125] for boundary layers near the wall. A $k-\omega$ model,

where ω is the turbulence vorticity density ($\omega^2 = k/L^2$), was suggested and tested by Spalding[126] and Gibson and Spalding[127]; a similar model was proposed independently by Saffman[128] for an inhomogeneous flow, which was modified later for generality[129,130]. Smith[19] proposed and tested the $q-f$ model with a flow through a sudden pipe expansion, where q and f are a square-root of the turbulent kinetic energy and a frequency, respectively. The terms in the equations for different $Z's$ may be considered to be equivalent to the terms in Eq.(2.20), except the diffusion term and the secondary source term which is important only near the wall. Thus, the main difference rests on the diffusion term. Launder and Spalding[131] claimed that the difference is unimportant in free shear flows, but that near the wall the gradient assumption for the diffusion term with a single constant appears to work better for $Z = \varepsilon$ than for any other variable. Furthermore, it is easier to apply wall boundary conditions with the $\varepsilon-$ equation which will be discussed later. For these reasons, the $\varepsilon-$ equation has been considerably more popular than any other length scale equation.

The modeled equations for k and ε are

$$\frac{\partial k}{\partial t} + U_i \frac{\partial k}{\partial x_i} = \frac{\partial}{\partial x_i}\left(\frac{\nu_t}{\sigma_k} \frac{\partial k}{\partial x_i}\right) + \nu_t \left(\frac{\partial U_i}{\partial x_j} + \frac{\partial U_j}{\partial x_i}\right) \frac{\partial U_j}{\partial x_i} - \varepsilon \qquad (2.25)$$

$$\frac{\partial \varepsilon}{\partial t} + U_i \frac{\partial \varepsilon}{\partial x_i} = \frac{\partial}{\partial x_i}\left(\frac{\nu_t}{\sigma_\varepsilon} \frac{\partial \varepsilon}{\partial x_i}\right) + c_{\varepsilon 1} \frac{\varepsilon}{k} P_k - c_{\varepsilon 2} \frac{\varepsilon^2}{k} \qquad (2.26)$$

where P_k is the production of the turbulent kinetic energy defined as the second term on the right hand side of Eq.(2.25). To close the equations the Kolmogorov-Prandtl relation is again utilized. Since $\varepsilon = k^{3/2}/L$,

$$\nu_t = c_\mu \frac{k^2}{\varepsilon} = c_\mu \sqrt{k}\, L \qquad (2.27)$$

which is identical to Eq.(2.9). The five empirical constants may be determined analytically with the help of a simple experiment. The details are in Rodi[97]. The values recommended by Launder and Spalding[131] and generally accepted are as follows:

$$c_\mu = 0.09$$
$$\sigma_k = 1.0$$
$$\sigma_\varepsilon = 1.3$$
$$c_{\varepsilon 1} = 1.44$$
$$c_{\varepsilon 2} = 1.92$$

It should be remarked that the equation for ε may be constructed directly from the equation for k. Since k is linearly dependent on ε in view of Eq.(2.25), ε – equation can be made just by multiplying ε/k to each term of the k – equation with modifications for the empirical constants.

This two-equation model is true only at high Reynolds numbers, because the rate of dissipation is equal to the molecular kinetic viscosity times the fluctuating vorticity, $\nu \overline{\frac{\partial U_i}{\partial x_j} \frac{\partial U_i}{\partial x_j}}$, which is valid only when local isotropy prevails. Therefore, these raw equations cannot be directly applied for flows with solid boundaries. Many modifications to the $k-\varepsilon$ model near the wall have been proposed, which can be grouped into the wall function methods, the low Reynolds number models, and the parabolized sublayer model. These will be mentioned later in this chapter.

The $k-\varepsilon$ model in the form with fixed constants described above has been applied successfully to many two-dimensional flows such as wall boundary layers[132], duct flows[133], free shear flows[134], separated flows[31,135,136], and also to

three-dimensional wall boundary layers[137], confined flows[138], and jets[139]. But, the complete universality of the fixed constants cannot be expected. Experience has shown that different types of flows and boundary conditions require different values or functonal forms for some of the constants. The wall treatment[121,140] is a good example. Rodi[141,134] introduced one such function for an axisymmetric jet,

$$\begin{aligned} c_\mu &= 0.09 - 0.04f \\ c_{\varepsilon 2} &= 1.92 - 0.0667f \\ f &= \left| \frac{\delta}{\Delta U_m} \left(\frac{\partial U_0}{\partial x} - \left| \frac{\partial U_0}{\partial x} \right| \right) \right|^{0.2} \end{aligned} \tag{2.28}$$

where δ is the width of the jet, ΔU_m the maximum velocity difference across the jet, and U_0 the velocity along the axis of the jet.

The two-equation models account for the transport not only of the turbulence velocity scale, but also of the length scale. These may be the simplest models which promise success for flows for which the length scale cannot be prescribed empirically in an easy way. Various length scale equations have roughly similar performances, but the ε –equation became most popular because of its relative simplicity, its easier impositon of boundary conditions, and its better performance. With proper modifications, the predictions of the $k-\varepsilon$ model have been successful for two-dimensional flows in the boundary layers[121,140,149], jets and wakes[131,145], ducted flows[30,131,149,184,187], separated flows with heat transfer[20-22,131], flows with swirl[144- 146], with streamline curvature[142,143], and with buoyancy[147,148] , and for many three-dimensional flows.

Several possible reasons can be listed for some of the failures, among which are the assumption of the isotropy, the gradient-type diffusion, and the lack of generality of the

ε –equation. When the eddy viscosity concept breaks down, or when the individual components of the turbulent stresses play an important role, this model should be avoided.

2.3.4 Reynolds-Stress Models

2.3.4.1 Modeling of Reynolds stress equations

The full Reynolds stress model provides a more realistic physical simulation of a turbulent flow and is potentially a superior model. It allows for an investigation of the nonisotropy as well as eliminates the necessity for a postulated relationship between the turbulent kinetic energy and the individual Reynolds stresses. In reality, however, the individual $\overline{u_i u_j}$'s may develop quite differently in the flow, and when this is the case, the models discussed so far will be too simple. In order to account for the different development of the individual stresses, the transport equations for $\overline{u_i u_j}$ have been introduced. These equations can be derived in exact forms, but they contain the higher-order correlations that have to be approximated to be closed. A particular advantage of deriving the exact equations is that terms accounting for rotation, buoyancy, and other effects are introduced automatically.

According to Mellor and Herring[150], Chou[118,151] seems to be the first to initiate a study of the full set of the Reynolds-stress equations with an eye towards closure. However, it was Rotta[122] who laid the formulation for almost all of the current models. For an incompressible fluid, unaffected by the gravitational force and buoyancy effect, the transport of Reynolds stresses is governed by the equation:

$$\frac{\partial \overline{u_i u_j}}{\partial t} + U_k \frac{\partial \overline{u_i u_j}}{\partial x_k} = -\frac{\partial}{\partial x_k}\left(\overline{u_i u_j u_k} + \overline{\frac{p}{\rho}(\delta_{jk} u_i + \delta_{ik} u_j)} - \nu \frac{\partial \overline{u_i u_j}}{\partial x_k} \right)$$
$$-\left(\overline{u_i u_k} \frac{\partial U_j}{\partial x_k} + \overline{u_j u_k} \frac{\partial U_i}{\partial x_k} \right) + \overline{\frac{p}{\rho}\left(\frac{\partial u_i}{\partial x_j} + \frac{\partial u_j}{\partial x_i}\right)} \qquad (2.29)$$
$$-2\nu \overline{\frac{\partial u_i}{\partial x_k} \frac{\partial u_i}{\partial x_k}}$$

Eq.(2.29) is an exact consequence of the incompressible Navier-Stokes equations for a fluid with constant properties. It can be derived by multiplying the x_i- momentum equation by u_j and adding it to the x_j- momentum equation multiplied by u_i, and then taking the time-averaging of the resultant equation. Each term represents the time rate of change, the convective and diffusive transports, the stress generation by the interaction with the mean flow, pressure-strain, and viscous dissipation.

For the system of the stress equations to be closed, a model approximation must be provided for the diffusive transport, pressure redistribution, and viscous dissipation in terms of the mean velocities, the Reynolds stresses, and one or more parameters characterizing the length scale of turbulence or some "length containing" parameter such as the turbulence energy dissipation rate as done in the two-equation models.

For homogeneous turbulent flows, the diffusive transport terms are simply dropped. But, for inhomogeneous turbulent flows as in most real cases, the diffusive processes play important roles and need to be approximated. Daly and Harlow[152] proposed the simple gradient-transport model,

$$\frac{\partial}{\partial x_k}\left(\overline{u_i u_j u_k}\right) = -\frac{\partial}{\partial x_k}\left[c_S \frac{k}{\varepsilon} \overline{u_k u_l} \frac{\partial \overline{u_i u_j}}{\partial x_l} \right], \qquad (2.30)$$

where 0.22 is recommended for a value of c_s.

The viscous diffusion of stresses is negligible at high Reynolds numbers although its retention does not require further approximation. The pressure diffusion terms have been neglected successfully by most workers. The strongest evidence for neglecting these terms is a number of experiments, Irwin[153,154] for example, where the turbulence energy budget virtually balances without including the pressure transport terms. But Lumley[155] has suggested

$$\frac{\overline{pu_k}}{\rho} = -\frac{\overline{u_i^2 u_k}}{5} \tag{2.31}$$

from an analysis of the Poisson equation for pressure; the result implies that the pressure diffusion of the turbulence energy is directly proportional to and equal to -40% of that due to the velocity transport. Irwin's experiments and Lumley's suggestion come to an agreement in the sense that pressure fluctuations diminish the transport effects of the velocity fluctuations, however, the magnitude of the coefficient in Eq.(2.31) is larger than Irwin's data imply(except close to the wall where Lumley admits his approximation is not valid).

The pressure-strain correlation term, the rate at which the Reynolds stresses are destroyed by the interaction of the pressure fluctuations with the fluctuating rate of strain, is of particular importance for problems involving nonisotropy. This term sums to zero in the turbulent kinetic energy equation and serves only to redistribute the turbulence energy among the various components, and to reduce the shear stresses. This, therefore, contributes to making turbulence more isotropic. The pressure-strain correlation is modeled in a form with the pressure fluctuation eliminated. Taking the divergence of the equation for a fluctuating motion and integrating the resultant Poisson

equation yields two contributions to the pressure-strain correlation, one being due to the interaction of the fluctuating velocities only, $\phi_{ij,1}$, and one caused by the interaction of the mean strain and the fluctuating velocities, $\phi_{ij,2}$. Rotta's[122] linear return-to-isotropy hypothesis for the first part is adopted by most workers:

$$\phi_{ij,1} = -C_1 \frac{\varepsilon}{k} (\overline{u_i u_j} - \frac{2}{3} k\delta_{ij}) \tag{2.32}$$

where 1.4 was recommended for C_1 by Rotta. This expression indeed acts to redistribute the energy among its components by the fact that $\overline{u_i^2} = \frac{2}{3} k$ in the isotropic turbulence.

For the second part, Launder, Reece and Rodi[24] obtained the following form:

$$\begin{aligned} \phi_{ij,2} = & -\frac{(C_2+8)}{11} (P_{ij} - \frac{2}{3}\delta_{ij} P_k) - \frac{30C_2 - 2}{55} k (\frac{\partial U_i}{\partial x_j} + \frac{\partial U_j}{\partial x_i}) \\ & -\frac{8C_2 - 2}{11} (D_{ij} - \frac{2}{3}\delta_{ij} P_k) \end{aligned} \tag{2.33}$$

where

$$\begin{aligned} P_{ij} &= -\left(\overline{u_i u_k} \frac{\partial U_j}{\partial x_k} + \overline{u_j u_k} \frac{\partial U_i}{\partial x_k} \right) \\ D_{ij} &= -\left(\overline{u_i u_k} \frac{\partial U_k}{\partial x_j} + \overline{u_j u_k} \frac{\partial U_k}{\partial x_i} \right) \\ P_k &= -\overline{u_i u_j} \frac{\partial U_i}{\partial x_j} \end{aligned} \tag{2.34}$$

and 0.4 was suggested for C_2 by Launder *et al.* Earlier than this Naot *et al.*[156] and Reynolds[157] provided a good approximation,

$$\phi_{ij,2} = -\gamma (P_{ij} - \frac{2}{3}\delta_{ij} P_k) \tag{2.35}$$

which is the first term and the dominant one in Eq.(2.33)[24]. This relation is a direct counterpart of Eq.(2.32) because it assumes that the mean-strain rate of the pressure-strain term is proportional to the anisotropy of the production of $\overline{u_i u_j}$.

Two simple proposals appear to have been made for the dissipation term, both relating the dissipation rate of $\overline{u_i u_j}$ to the dissipation rate of the turbulent kinetic energy, ε, defined as $\nu \overline{(\frac{\partial u_i}{\partial x_k})^2}$. Donaldson[158] and Harlow and Nakayama[159] have proposed

$$\varepsilon_{ij} = 2\nu \overline{\frac{\partial u_i}{\partial x_k} \frac{\partial u_j}{\partial x_k}} = \varepsilon \frac{\overline{u_i u_j}}{k}, \tag{2.36}$$

while Rotta[122] and most other current workers have assumed

$$\varepsilon_{ij} = 2\nu \overline{\frac{\partial u_i}{\partial x_k} \frac{\partial u_j}{\partial x_k}} = \frac{2}{3} \delta_{ij} \varepsilon. \tag{2.37}$$

Eq.(2.36) may be taken to imply that the dissipating eddies are similar in structure to the energy containing ones, while Eq.(2.37) results from assuming the dissipative motions to be isotropic. At high Reynolds number Eq.(2.37) is certainly better founded. The final form of the modeled equations for the Reynolds stresses may be written as

$$\frac{\partial \overline{u_i u_j}}{\partial t} + U_k \frac{\partial \overline{u_i u_j}}{\partial x_k} = \frac{\partial}{\partial x_k} \left[c_S \frac{k}{\varepsilon} \overline{u_k u_l} \frac{\partial \overline{u_i u_j}}{\partial x_l} \right] - \left(\overline{u_i u_k} \frac{\partial U_j}{\partial x_k} + \overline{u_j u_k} \frac{\partial U_i}{\partial x_k} \right] + (\phi_{ij,1} + \phi_{ij,2}) - \frac{2}{3} \delta_{ij} \varepsilon \tag{2.38}$$

where the pressure diffusion is neglected.

The dissipative correlation ε is now the only term to be determined in the stress transport equations. For high Reynolds number flows, following Davidov[119] and Harlow and Nakayama[120], an exact transport equation for ε may be constructed as

$$\frac{\partial \varepsilon}{\partial t} + U_l \frac{\partial \varepsilon}{\partial x_l} = -\frac{\partial}{\partial x_j}\left[\nu \overline{u_j (\frac{\partial u_i}{\partial x_k})^2} + \frac{2\nu}{\rho} \overline{\frac{\partial p}{\partial x_j} \frac{\partial u_i}{\partial x_j}} - \nu \frac{\partial \varepsilon}{\partial x_j} \right]$$
$$- 2\nu \left[\frac{\partial U_i}{\partial x_j} \left(\overline{\frac{\partial u_i}{\partial x_k} \frac{\partial u_j}{\partial x_k}} + \overline{\frac{\partial u_k}{\partial x_i} \frac{\partial u_k}{\partial x_j}} \right) + \frac{\partial^2 U_i}{\partial x_j \partial x_k} \overline{u_j \frac{\partial u_j}{\partial x_k}} \right] \quad (2.39)$$
$$- 2\nu \overline{\frac{\partial u_i}{\partial x_j} \frac{\partial u_i}{\partial x_k} \frac{\partial u_j}{\partial x_k}} - 2\overline{(\nu \frac{\partial^2 u_i}{\partial x_j \partial x_k})^2}$$

A physical interpretation of each term on the right hand side in Eq.(2.39) can be stated as follows: the diffusion from the velocity and pressure fluctuations and of ε itself, two generation terms due to the mean shearing motion, the generation rate of vorticity fluctuation through the self-stretching action of turbulence, and the decay of the dissipation rate ultimately through the action of viscosity. A more detailed interpretation of the individual terms was provided in reference[160].

Now, since none of the terms on the right hand side in Eq.(2.37) is accessible to measurement, their modeling is dependent on the physical insight of workers. The diffusion term due to the pressure fluctuations may generally be neglected, and the diffusion of ε from the velocity fluctuations is treated in a manner analogous to its counterpart in the stress equation (2.30),

$$\nu \overline{u_j (\frac{\partial u_i}{\partial x_k})^2} = \overline{u_j \varepsilon'} = -c_\varepsilon \frac{k}{\varepsilon} \overline{u_j u_k} \frac{\partial \varepsilon}{\partial x_k} \quad (2.40)$$

where the mean-square-root of ε' is defined as $\nu \overline{\frac{\partial u_i}{\partial x_k} \frac{\partial u_i}{\partial x_k}}$. The viscous transport term, which needs no approximation, is negligible in fully turbulent flows. The generation term can be appropriately approximated:

$$2\nu\left(\overline{\frac{\partial u_i}{\partial x_k}\frac{\partial u_j}{\partial x_k}}+\overline{\frac{\partial u_k}{\partial x_i}\frac{\partial u_k}{\partial x_j}}\right) = c_{\varepsilon 1}\frac{\varepsilon}{k}\overline{u_i u_j} + \tilde{c}_{\varepsilon 1}\delta_{ij} \tag{2.41}$$

where $c_{\varepsilon 1}$ and $\tilde{c}_{\varepsilon 1}$ are constants. In fact, the term containing $\tilde{c}_{\varepsilon 1}$ vanishes when Eq.(2.38) is multiplied by $\frac{\partial U_i}{\partial x_j}$. The second generation term is usually neglected. The generation rate of the vorticity fluctuations and the dissipation of the dissipation rate are combined to give the same result as the one in the $k-\varepsilon$ model, which is

$$-2\left[\nu\overline{\frac{\partial u_i}{\partial x_j}\frac{\partial u_j}{\partial x_k}\frac{\partial u_j}{\partial x_k}}+\overline{(\nu\frac{\partial^2 u_i}{\partial x_j \partial x_k})^2}\right] = \left(c_{\varepsilon 1}\frac{P_k}{\varepsilon} - c_{\varepsilon 2}\right)\frac{\varepsilon^2}{k}, \tag{2.42}$$

$c_{\varepsilon 2}$ being a constant. The final form of the simulated transport equation for the energy dissipation rate for high Reynolds numbers can be expressed as follow:

$$\begin{aligned}\frac{\partial \varepsilon}{\partial t}+U_l\frac{\partial \varepsilon}{\partial x_l} &= +c_\varepsilon\frac{\partial}{\partial x_j}\left(\frac{k}{\varepsilon}\overline{u_j u_k}\frac{\partial \varepsilon}{\partial x_k}\right) - c_{\varepsilon 1}\frac{\varepsilon}{k}\overline{u_i u_j}\frac{\partial U_l}{\partial x_j} \\ &\quad + \left(c_{\varepsilon 1}\frac{P_k}{\varepsilon} - c_{\varepsilon 2}\right)\frac{\varepsilon^2}{k}\end{aligned} \tag{2.43}$$

The determination of three constants in the above equation is explained well in references[86,104].

The Reynolds stress model, with wall corrections where appropriate, has been applied to a number of homogeneous flows[153,161] , and jets and wakes[162], wall boundary layers, two- and three-dimensional duct flows[24,152], and flows with

separation[32]. For very complex flows, such as those predicted by Gibson *et al.*[163-165], Wilcox and Rubesin[166], and others, the Reynolds stress model has been much superior to the $k-\varepsilon$ model. But for moderate-to-simple shear layers, the $k-\varepsilon$ model may be adequate. In summary, the Reynolds stress model is computationally expensive and little tested so far and has not yet reached the state of practical application. It is not clear under what situations the Reynolds stress model is better than the $k-\varepsilon$ model. For further information, one should refer to Launder[104], Rodi[167], and/or Lakshminarayana[102].

2.3.4.2 Stability and realizability

Many phenomenological turbulence models for the Reynolds-stress transport equations have been suggested which consist of a set of partial differential equations for the mean velocities U_i, and the Reynolds stresses R_{ij} together with an appropriate predictive equation for the integral length scale L or for the dissipation rate ε. These models contain closure assumptions which relate algebraically unknown correlations, such as the pressure-strain correlations

$$\phi_{ij} = \overline{p\left(\frac{\partial u_i}{\partial x_j} + \frac{\partial u_j}{\partial x_i}\right)} \tag{2.44}$$

to the known quantities U_i, R_{ij}, and L or ε. Such models may not have a solution for an arbitrary set of the initial and boundary conditions in the sense that the realizability conditions

$$R_{ij} \geq 0 \qquad \text{for} \quad i = j \tag{2.45}$$

$$R_{ij}^2 \leq R_{ii} R_{jj} \quad \text{for} \quad i \neq j \tag{2.46}$$

$$\det(R_{ij}) \geq 0 \tag{2.47}$$

may be violated[168,169]. In equations (2.45) and (2.46) the summation convention is not adapted for indices. The conditions (2.45) and (2.47) are the consequence of real velocities(nonnegative energy), and the condition (2.46) is the consequence of the Schwarz' inequality. It is important to know whether the divergence of solution during iterations is a consequence of an unstable numerical scheme, which can be adjusted, or a consequence of the model itself and of the initial and boundary conditions.

Schumann[169] proved the realizability of each term in the Reynolds stress equations and came to a conclusion that the realizabilities for the pressure diffusion and the redistribution could not be proved independently. This suggests that the independent modeling of these terms may result in nonrealizable models. The fact that the realizability can be proven independently for the terms in groups shows that the realizability of the exact equations is guaranteed for any sign and magnitude of the values $\partial U_i/\partial x_j$, p, or $\nu\, \partial u_i/\partial x_j$.

The separate treatment of the redistribution term from the pressure diffusion is either over-realizable for Rotta's proposal, Eq.(2.32), or nonrealizable for Naot's and Reynolds' approximation, Eq.(2.35). The over-realizable model of Rotta would be unsuitable for the extremely anisotropic turbulence such as certain atmospheric or magneto-hydrodynamic flow problems. If realizability is not strictly enforced, instability during iterations is not entirely prevented[168].

2.3.5 Algebraic Reynolds Stress Models

The Reynolds stress closure presented in the previous section requires the solution of more than six transport equations for the turbulent quantities for general three-dimensional flows. While obtaining solutions to such equations may be within current computational capabilities, it is not a trivial task and not economical. Simpler approaches, therefore, have been made to simplify the equations such that they reduce to algebraic expressions but still retain most of their basic features. The essence of this simplification resides in the recognition that the only terms containing gradients of the Reynolds stresses in the closure are those in the convective and diffusive transport terms. If these gradients can be eliminated by the model approximations, the partial differential equations can be reduced to a set of algebraic equations. A generally valid approximation was proposed by Rodi[170] who assumed that the convective and diffusive transports of the Reynolds stresses are related to the kinetic energy transport rates by the formulae:

$$\frac{D\overline{u_iu_j}}{Dt} = \frac{\overline{u_iu_j}}{k}\frac{Dk}{Dt} \tag{2.48}$$

$$D(\overline{u_iu_j}) = \frac{\overline{u_iu_j}}{k} D(k), \tag{2.49}$$

where the operator $D(\ )$ stands for a net diffusion rate of the quantity in the parenthesis. Equation (2.48) is a good approximation when the rate of variation of $\overline{u_iu_j}/k$ along a streamline is much smaller than that of $\overline{u_iu_j}$ itself. The diffusive transport approximation is also valid whenever the spatial gradient of $\overline{u_iu_j}$ is large compared with that of $\overline{u_iu_j}/k$. From the $k-$ equation (2.25)

$$\frac{Dk}{Dt} - D(k) = P_k - \varepsilon, \tag{2.50}$$

thus

$$\frac{D\overline{u_iu_j}}{Dt} - D(\overline{u_iu_j}) = \frac{\overline{u_iu_j}}{k}(P_k - \varepsilon). \tag{2.51}$$

Comparison of Eq.(2.51) with the Reynolds stress equation (2.38) yields

$$\frac{\overline{u_iu_j}}{k}(P_k - \varepsilon) = P_{ij} + \phi_{ij,1} + \phi_{ij,2} - \varepsilon_{ij}, \tag{2.52}$$

P_{ij}, $\phi_{ij,1}$, $\phi_{ij,2}$, and ε_{ij} being defined earlier in the previous section. Substitution of these definitions into Eq.(2.52) results in

$$\overline{u_iu_j} = k\left[\frac{2}{3}\delta_{ij} + \frac{(1-\gamma)(P_{ij} - \frac{2}{3}\delta_{ij}P_k)}{P_k + (C_1 - 1)\varepsilon}\right] \tag{2.53}$$

If Eq.(2.53) is specialized to the case of two-dimensional thin shear flows, the formula for the shear stress becomes

$$-\overline{uv} = \frac{2}{3}(1-\gamma)\frac{C_1 - 1 + \gamma P_k/\varepsilon}{(C_1 - 1 + P_k/\varepsilon)^2}\frac{k^2}{\varepsilon}\frac{\partial U}{\partial y} \tag{2.54}$$

It should be noted that Eq.(2.54) links the shear stress to the local rate of strain so that it is an "effective-viscosity" relationship, $\frac{k^2}{\varepsilon}$ having the dimension of the kinematic viscosity. The two unknown quantities, the kinetic energy and the dissipation rate, are generally determined by solving their transport equations as done in the $k-\varepsilon$ model.

Algebraic stress models are useful tools between the isotropic eddy viscosity models and the stress equation models. They combine, to some extent, the economy of the former with the universality of the latter. Algebraic stress models have been applied successfully to predict the partition of normal stresses in a number of thin shear layers[163,170], to predict turbulence-driven secondary flows in square ducts[171], and to describe the influence of buoyancy on various shear layers[143,172,173] and in near-wall layers[174], and the feature of a reacting shear layer in a divergent channel[30].

2.3.6 Large Eddy Simulation

A fundamentally different method of computing three-dimensional turbulent flows, that potentially is universally applicable, is the computer simulation of the large eddy structure, rather than solving the Reynolds time-averaged form of the equations of motion, of the turbulent flow fields. The idea is based on the experimentally observed spectral character of turbulent flow fields. Generally, the large eddies are created by the instabilities of the mean flow and continuously extract energy from the mean shearing motion. These large eddies break into smaller eddies due to the nonlinearity in nature. The smaller eddies also interact to produce even smaller ones and merge to form larger ones. The smallest eddies are generated by the breaking up of the larger eddies, and they lose their identities by dissipating their energy into heat due to the molecular viscosity. This process of the production of the smaller eddies through the instabilities and the recombination of eddies continues until a continuous spectrum of eddies is generated and reaches a stationary random state.

The large eddies contain most of the energy of turbulence, have relatively long life-time, and are anisotropic and different from type to type of the flow and surrounding boundaries. The large eddy simulation of turbulence predicts these mechanics for the largest eddies and approximates the effects of the eddies smaller than the finite difference mesh can resolve. The prediction of the large scale turbulent motions is made by numerically solving the three-dimensional, time-dependent equations of motion. The approximation of the effects of the small-scale eddies is, therefore, called subgrid-scale modeling. The subgrid-scale scheme does not adopt the time-averaging process over an infinitely long period as done in the Reynolds equations, but over a sufficiently small interval that only time-dependent fluctuations of small scale turbulent motions can be smoothed out. The overall accuracy of turbulence prediction can be enhanced in a sense that only a fraction of the turbulence needs to be modeled. Also, the isotropic and, hopefully, universal character of the small-scale eddies may permit the development of closure models based on more reasonable physical arguments. This method has a very promising potential for understanding and accurate numerical simulation of turbulence, but still is not fully understood and is very costly computationally. It is now mainly looked upon as a tool of improving the modeling approximations of the simple closures.

The origin of the subgrid-scale modeling goes back to meteorologists who, in their numerical integration of geophysical-scale flows, found it necessary to introduce an eddy viscosity, which provided an essential numerical stabilization and represented physically the damping by the eddies smaller than the computational grid size. Lilly[175] appears to be the first to make explicitly the separation of computational grid scales from the subgrid scales by introducing the volume Reynolds averaging over the computational grid, Δ^3.

The subgrid-scale model was successfully applied by Deardorff to studies of channel flow[176] and planetary boundary layer flows[168, 177]. Schumann[178] solved turbulent flows in plane channels and annuli. Extension of the subgrid scale models has been made mainly by Reynolds and his associates[179,180] at Stanford University and Love and Leslie[181] at Queen Mary College in England.

2.4 Wall treatments

All the closure models presented so far are valid only in fully turbulent regions. Close to solid walls and some other interfaces, there inevitably exist regions, where the local turbulent Reynolds number $R_T(\equiv \sqrt{k}\, L/\nu$ where $L = k^{3/2}/\varepsilon)$ is so small that the molecular viscosity exerts a direct influence on turbulence, and where the assumption of turbulence isotropy breaks down; this is certainly true of the dissipation isotropy and of the Rotta's fundamental energy redistribution concept.

Over the past years, many suggestions have been made for the extension of the turbulence closure models to enable their use at low Reynolds numbers and to describe flows close to a solid wall. The simplest example of the near-wall modifications to turbulence models is the Van Driest[182] damping function for the mixing length. More advanced models incorporate either a wall damping effect or a direct effect of the molecular viscosity, or both, on the empirical constants and functions in the turbulence transport equations, devised originally for high Reynolds number, fully turbulent flows remote from the walls. In the absence of reliable turbulence data in the immediate vicinity of the walls or at low Reynolds numbers, these modifications have been based

largely on personal insights, and numerical experiments and comparisons between calculations and experiments in terms of global parameters.

There are several ways of accounting for the presence of the wall; they are the wall function methods, the low-Reynolds-number modeling, and the parabolized sublayer approximation. Following discussion on the wall treatments will be limited to the $k-\varepsilon$ model, but mostly can be applied to other class of models.

2.4.1 Wall Function Methods

Near a solid surface, the largest stress-containing eddies have a wavelength of the order of the distance from the surface, say y. The eddies with a larger longitudinal wavelength are too flat to carry much shear stress. Since $y << \delta$, where δ is the total width of a shear layer, the eddies are little affected by the turbulent motion in the outer part of the flow, and their life time is short compared to the time scale of significant change in the primary direction. Thus, both the mean and turbulent transport of the Reynolds stresses to or from regions at a distance much larger than y are negligible, and the typical velocity scale of the turbulence depends only on the conditions in this "inner layer", specifically on the shear stress transmitted through the layer to the surface, τ_w. If the velocity scale of the turbulence is independent of y and the length scale is dependent only on y, we expect the turbulent transport of the Reynolds stresses within the layer to be small, so that the turbulent kinetic energy or the exact Reynolds stress equations reduce to "generation = destruction", all transport terms being zero. This is called a state of the local equilibrium. If this is the case, a substantial near wall mesh requirement is not needed. This feature is crucial in reducing overall core storage and

computing time burdens remarkably and gives a good reason why the wall functions have been favorably adopted.

The local equilibrium renders Eq.(2.25) to be

$$\varepsilon \simeq P_k = \frac{\tau_w}{\rho} \frac{\partial U}{\partial y} \tag{2.55}$$

where $\tau_t \simeq \tau_w$ is used in the logarithmic region of the inner layer. In that region an empirical relation,

$$U = \frac{u_*}{\kappa} \ln (Ey^+), \tag{2.56}$$

holds, where u_* is the friction velocity ($= \sqrt{\frac{\tau_w}{\rho}}$). Combination of Eqs.(2.54), (2.55), and (2.27) with $\frac{\tau_w}{\rho} = \nu_t \frac{\partial U}{\partial y}$ results in

$$\varepsilon = \frac{u_*^3}{\kappa y} \tag{2.57}$$

$$k = \frac{u_\tau^2}{\sqrt{c_\mu}}. \tag{2.58}$$

Chieng and Launder[20] suggested a two-layer wall function for the $k-\varepsilon$ model which was applied to solve a heat transfer problem in an abrupt pipe expansion. They divided the turbulent boundary layer into a viscous-affected part and a strong turbulent part, and obtained algebraic relations in each part based on the idea that the wall's dominance on the length scale near the wall is complete; outside of the viscous sublayer the length scale is held to depend, for a limited region near the wall, only on the normal

distance from the wall. Their suggestion was applied to the computation of a turbulent impinging jet by Amano and Neusen[183].

Later in 1984, Amano[22] proposed a similar three-layer model that is composed of a viscous sublayer ($0 < y^+ < 5$), a buffer layer ($5 < y^+ < 30$), and an overlap layer ($30 < y^+ < 400$). He obtained a better prediction of the Nusselt number distribution over the two-layer near wall model for turbulent flow in a sudden pipe expansion.

2.4.2 Low Reynolds Number Models

The success enjoyed by the turbulence closure models in the prediction of wall bounded shear layer flows has depended, to a large extent, upon the application of the wall functions that relate surface boundary conditions to points in the fluid away from the boundaries and thereby avoid the problem of modeling the direct influence of viscosity. The validity of this procedure is, of cource, restricted to situations in which the Reynolds number is sufficiently high for the viscous effects to be unimportant, or in which the universal wall functions are well established. There are a number of instances in which this approach has to be abandoned, e.g., turbulent boundary layers at low and transitional Reynolds numbers, flows with steep streamwise pressure gradient, unsteady and separated flows, and flow over spinning surfaces or surfaces with mass or heat transfer. Also, the traditional wall functions are probably inappropriate for complex three-dimensional flows.

In order to provide predictions of flow within the viscous sublayer adjacent to the wall, the high Reynolds number form of the model must be enlarged in three ways, according to Jones and Launder[121]. They are

1. the viscous diffusion of k and ε must be included;
2. the terms containing the c's in the transport equations must become dependent upon the Reynolds number of turbulence;
3. further terms must be added to account for the fact that the dissipation processes are not isotropic.

After Jones and Launder's proposal many suggestions for near-wall model have followed. Launder and Sharma[140] made a slight modification to the Jones and Launder model and successfully solved a swirling flow problem. Since then, Hoffman's proposal for channel flow[184], Reynolds' proposal[96], Hassid and Poreh's for drag reduction[185], Dutoya and Michard's for compressor and turbine blades[186], Lam and Bremhorst's pipe flow[187], and Chien's for flat plate and channel flows[149] have been made. Patel *et al.*[188] reviewed and compared the performance of all the proposals for a boundary layer at high and low Reynolds numbers and for equilibrium boundary layers in adverse pressure gradients. They concluded that Launder and Sharma's model works best over others. With the fact mentioned above and since only the Launder and Sharma's model has tested the effect of swirl, their model was selected to solve the concerned flow problem in this work.

The complete form of the turbulence model is given below with the wall modifications in the boxes:

$$\frac{Dk}{Dt} = \frac{\partial}{\partial x_j}\left[(\nu + \nu_t)\frac{\partial k}{\partial x_j}\right] - \overline{u_i u_j}\frac{\partial U_i}{\partial x_j} - \tilde{\varepsilon} - 2\nu\left(\frac{\partial \sqrt{k}}{\partial x_l}\right)^2 \qquad (2.59)$$

$$\frac{D\tilde{\varepsilon}}{Dt} = \frac{\partial}{\partial x_j}\left[(\nu + \nu_t)\frac{\partial \tilde{\varepsilon}}{\partial x_j}\right] - c_1 f_1 \overline{u_i u_j}\frac{\tilde{\varepsilon}}{k}\frac{\partial U_i}{\partial x_j} - c_2 f_2 \frac{\tilde{\varepsilon}^2}{k} + 2\nu\nu_t\left(\frac{\partial^2 U_i}{\partial x_k \partial x_l}\right)^2 \tag{2.60}$$

$$-\overline{u_i u_j} = c_\mu f_\mu \frac{k^2}{\tilde{\varepsilon}}\cdot\left(\frac{\partial U_i}{\partial x_j} + \frac{\partial U_j}{\partial x_i}\right) = \nu_t\left(\frac{\partial U_i}{\partial x_j} + \frac{\partial U_j}{\partial x_i}\right) \tag{2.61}$$

where auxiliary relations are given as follows:

$$\nu_t = c_\mu f_\mu \frac{k^2}{\tilde{\varepsilon}}$$

$$f_\mu = \exp\left[-\frac{3.4}{(1 + R_t/50)^2}\right],$$
$$f_1 = 1.0$$
$$f_2 = 1.0 - 0.3\exp[-R_t^2]$$
$$R_t = \frac{k^2}{\nu\tilde{\varepsilon}}$$

where R_t is a turbulent Reynolds number based on a velocity scale $\sqrt{k}$ and a length scale $k^{3/2}/\tilde{\varepsilon}$.

The proposal of using $\tilde{\varepsilon}$ as the "dissipation variable" is due to Jones and Launder[121], who cited decisive computational advantages of using it. They argued that the dissipation rate used in the $k-\varepsilon$ equation, which is defined as

$$\varepsilon = \nu\overline{\frac{\partial u_j}{\partial x_l}\frac{\partial u_j}{\partial x_l}}, \tag{2.62}$$

is not zero right on the wall. The term ε is the dissipation rate only in the case of the homogeneous, not isotropic, turbulence as Hinze[189] pointed out. The term $\tilde{\varepsilon}$ is chosen

such that it is zero at the wall for a numerically convenient boundary condition. It satisfies the following relation near the wall

$$\tilde{\varepsilon} = \varepsilon - 2\nu \left(\frac{\partial \sqrt{k}}{\partial x_l}\right)^2 \tag{2.63}$$

The last term of the right hand side in Eq.(2.60) is also one that does not appear in the high-Reynolds number form of the model. The authors could provide no physical argument for its adoption. Its inclusion is simply for matching the desired profile of k near the wall and was found by dimensional analysis and numerical adjustment.

2.4.3 Parabolized Sublayer(PSL) Model

The PSL scheme is based on the idea that, while the flow as a whole must be regarded as elliptic, there is a thin parabolic sublayer immediately adjacent to a wall across which the static pressure variations are negligible or, in the case of highly-curved surfaces the variation may be obtained by assuming a radial equilibrium[190]. This parabolic sublayer is taken to extent over the whole low-Reynolds-number region where the turbulent transport properties exhibit such a strongly nonlinear variation. If a fine grid is desirable on physical grounds, its treatment is employed across this region, and then major simplifications may be made to the conventional incompressible elliptic treatment. Within the parabolized sublayer:

1. the pressure does not require storing since it can be supplied by the pressure just outside the region;
2. thus no Poisson or pressure-perturbation equation has to be solved;

3. the velocity component normal to the wall may be obtained very rapidly by cell continuity rather than by solving the normal momentum equation.

These facts indicate clear advantages of the PSL; its computation time and memory demands are comparable with the wall function approaches.

Launder[191] tested the PSL scheme for convective heat transfer problems, and obtained better prediction over the wall function method. But, the better performance is much damaged in the vicinity of a stagnation point or when a reverse flow is present.

3. FINITE ELEMENT METHODS

3.1 *Governing Equations and Boundary Conditions*

The governing system of equations describing the mean flow field, obtained by the Reynolds time-averaging process, is expressed in cylindrical coordinates (x, r, θ) as

continuity:

$$\frac{\partial U_x}{\partial x} + \frac{1}{r}\frac{\partial}{\partial r}(rU_r) = 0 \tag{3.1}$$

x-momentum

$$U_x\frac{\partial U_x}{\partial x} + U_r\frac{\partial U_x}{\partial r} = \frac{1}{\rho}\frac{\partial}{\partial x}(\sigma_{xx}) + \frac{1}{\rho r}\frac{\partial}{\partial r}(r\sigma_{xr}) + \frac{1}{\rho}f_x \tag{3.2}$$

r-momentum:

$$U_x\frac{\partial U_r}{\partial x} + U_r\frac{\partial U_r}{\partial r} - \frac{U_\theta^2}{r} = \frac{1}{\rho}\frac{\partial}{\partial x}(\sigma_{xr}) + \frac{1}{\rho r}\frac{\partial}{\partial r}(r\sigma_{rr}) - \frac{1}{\rho}\frac{\sigma_{\theta\theta}}{r} + \frac{1}{\rho}f_r \tag{3.3}$$

θ-momentum:

$$U_x\frac{\partial U_\theta}{\partial x} + U_r\frac{\partial U_\theta}{\partial r} + \frac{U_rU_\theta}{r} = \frac{1}{\rho}\frac{\partial}{\partial x}(\sigma_{x\theta}) + \frac{1}{\rho r^2}\frac{\partial}{\partial r}(r^2\sigma_{r\theta}) + \frac{1}{\rho}f_\theta \tag{3.4}$$

In the equations, U_x, U_r, and U_θ are the mean velocities along the axial(x), radial(r), and tangential(θ) directions, respectively, and ρ is the flow density, and f_x, f_r, and f_θ are the body forces per unit volume along each direction. The flow field is considered steady, axisymmetric, incompressible, and with constant physical properties. By axisymmetric it is meant that all the field variables including U_θ are functions of x and r. The stresses in the equations defined as follows;

$$\sigma_{xx} = -P + 2(\mu + \mu_t)\frac{\partial U_x}{\partial x} \qquad \sigma_{xr} = (\mu + \mu_t)\left(\frac{\partial U_r}{\partial x} + \frac{\partial U_x}{\partial r}\right)$$

$$\sigma_{rr} = -P + 2(\mu + \mu_t)\frac{\partial U_r}{\partial r} \qquad \sigma_{r\theta} = (\mu + \mu_t)\, r\, \frac{\partial}{\partial r}\left(\frac{U_\theta}{r}\right) \tag{3.5}$$

$$\sigma_{\theta\theta} = -P + 2(\mu + \mu_t)\frac{U_r}{r} \qquad \sigma_{x\theta} = (\mu + \mu_t)\frac{\partial U_\theta}{\partial x}$$

where $\mu_t (= \rho\, \nu_t)$ is to represent the Reynolds stresses by the Boussinesq's eddy viscosity expression[107]:

$$-\overline{u_i u_j} = \nu_t\left(\frac{\partial U_i}{\partial x_j} + \frac{\partial U_j}{\partial x_i}\right) - \frac{2}{3}\, k\, \delta_{ij} \tag{3.6}$$

The momentum equations are expressed in terms of the divergence of stresses. This representation has a great advantage when the Galerkin finite element procedure is applied to these equations. The stress-divergence form results in a natural boundary condition which can be interpreted physically as the components of stress acting on the fluid at the boundary, while the Navier-Stokes form results in a natural boundary condition, which while almost identical, has no corresponding direct physical interpretation. Above equations governing the primitive mean-flow quantities U_i and P do not form a closed set due to an appearance of a field variable ν_t. The determination

of ν_t requires two supplemental turbulence transport equations for the velocity and length scales as follows:

$$U_x \frac{\partial k}{\partial x} + U_r \frac{\partial k}{\partial r} = \frac{\partial}{\partial x}\left[(\nu + \frac{\nu_t}{\sigma_k}) \frac{\partial k}{\partial x} \right] + \frac{1}{r} \frac{\partial}{\partial r}\left[r(\nu + \frac{\nu_t}{\sigma_k}) \frac{\partial k}{\partial r} \right] + P_k - \tilde{\varepsilon} - 2\nu \left(\frac{\partial \sqrt{k}}{\partial r} \right)^2 \tag{3.7}$$

$$U_x \frac{\partial \tilde{\varepsilon}}{\partial x} + U_r \frac{\partial \tilde{\varepsilon}}{\partial r} = \frac{\partial}{\partial x}\left[(\nu + \frac{\nu_t}{\sigma_\varepsilon}) \frac{\partial \tilde{\varepsilon}}{\partial x} \right] + \frac{1}{r} \frac{\partial}{\partial r}\left[r(\nu + \frac{\nu_t}{\sigma_\varepsilon}) \frac{\partial \tilde{\varepsilon}}{\partial r} \right] + \frac{\tilde{\varepsilon}}{k}(c_{\varepsilon 1} f_1 P_k - c_{\varepsilon 2} f_2 \tilde{\varepsilon}) + 2\nu\nu_t \left\{ \frac{\partial}{\partial r}\left[\left(\frac{\partial U_x}{\partial r} \right)^2 + \left(r \frac{\partial (U_\theta / r)}{\partial r} \right)^2 \right]^{1/2} \right\}^2 \tag{3.8}$$

where k and $\tilde{\varepsilon}$ are the turbulent kinetic energy per unit mass and its rate of dissipation. The terms for the wall modification[140,146] are included in the boxes, which are accounted for only near the wall, and simply dropped in the fully turbulent region away from the wall. The production of the turbulent kinetic energy P_k and supplemental algebraic relations are written as

$$P_k = 2\nu_t \left[(\frac{\partial U_x}{\partial x})^2 + (\frac{\partial U_r}{\partial r})^2 + (\frac{U_r}{r})^2 \right] + \nu_t \left[(\frac{\partial U_x}{\partial r} + \frac{\partial U_r}{\partial x})^2 + \left(r \frac{\partial}{\partial r}(\frac{U_\theta}{r}) \right)^2 + (\frac{\partial U_\theta}{\partial x})^2 \right] \tag{3.9}$$

and

$$
\begin{aligned}
\nu_t &= c_\mu f_\mu \frac{k^2}{\tilde{\varepsilon}} \\
f_\mu &= \exp\left[-\frac{3.4}{(1 + R_T/50)^2} \right] \\
R_T &= \frac{k^2}{\nu\tilde{\varepsilon}} \\
f_1 &= 1.0, \qquad f_2 = 1.0 - 0.3 \exp(-R_T^2) \\
\sigma_k &= 1.0, \quad \sigma_\varepsilon = 1.3, \quad c_{\varepsilon 1} = 1.0, \quad c_{\varepsilon 2} = 1.92, \quad c_\mu = 0.09
\end{aligned}
\tag{3.10}
$$

The boundary conditions may be written as

at inlet cross-section :

$$U_x = U_x(r); \quad U_r = U_r(r); \quad U_\theta = U_\theta(r); \quad k = k(r); \quad \tilde{\varepsilon} = \tilde{\varepsilon}(r)$$

at exit cross-section :

$$t_x = t_r = t_\theta = 0; \quad \frac{\partial k}{\partial x} = \frac{\partial \tilde{\varepsilon}}{\partial x} = 0$$

on solid walls :

$$U_x = U_r = U_\theta = k = \tilde{\varepsilon} = 0 \tag{3.11}$$

along the centerline :

$$U_r = 0; \quad \frac{U_x}{\partial r} = \frac{U_\theta}{\partial r} = \frac{\partial k}{\partial r} = \frac{\partial \tilde{\varepsilon}}{\partial r} = 0$$

in entrainment region $r > \delta$:

$$\frac{\partial U_x}{\partial r} = \frac{\partial U_r}{\partial r} = \frac{\partial U_\theta}{\partial r} = \frac{\partial k}{\partial r} = \frac{\partial \tilde{\varepsilon}}{\partial r} = 0$$

At the inlet plane the mean velocity components and turbulence intensities are obtained from measurements. The rate of dissipation of the turbulent kinetic energy is supplied by the empirical relations available in several regions. Near the wall region for $r^+ < 30$, the Van Driest damping function[182] is used:

$$\mu_t = \rho \kappa^2 \left[1 - \exp(-\frac{r^+}{26}) \right]^2 r^2 \left| \frac{\partial U_x}{\partial r} \right| \tag{3.12}$$

In the logarithmic part of the inner region of $30 < r^+ < 100$, the convection and diffusion of the Reynolds strresses are negligible and the local equilibrium prevails. This assumption results in

$$\text{production} = \text{dissipation} \tag{3.13}$$

or

$$\tilde{\varepsilon} = \frac{\tau_w}{\rho_\infty} \frac{\partial U_x}{\partial r} = \frac{u_*^3}{\kappa r} \tag{3.14}$$

In the outer region Clauser eddy viscosity model[192] is employed

$$\mu_t = 0.018 \rho U_\infty \delta^* \tag{3.15}$$

where δ^* is the displacement thickness of the boundary layer. Once μ_t is given, $\tilde{\varepsilon}$ is obtained by the relation $\mu_t = c_\mu k^2/\tilde{\varepsilon}$. A smooth curve fitting is necessary between the regions.

3.2 Variational Formulation

3.2.1 Variational Principles

The appropriate connection of the calculus of variations to boundary value problems of partial differential equations had long been sought. The practical applications were envisaged by two physicists, Lord Rayleigh and Walter Ritz[194]; they independently

conceived the idea of utilizing this connection for a numerical calculation of many engineering problems, by substituting for the variational problems simpler approximating extremum problems in where only a finite number of parameters need to be determined.

Consider an equilibrium boundary value problem for a membrane under external force f. It leads to a linear self-adjoint differential equation for an unknown function $u(x,y)$:

$$\begin{aligned} Lu &= f \quad in\ B \\ u &= 0 \quad on\ S \end{aligned} \tag{3.16}$$

where L is a Laplacian operator in a two-dimensional simply connected domain B with Dirichlet conditions specified along its smooth boundary S. The conventional Rayleigh-Ritz method seeks the minimum of the variational functional,

$$I(u) = \frac{1}{2}\int\int_B [u_x^2 + u_y^2 + 2uf]\,dx\,dy \tag{3.17}$$

for the deflection u.

Later in 1943 Courant[193] suggested the following method of obtaining better convergence in the Rayleigh-Ritz method. Instead of considering the simple variational problem, he modified the former problem without changing the solution of the latter. For the same equilibrium problem he constructed a similar functional,

$$I(u) = \frac{1}{2}\int\int_B [u_x^2 + u_y^2 + 2uf]\,dx\,dy + \frac{1}{2}\int\int_B \lambda\,(Lu - f)^2\,dx\,dy \qquad (3.18)$$

where λ is an arbitrary positive constant or function. Such additional term makes $I(u)$ more sensitive to the variation of u without changing the solution. In other words, minimizing sequences attached to such a "sensitized" functional will by force behave better as regards convergence.

By the same analogy as Eq.(3.18) is constructed, another functional can be considered using the essential boundary condition in Eq.(3.16):

$$I(u) = \frac{1}{2}\int\int_B [u_x^2 + u_y^2 + 2uf]\,dx\,dy + \frac{\gamma}{2}\int_S u^2\,dS \qquad (3.19)$$

where γ is an arbitrary large number to freeze the boundary condition. For sufficiently large values for γ , the boundary value problem corresponding to the functional in Eq.(3.19) is almost equivalent to that associated with the functional in Eq.(3.16).

3.2.2 Galerkin Formulation of Navier-Stokes Equations

As we have seen in the previous section, the variational formualtion is a weak formulation in which the original constrained differential equation is transformed into an unconstrained integral form and the minimum of the variational(quadratic)

functional is sought as an equivalent set of solution. A general approach to formulating the equations for the finite element method depends on the existence of a varational form of the boundary value problem. Even though there exists no classical variational principle for the Navier-Stokes equations, it is possible to obtain a weak form of the Navier-Stokes equations by using the Galerkin approach[195].

The equations of motion for general three-dimensional flow are recalled as follows:

$$L(U_i) = U_j \frac{\partial U_i}{\partial x_j} - \frac{\partial}{\partial x_j}\left[\nu \left(\frac{\partial U_i}{\partial x_j} + \frac{\partial U_j}{\partial x_i} \right) \right] + \frac{1}{\rho} \frac{\partial P}{\partial x_i} - f_i = 0 \quad in \ B \tag{3.20}$$

$$L(P) = \frac{\partial U_i}{\partial x_i} = 0 \quad in \ B \tag{3.21}$$

which, for simplicity, are subject to Dirichlet boundary conditions,

$$U_i = 0 \quad on \ S \tag{3.22}$$

where S is boundary of domain B The problem can be viewed as one of seeking the solution $U_i(x_j)$ such that Eq.(3.22) is satisfied and the functional

$$I(U_i) = \int_B \left[U_j \frac{\partial U_i}{\partial x_j} U_i + \frac{\nu}{2} \left(\frac{\partial U_i}{\partial x_j} + \frac{\partial U_j}{\partial x_i} \right)^2 - f_i U_i \right] dB \tag{3.23}$$

is minimized. The pressure drops out of the functional owing to the fact that the velocity field satisfies the incompressiblity condition Eq.(3.21) identically[60]. Once the velocity field is known, the pressure can be calculated from Eq.(3.20). There are two common ways to enforce the constraint on Eq.(3.20): the Lagrange multiplier method

and the penalty function method. These give rise to the velocity-pressure or mixed, and the penalty formulations, respectively. The Lagrange multiplier method enforces the constrant as it is whereas the penalty function method enforces it in a least square sence.

The variational functional in the Lagrange multiplier method is given by

$$I_L(U_i,\ \lambda) = I(U_i) + \int_B \lambda\, L(P)\, dB \tag{3.24}$$

Computing the first variation $I_L(U_i,\ \lambda)$ and comparing its integrand with the equation (3.20) yields that the Lagrange multiplier λ is indeed the negative of the pressure,

$$\lambda = -P \tag{3.25}$$

The resulting mixed formulation is given by the pair of the variational equations,

$$\int_B \delta P\, \frac{\partial U_i}{\partial x_i}\, dB = 0 \tag{3.26}$$

$$\int_B \left[\delta U_i U_j \frac{\partial U_i}{\partial x_j} + \nu \frac{\partial \delta U_i}{\partial x_j} \left(\frac{\partial U_i}{\partial x_j} + \frac{\partial U_j}{\partial x_i} \right) + \frac{P}{\rho} \frac{\partial \delta U_i}{\partial x_i} + f_i\, \delta U_i \right] dB = \int_S \frac{t_i}{\rho}\, \delta U_i dS \tag{3.27}$$

where δU_i and δP denote the variations in U_i and P , and t_i is surface traction on S in the direction of x_i,

$$t_i = \left[-P + \mu \left(\frac{\partial U_i}{\partial x_j} + \frac{\partial U_j}{\partial x_i} \right) \right] n_j, \tag{3.28}$$

whose appearance is a consequence of the application of the Green's theorem. n_j is the direction cosine of the unit vector normal to the boundary.

The penalty functional becomes

$$I_p(U_i, \gamma) = I(U_i) + \frac{\gamma}{2} \int_B [L(P)]^2 \, dB \tag{3.29}$$

here the penalty parameter γ can be determined similarly,

$$\gamma \, L(P) = -P \tag{3.30}$$

Note that Eq.(3.30) is deduced from the penalty functional, $I_p(U_i, \gamma)$; it does not form the basis of the penalty method, but is a consequence of Eq.(3.29). The resulting variational formulation by the penalty method is written by

$$\begin{aligned} &\int_B \left[\delta U_i U_j \frac{\partial U_i}{\partial x_j} + \nu \frac{\partial \delta U_i}{\partial x_j} \left(\frac{\partial U_i}{\partial x_j} + \frac{\partial U_j}{\partial x_i} \right) + \delta U_i f_i \right] dB \\ &+ \lambda \int_B \frac{\partial \delta U_i}{\partial x_i} \frac{\partial U_i}{\partial x_i} \, dB = \int_S \frac{t_i}{\rho} \, \delta U_i \, dS \end{aligned} \tag{3.31}$$

Note that in the above equation the pressure does not appear explicitly. Once the velocity field is obtained by solving Eq.(3.31), the pressure can be computed by the following relation,

$$P = -\lambda \frac{\partial U_i}{\partial x_i} \tag{3.32}$$

which is the same expression as the one in Eq.(3.30).

The penalty parameter γ should be chosen large enough so that the incompressibility and presure errors are negligible, yet not so large that a numerical ill-conditioning ensues. The criterion for the Navier-Stokes equations is

$$\lambda = c\,\mu\,Re$$

where c is a constant which depends only on the computer word length and is independent of the mesh discretization. Numerical studies reveal that for a floating-point word length of 60 to 64 bits, an appropriate choice of c is 10^7. This choice seems to be problem independent[59]. But it is not necessary to be very fussy about the selection of λ as it may vary over several orders of magnitude with an essentially insignificant effect on results.

3.3 Finite Element Approximation

The finite element method is a piecewise application of the variational methods, either Eqs.(3.26) and (3.27) or Eq.(3.31) depending on whether the mixed or penalty formulation is selected. The domain of interest is discretized into a collection of geometrically simple subdomains, called the finite elements. Over each finite element, the variational formulation is constructed and the approximation functions are derived using the basic idea that any continuous function can be represented by a linear combination of algebraic polynomials. The approximation functions are also called the interpolation functions, which do interpolate the dependent variables according to the number of nodes in the element. Integration over each element is performed via the Gauss quadrature to obtain algebraic matrix equations for the element. These element equations are asembled and superposed to yield the global matrix equations and then boundary conditions are imposed. The resulting global system of equations is nonlinear and of the form,

$$[K(U)] = F \tag{3.33}$$

where $[K]$ is the global(stiffness) matrix, U the unknown global vector composed of dependent variables, and F the global vector composed of external forces and boundary conditions.

3.3.1 Mixed Finite-Element Formulation

In the Galerkin formulation, the same approximation functions are employed in both for the functional representation of the primitive variables and the weighting functions over each element:

$$\begin{aligned}
U_I(x_j) &= \sum_{J=1}^{N} U_{IJ}\,\phi_J(x_j), \qquad \delta U_I(x_j) \sim \phi_I(x_j) \\
P(x_j) &= \sum_{J=1}^{N} P_J\,\psi_J(x_j), \qquad \delta P(x_j) \sim \psi_I(x_j) \\
k(x_j) &= \sum_{J=1}^{N} k_J\,\phi_J(x_j), \qquad \delta k(x_j) \sim \phi_I(x_j) \\
\tilde{\varepsilon}(x_j) &= \sum_{J=1}^{N} \tilde{\varepsilon}_J\,\phi_J(x_j), \qquad \delta\tilde{\varepsilon}(x_j) \sim \phi_I(x_j)
\end{aligned} \tag{3.34}$$

where

1. J is the node number in the element,
2. N is the number of nodes in the element,
3. U_{IJ} is the value of U_I at the J-th node of the element,
4. ϕ_J and ψ_J are the interpolation functions associated with the J-th node,

5. δU_i, δP, δk, and $\delta\tilde{\varepsilon}$ are the variations in each variable.

Herein the same basic functions are employed for U_i, k and $\tilde{\varepsilon}$ - an unnecessary but cost effective restriction. Note that the interpolation function for the pressure is different from the ones for the other variables. This is because P is not differentiated whereas U_i, k, and $\tilde{\varepsilon}$ are differentiated once except the source term for the wall treatment in the $\tilde{\varepsilon}$ -equation. It indicates that the interpolation functions for U_i, k, and $\tilde{\varepsilon}$ should be at least linear in each x_j if the source term in the $\tilde{\varepsilon}$-equation is out of consideration, whereas the function for P can be either a constant, which results in a chequerboard-type pressure distribution, or linear in each x_j. The substitution of the approximation functions for the primitive variables and the integration over the each element result in the following matrix equations,

$$\begin{bmatrix} K_{11} & K_{12} & K_{13} & C_1 & 0 & 0 \\ K_{21} & K_{22} & K_{23} & C_2 & 0 & 0 \\ K_{31} & K_{32} & K_{33} & C_3 & 0 & 0 \\ -C_1^T & -C_2^T & -C_3^T & 0 & 0 & 0 \\ K_{41} & K_{42} & K_{43} & 0 & K_{44} & K_{45} \\ K_{51} & K_{52} & K_{53} & 0 & K_{54} & K_{55} \end{bmatrix} \begin{bmatrix} U_x \\ U_r \\ U_\theta \\ P \\ k \\ \tilde{\varepsilon} \end{bmatrix} = \begin{bmatrix} f_x \\ f_r \\ f_\theta \\ 0 \\ f_k \\ f_\varepsilon \end{bmatrix} \tag{3.35}$$

where each component of the matrix and vectors are expressed in Appendix A. The matrix equation represents the discrete analogue of the equations (3.1) - (3.8) and the corresponding boundary conditions in an individual fluid element.

The above derivation has focused on a single finite element. The discrete representation of the entire region of interest is obtained through an assemblage of elements such that the interelement continuities of the velocity, turbulent kinetic energy,

and dissipation rate are enforced. This continuity requirement is met through the appropriate summation of equations for nodes common to adjacent elements. The result of such an assembly process is a system of matrix equations of the form given by Eq.(3.35).

3.3.2 Penalty Finite-Element Formulations

When the penalty formulation is employed, the continuity equation $C_l^T U_l$ in Eq.(3.35) is simply dropped, and the pressure is obtained by the discrete analogue of Eq.(3.32), i.e.,

$$C_l^T U_l = -\frac{1}{\lambda} M P \tag{3.36}$$

This equation can be used to eliminate P from the momentum equation and the resulting system of equations becomes

$$\begin{bmatrix} K_{11}+\lambda K_{11}^P & K_{12}+\lambda K_{12}^P & K_{13}+\lambda K_{13}^P & 0 & 0 \\ K_{21}+\lambda K_{21}^P & K_{22}+\lambda K_{22}^P & K_{23}+\lambda K_{23}^P & 0 & 0 \\ K_{31}+\lambda K_{31}^P & K_{32}+\lambda K_{32}^P & K_{33}+\lambda K_{33}^P & 0 & 0 \\ K_{41} & K_{42} & K_{43} & K_{44} & K_{45} \\ K_{51} & K_{52} & K_{53} & K_{54} & K_{55} \end{bmatrix} \begin{bmatrix} U_x \\ U_r \\ U_\theta \\ k \\ \tilde{\varepsilon} \end{bmatrix} = \begin{bmatrix} f_x \\ f_r \\ f_\theta \\ f_k \\ f_\varepsilon \end{bmatrix} \tag{3.37}$$

where each component of matrix and vectors are expressed in Appendix A. We shall be concerned here with the construction of the matrix K_{ij}^P, which is different depending on whether the reduced or consistent integration method is used.

3.3.2.1 Reduced integration method

The interpolation functions used for the velocity components in Eq.(3.34) may be substituted directly into the penalty formulation of Eq.(3.31) to obtain the Galerkin penalty finite element approximation to the Navier-Stokes equations. Then the penalty matrices are defined as

$$K_{ij}^{PR} = -\int_B \frac{\partial \phi_I}{\partial x_i} \frac{\partial \phi_J}{\partial x_j} dB \tag{3.38}$$

It should be noted that the reduced integration be taken in evaluating the penalty terms since, if the full Gauss quadrature were used, this approach is illegal because the system would be effectively overconstrained : there would be more continuity constraints than velocities to satisfy them. This exact integration of K_{ij}^{PR} would be equivalent to a particularly untenable application of an equal order interpolation for the velocity and pressure. Note also that in the reduced integration approach, the pressure basis function ψ_I does not enter explicitly into the construction of the reduced penalty matrix K_{ij}^{PR}.

Generally, the reduced integration uses a one point Gauss quadrature for multilinear elements, and a two point in each direction for multiquadratic elements. It turns out to be a piecewise constant pressure for the multilinear elements, and a discontinuous piecewise multilinear pressure for the multiquadratic elements. Thus these elements may suffer from spurious pressure modes just as do their mixed counterpart[64,196]. It was shown that if an element is fully isoparametric with curved sides, the reduced integration would introduce an integration error into the computation of the penalty matrix K_{ij}^{PR} and subsequantly an error into the computed velocity and pressure solutions[196]. This is a

serious defect for the reduced integration, since most analyses require the use of non-rectangular grids to accomodate complicate geometries. To circumvent this difficulty, the consistent penalty method was introduced [196].

3.3.2.2 Consistent integration method

The reduced integration method is equivalent to the consistent integration method only for the limited number of simple elements. In general, the consistent penalty method obtains more accurate penalty matrices than the reduced penalty method. The formulation starts with the equations (3.26) and (3.27) of the mixed formulation with a hope that the pressure term can be replaced in terms of the velocity through $P = -\lambda \frac{\partial U_j}{\partial x_j}$. The equations are brought here again:

$$\int_B P\,\delta P\,dB = -\lambda \int_B \frac{\partial U_j}{\partial x_j}\,\delta P\,dB \tag{3.39}$$

$$\int_B \left[U_j \frac{\partial U_i}{\partial x_j}\delta U_i + \nu\left(\frac{\partial U_i}{\partial x_j} + \frac{\partial U_j}{\partial x_i}\right)\frac{\partial \delta U_i}{\partial x_j} + \frac{P}{\rho}\,\frac{\partial \delta U_i}{\partial x_i} + f_i\,\delta U_i \right] dB = \int_S \frac{t_i}{\rho}\,\delta U_i dS \tag{3.40}$$

The integration functions utilized in the mixed formulation, Eq.(3.35), are used. Upon substitution, Eq.(3.39) reduces to

$$\sum_{J=1}^{N}\left[\int_B \psi_I \frac{\partial \psi_J}{\partial x_j}\, dB\right] P_J \;=\; -\lambda \sum_{J=1}^{N}\left[\int_B \psi_I \frac{\partial \phi_J}{\partial x_j}\frac{}{\partial x_j}\, dB\right] U_{JJ} \qquad (3.41a)$$

or

$$M^{IJ} P_J \;=\; -\lambda\,[C_j^{IJ}]^T U_{JJ} \qquad \text{sum on } J \qquad (3.41b)$$

where M^{IJ}, sometimes referred to as the pressure mass matrix, and C^{IJ} are defined as follows:

$$\begin{aligned} M^{IJ} &= \int_B \psi_I \psi_J\, dB \\ C_j^{IJ} &= \int_B \frac{\partial \phi_I}{\partial x_j}\, \psi_J\, dB \end{aligned} \qquad (3.42)$$

The above equation may be solved for P_J, which are substituted into the pressure term of the momentum equation. The resulting penalty matrix formulation for the pressure term becomes

$$\begin{aligned} \int_B P \frac{\partial \delta U_i}{\partial x_i}\, dB &= \sum_{J=1}^{N}\left[\int_B \psi_J \frac{\partial \phi_I}{\partial x_i}\, dB\right] P_J \\ &= -\lambda\, C_i^{IJ}\,[M^{IJ}]^{-1}\,[C_j^{IJ}]^T U_{JJ} \\ &= -\lambda\, K_{ij}^{PC}\, U_{JJ} \qquad \text{sum on } j \end{aligned} \qquad (3.43)$$

Therefore, the pressure matrix for the constistent penalty formulation is

$$K_{ij}^{PC} \;=\; C_i\, M^{-1}\, C_j^T \qquad (3.44)$$

The explicit integration of the pressure interpolation functions in this method provides the greater freedom in the construction of the penalty elements and directly identifies the discrete approximation of the constraints. It was shown that to every penalty element there corresponds an equivalent mixed element formulation. Consequently, the consistent formulation provides for the construction of very accurate and stable penalty finite element approximations by using the same interpolation function used in the best mixed elements. Since the pressure interpolation functions are explicitly introduced, the full quadrature is used to evaluate the integrals in the penalty term. The relationship between the two penalty methods and conditions for their equivalence are detailed in reference[196], where it was shown that the consistent integration of the penalty matrix is to be preferred.

3.4 Computational Domain and Mesh Generation

A computational domain, which should be taken as large as possible, is strongly restricted by the costs of computation and storage. The least requirement is that the domain stretch radially deep into the inviscid free stream region and that it contains certain finite distances upstream and downstream far enough to minimize the effect transferred from the possible defect of the specified boundary conditions.

The basic rule to a mesh generation is that the larger spatial gradients of the variables need the finer meshes. Therefore, coarser meshes are generated towards the inviscid free stream region and the exit plane, and finer meshes are generated towards walls and near the propeller. For better treatment of the wall modification for the

$k-$ and $\varepsilon-$equations at least one point should be put in the laminar sublayer on the body surface. This restricts axial lengths of elements, whose maximum aspect ratios are kept no greater than 100 to avoid a slow convergence rate. In the boundary layer at least 20 points are put to resolve large gradients. As the boundary layer grows on the slender body, the meshes near the body become thicker towards the tail of the body.

The measurements at the inlet plane were taken at 1.804 propeller diameter upstream of the propeller. This distance is considered to be reasonable as the inlet plane because the influence of a propeller on an axisymmetric stern boundary layer was found to be contained within a limited region extending two propeller diameters upstream of the propeller[3]. Since the measurements downstream of the propeller were made at 0.208 and 1.0 propeller diameters, the exit plane is chosen at 4.0 propeller diameter which is expected to be far enough. The radial distances from the axisymmetric center line are 2.4 times the propeller radius for a streamlined drag body with no propeller and also for ducted and nonducted propellers on that body. This radial distance is considered to be long enough for the flow there to be remain inviscid and to provide good boundary conditions.

4. PROPELLER MODELING AND SOLUTION PROCEDURES

4.1 Modeling of Propeller

As mentioned in the Introduction, an actutator disk is employed here to model a propeller. A disk with radius and thickness equal to the real propeller takes the place of the propeller. The disk has radial variations of thrust and torque, which are converted into body forces to generate the same effects on the flow as the actual propeller does. However, little is known about the radial distributions of the thrust and torque, but only the global magnitudes of the thrust and torque are known from experimental measurement. The radial variations are assumed to be of simple form, but their total integrated values should match the global thrust and torque.

4.1.1 Nonducted Propeller

4.1.1.1 Experimental conditions

The calculations made for a streamlined drag body and for a non-ducted propeller in this study were to be compared to experiments performed at Virginia Tech[198]. The experiments were conducted in the 6 ft by 6 ft test section of the Stability Wind Tunnel at nominal Reynolds numbers based on the body diameter of 0.45×10^6. The free stream velocity was 150 ft/sec.

The model, originally designed for the investigation of free surface effects, consisted of two axisymmetric slender bodies which were connected by a flat plate strut in the vertical plane of symmetry as shown in Fig.2. The bodies had a slenderness ratio, (L/D_0), of 15; they were 90 in. long with a diameter of 6 in. and had a streamlined nose and pointed tail. The flat plate strut was 60 in. long, 6 in. wide and 0.375 in. thick with a streamlined leading edge and a sharp trailing edge. The strut was connected to a strain gage balance which measured the drag force.

Propulsion for a nonducted propeller case was provided by a 3 hp. motor turning a three-bladed propeller with a diameter of 6 inches. The blades were twisted to 44 deg. pitch angle at 70% radius. Self-propelled and 100% over-thrusted conditions for the body were found with the strain gage balance and these occurred at the propeller rotational speeds of 12,900 rpm and 17,100 rpm, respectively.

The mean flow parameters, viz. the three components of velocity and static pressure, and the six components of the Reynolds stresses were measured at two stations in the

near wake at 0.208 and 1.0 propeller diameters downstream of the propeller plane. More details of the measurement techniques and data can be found in reference[198].

In a separate set of experiment, the boundary layer was measured carefully at 1.804 propeller diameters upstream of the propeller[199]. This location was sufficiently far upstream to be free of propeller influence. The measurements provided the specifications of three components of mean velocities and turbulence intensities at the inflow boundary for the calculations.

4.1.1.2 Estimation of thrust and torque

For the calculations, values of net thrust and torque produced by the propeller were needed. Unfortunately, from the experiments, only the rotational speeds and the fact that the experiment was self-propelled or 100% over-thrusted were known, where by self-prepelled it is meant that the thrust generated by the propeller is equal to the drag and by 100% over-thrusted twice the drag. An additional fact was also known which allows a calculation of thrust and torque. Without the propeller operating, the drag coefficient of the body alone was measured as 0.19 and the drag coefficient of the body and flat plate strut was 0.25 based on the cross-sectional area of the body. The equivalent rotational speeds for the axisymmetric self-propelled and over-thrusted cases are 11,900 rpm and 15,100 rpm, obtained by inter- and extrapolation of two rotational speeds of 12,900 rpm and 17,100 rpm for both of the nonaxisymmetric cases.

The pressure distribution on the aft portion of the body is changed by the propeller in operation, so that an augmented drag factor, otherwise known as a thrust deduction

fraction, must be added to the drag coefficient of 0.19. The coefficient of drag of 0.19 produces a thrust in the absence of interaction, T_0, of 0.917 lb.

Following the method in reference[200], the augmented thrust is calculated for the self-propelled case. The nominal thrust coefficient, C_{T0} , is calculated.

$$C_{T0} = \frac{T_0}{\frac{1}{2}\rho_\infty U_\infty^2 (\pi \frac{D_P^2}{4})} = 0.19 \tag{4.1}$$

where D_P is the propeller diameter. The wake fraction, w_f , is calculated from the axial velocity distribution at the propeller location without the propeller operating.

$$w_f = \frac{\int_0^{2\pi} \int_0^{\frac{D_P}{2}} (1 - \frac{U}{U_\infty})\, r\, dr\, d\theta}{\pi \frac{D_P^2}{4}} = 0.147 \tag{4.2}$$

which was obtained from the solution of the wake behind a slender body. With these quantities, the thrust deduction fraction, f_{th}, is calculated.

$$f_{th} = 2w_f \left[\frac{(1 + C_{T0})^{1/2} - 1}{C_{T0}} \right] = 0.140 \tag{4.3}$$

The augmented thrust with the propeller operating, T, can then be calculated.

$$T = \frac{T_0}{1 - f_{th}} = 1.07 \text{ lb} \tag{4.4}$$

With no direct information on the efficiency of the propeller available, a value of 70% was taken as a reasonable value for this type of propeller[83] and torque was calculated as

$$Q = \frac{T U_\infty}{2\pi n \eta} \tag{4.5}$$

where n is a number of revolution per second and η is the efficiency of the propeller. Torque for the self-propelled case was calculated as 0.184 lb-ft. Likewise for the 100% over-thrusted case, thrust was calculated at 2.12 lb and torque at 0.287 lb-ft. The efficiency was assumed to remain at 70% also.

The thrust and torque coefficents, expressed as

$$K_T = \frac{T}{\rho_\infty n^2 D_P^4}$$
$$K_Q = \frac{Q}{\rho_\infty n^2 D_P^5}, \tag{4.6}$$

are calculated as 0.199 and 0.0683 for the self-propelled case, and 0.245 and 0.0664 for the over-thrusted case, respectively.

4.1.1.3 Propeller modeling

The propeller is modeled as an actuator disk of radius equal to the actual radius of the propeller and a thickness, Δt, roughly equal to the actual thickness of the propeller. The thrust and torque are allowed to vary radially, but are constant in the tangential direction. The actual distribution of thrust and torque radially along the propeller is not

known. An engineering rule of thumb[40] is used to center the maximum thrust around the 70% radius of the propeller and to make the distribution of torque similar. Therefore, a simple trapezoidal distribution of thrust is adopted with thrust beginning at the hub and increasing linearly to a plateau of maximum thrust surrounding the 70% radius location and then dropping to zero at the tip. And as towards the tip the incidence and the chord length of the blade reduce, the magnitude of torque towards the tip is diminished[81-83]. The assumed distributions of the thrust and torque are shown in Fig. 20(a), where t_m is the maximum value of the thrust, q_{m1} and q_{m2} are the values of the torque at r_2 and r_3, and R_p is the radius of the propeller. The values of r_1, r_2, and r_3 were set to 0.0834, 0.474, and 0.925 R_p, respectively. This is not a unique choice, but it is based on experience with the predictions of simple propeller preformance codes for propellers of this type[40,41,201,202]. The same form is adopted for the distribution of the torque, q, producing the swirl. Its maximum value is denoted by q_m. The upstream face of the propeller disk is located at $x/D_0 = -\Delta t/D_0 = -0.0417$, while the downstream face of the propeller is located at $x/D_0 = 0.0$. These distributions are integrated to yield the global thrust and torque of the propeller:

$$T = \int\int_{A_p} r\, t(r,\theta)\, dr\, d\theta = 2\pi \int_{R_p} r\, t_r(r)\, dr \tag{4.7}$$

$$Q = \int\int_{A_p} r^2\, q(r,\theta)\, dr d\theta = 2\pi \int_{R_p} r^2\, q_r(r)\, dr \tag{4.8}$$

where A_p is the propeller disk area. This integration results as:

$$T = 0.209\, \pi\, t_m \tag{4.9}$$

and

$$Q = 0.0583\,\pi\,q_m \tag{4.10}$$

where $q_{m1} = q_m$ and $q_{m2} = 0.61q_m$ are used. From the measured global thrust and torque the values of t_m and q_m can be obtained.

The values of the body forces, f_t and f_q, used in the finite element code are arrived at by nondimensionalizing t_m and q_m and dividing by the thickness of the propeller.

$$f_t = \frac{T}{0.209\,\pi\,\rho_\infty\,U_\infty^2\,D_0^2\,\frac{\Delta t}{D_0}} \tag{4.11}$$

$$f_q = \frac{Q}{0.0583\,\pi\,\rho_\infty\,U_\infty^2\,D_0^3\,\frac{\Delta t}{D_0}} \tag{4.12}$$

For the self-propelled and over-thrusted cases, this resulted in the dimensionless values for the body forces, f_t of 3.045 and 6.299, and f_q of 4.100 and 6.126, respectively.

4.1.2 Ducted Propeller

The present investigation is aimed at comparison of wakes downstream of the propeller with and without a duct. For this purpose, a ducted propeller was located at the same position of the same slender body, and its net thrust and torque are kept the same as the ones for the nonducted, self-propelled condition. Since the duct increases overall drag of the propulsive system, the magnitude of the global thrust generated by the propeller and duct should be increased. The drag of the duct is not known a priori.

Therefore, the momentum differences of both cases between two points somewhere far upstream and downstream must be compared.

4.1.2.1 Determination of duct shape

For better and easier comparisons, most of the conditions employed for the computation of the self-propelled case remain fixed except the global magnitudes and radial diatributions of thrust and torque. For simplicity, a straight converging nozzle with zero thickness was chosen as a duct in this study. The specifications of the duct are as follows:

clearance between duct and blade tip = 0.06 in.,
duct length = 3 in., $-0.25D_0$ to $0.25D_0$
propeller location in duct = 50% from the leading edge of duct,
duct incidence = 4.0 deg.

The duct is aligned well with the streamlines so that no separation occurs on both sides of the duct. The incidence was determined to satisfy the condition of no separation.

4.1.2.2 Distribution of thrust and torque

It should be mentioned that the combination of the duct, propeller, and body is not optimal; in other words the incidence of the duct, duct length, duct location, clearance, and most importantly the radial distributions of thrust and torque are not necessarily best choice. The basic reasons for ducting a propeller are that the radius of the propeller is reduced, the number of blades are increased, and the blades are generally wider

towards their tips. However, in this study the radius of the blades was not changed, and the actuator disk model does not account for the number of blades.

Estimating the radial distributions of thrust and torque, we start with a typical distribution of circulation, $\Gamma(r)$, around a blade of a ducted propeller[6]. The global thrust and torque can be expressed as

$$T = 2\pi \int_{R_p} r\, t_r(r)\, dr = Z \int_{R_p} \rho\, \omega\, r\, \Gamma(r)\, dr \tag{4.13}$$

and

$$Q = 2\pi \int_{R_p} r^2 q_r(r)\, dr = Z \int_{R_p} \rho\, V_x(r)\, r\, \Gamma(r)\, dr \tag{4.14}$$

In the above equations Z denotes the number of blades, $\omega (= 2\pi n)$ the angular velocity of the propeller in rad/sec, and $V_x(r)$ the radial profile of axial velocity of flow. From the above equations

$$t_r(r) = \frac{Z\rho\omega}{2\pi} \Gamma(r) \tag{4.15}$$

and

$$q_r(r) = \frac{Z\rho}{2\pi} \frac{V_x(r)\Gamma(r)}{r} \tag{4.16}$$

are obtained. The thrust per unit area, t_r, which has the same shape as Γ, and the torque per unit volume, q_r , are shown in Fig. 20(b). t_{m1} and t_{m2} are the values of the thrust at r_2 and r_3 and q_m is the maximum value of the torque. The values of r_1, r_2, and r_3 were set to 0.0834, 0.30, and 0.90 R_p, respectively. The global thrust and torque generated by the propeller alone for the self-propelled condition are calculated at 1.324 lb and 0.184 lb-ft, of which the thrust is 24 % larger than that of the nonducted self-propelled value, and

the torque remains the same as the one for the nonducted propeller, but the efficiency drops to 56.5%. The equivalent body forces are 3.281 at r_2 and 4.174 at r_3 for the thrust and 4.054 for the torque.

4.2 Solution Procedures

4.2.1 Nondimensionalization

The governing equations are cast into nondimensionalized form for normalization[203]. The reference values for such procedure are the length D_0(body diameter), velocity U_∞ (free stream velocity), viscosity μ_∞ or ν_∞, and density ρ_∞. By using these quantities the following nondimensionalized variables can be obtained:

$$
\begin{aligned}
x_i^* &= \frac{x_i}{D} & \rho^* &= \frac{\rho}{\rho_\infty} \\
U_i^* &= \frac{U_i}{U_\infty} & u_i^* &= \frac{u_i}{U_\infty} \\
P^* &= \frac{P}{\rho_\infty U_\infty^2} & \sigma_{ij}^* &= \frac{\sigma_{ij}}{\rho_\infty U_\infty^2} \\
t_i^* &= \frac{t_i}{\rho_\infty U_\infty^2} & f_i^* &= \frac{D}{\rho_\infty U_\infty^2} f_i \\
k^* &= \frac{k}{U_\infty^2} & \varepsilon^* &= \frac{D}{U_\infty^3} \varepsilon \\
Re_D &= \frac{\rho_\infty U_\infty D}{\mu_\infty} & P_k^* &= \frac{D}{U_\infty^3} P_k \\
\mu^* &= \frac{\mu_\infty}{\rho_\infty U_\infty D} = \frac{1}{Re_D} & \mu_t^* &= \frac{\mu_t}{\rho_\infty U_\infty D} = \frac{1}{Re_D} \frac{\mu_t}{\mu_\infty} \\
\lambda^* &= \frac{\lambda}{\rho_\infty U_\infty D}
\end{aligned}
\tag{4.17}
$$

where the nondimensionalized variables are denoted by an asterisk. λ is a penalty parameter and all other variables are defined at the previous section.

The nondimensionalized equations are expressed by Eq.(A.1) through Eq.(A.10) in Appendix A. It should be mentioned that even the turbulence transport equations are nondimensionalized by the velocity and length scales of the mean field quantities in free stream. If the k- and ε-equations are nondimensionalized by the turbulence velocity (u_*, friction velocity) and length ($l \sim \frac{k^{3/2}}{\varepsilon}$) scales, then there should be extra factors, for example, $(U_\infty/u_*)^2$ in the production term of the k –equation.

The consequence of nondimensionalization lies in the following two aspects. First, the better conditioning of the global matrix can be obtained. Second, by choosing properly the values for the reference velocity and length, the variables are normalized so that their values are limited between certain prescribed limits.

4.2.2 Solution Methods

The application of the Galerkin finite element method to the stationary Navier-Stokes and turbulent transport equations results in a set of nonlinear algebraic equations that may be represented in matrix form as

$$[\, K(\Delta,\, v_i(\Delta))\,] \;=\; F \tag{4.18}$$

where K is the global system matrix, Δ is the global vector of unknowns, $[U_z,\ U_r,\ U_\theta,\ k, \tilde{\varepsilon}]^T$, and F is a vector which includes the effects of the body forces and boundary conditions. Pressure is recovered explicitly by using the consistent integration of penalty function formulation. The extra source terms in $k-$ and $\varepsilon-$equations for the treatment of wall effects are included in Eq.(4.14); however, these source terms are simply neglected in fully turbulent region, say $y^+ > 100$. It is generally known that the wall influence becomes negligible beyond y^+ of 60[105,181]. The wall correction parameter f_μ for c_μ asymptotically approaches to a value of 1 near y^+ equal to 100.

Since the set of equations is highly nonlinear, an effective iterative procedure is a key issue. Newton type methods, Newton-Rapson and Quasi-Newton, have a quadratic convergence rate, but they suffer a small radius of convergence. Many earlier researches reported that an inconveniently extremely good initial guess was necessary to achieve

convergence of Newton method when using $k-\varepsilon$ turbulence model[18,80,85]. The successive substitution is used throughout the iterations simply because it has a large radius of convergence to contain the sensitive variables k and ε. At each iteration an exact solution is obtained by inverting the global stiffness matrix through L/U decomposition.

To start the iteration process, a Stokes' flow solution is obtained as an initial guess for all problems solved in this work. And, to enhance the convergence rate, a weighted sum of the last solution and the last but one is used for the updated solution vector for linearization:

$$\{\Delta\} = \alpha\{\Delta\}^n + (1-\alpha)\{\Delta\}^{n-1} \tag{4.19}$$

where n denotes the iteration number and α, $0 \le \alpha \le 1$, is an acceleration parameter. Complex turbulent problems with sudden changes in variables are often dealt with by using under-relaxed iterative techniques which can be controlled iteration by iteration. The ralaxation parameter, α, remains between 0.4 and 0.8 throughout the iterations for all problems. This iteration process continues until the L_2-norm of the relative error of the solution vector drops to no greater than 10^{-4} for the first three problems and 10^{-3} for the ducted propeller.

Solutions are often corrupted by spurious node-to-node oscillations or wiggles. Wiggles are likely to appear in convection dominant flow when a rapid change in the solution occurs due to large gradients in flow. The only way to eliminate the oscillations is to severely refine the mesh, such that convection no longer dominates on an element level. It was discovered, however, that wiggle-free solutions could be obtained by the use of upwind differencing on the convective term. Upwind differencing amounts to

approximating the convective derivatives with solution values at the upstream and central nodes of a three-node stencil. It is well known that the Galerkin finite element method gives rise to central-difference type approximations of differential operators. It is thus not surprising that wiggles have also afflicted central-difference finite difference solutions[205].

The drawback is that upwind differences are only first-order accurate(central differences are second-order accurate). The loss of accuracy is manifested as overly diffuse solutions. It is well known that the upwinded convective term can be constructed simply by adding artificial diffusion to a difference treatment. The oscillations in axial velocity, turbulent kinetic energy, and eddy viscosity in front of the propeller plane are removed by adding the streamline upwind[55].

5. RESULTS AND DISCUSSION

Applications of the $k-\varepsilon$ turbulence model with the wall and swirl treatments previously described have been made to four problems:

1. flow through a sudden pipe expansion,
2. the stern region flow of an axisymmetric slender body,
3. flow past a propeller on the same body operating at two rotational speeds,
4. flow past a ducted propeller on the same body.

The modification was interfaced to the existing fluid dynamics program FIDAP[12] using the finite element method. The resulting code can simulate any kind of two-dimensional and axisymmetric swirling flow problems and can be extended for applications to three-dimensional flow simulations.

5.1 Sudden Pipe Expansion

5.1.1 Solution Informations

The simulation of a turbulent flow through a sudden enlargement of a pipe is one of the very interesting problems against which many workers in turbulence like to test their turbulence models and computer codes. The key features this flow has are a sudden separation from wall, recirculating motion downstream of the step, corner eddy, splitting of a shear layer at reattachment, redevelopment of a sub-boundary layer downstream of the reattachment, and self-adjusting motion of the flow in the central region to varying environments as shown in Fig. 2(a). This problem constitutes a good validation test of the wall modification as well as the basic turbulence model.

The characteristics chosen for this problem are as follows:

pipe diameter, $D = 0.81$ ft

enlarged pipe diameter, $D_L = 1.215$ ft

step height, $H = \frac{1}{2}(D_L - D) = 0.2025$ ft

expansion ratio, $D_L/D = 1.5$

velocity at center at inlet boundary, $U_0 = 10.0$ ft

air density, $\rho_0 = 0.002378$ slug/ft^3

Reynolds number, $Re_D = \rho U_0 D/\mu = 50{,}000$

Experiments[13-16,36] of similar conditions are available for comparison with the present predictions. At the inlet boundary the flow was assumed to be fully developed.

The boundary conditions at the inlet plane were obtained from Laufer's experiment for a fully developed pipe flow[204], which carries extensive measured data even for the turbulent quantities. The other boundary conditions are shown in Fig. 2(b).

The pressure gradient, $-dP/dx$, was measured at 2.055×10^{-3} lb/ft^3 , from which the friction velocity at the inlet can be calculated as follow: The pressure drop is caused by the viscous shear on the pipe wall, and therefore, the wall shear stress can be obtained as

$$\tau_w = -\frac{a}{2}\frac{dP}{dx} = 0.416 \times 10^{-3} \frac{\text{lb}}{\text{ft}^2} , \tag{5.1}$$

where a is the radius of the pipe. The friction coefficient, $C_f (= 2\tau_w/\rho U_0^2)$, was calculated at 0.0035 and the fricition velocity, u_*, resulted in 4.18% of the central velocity.

The inlet and exit planes are located at 4 step heights upstream and 20 step heights downstream of the step. The downstream boundary is about 2.5 times reattachment distance, so that the boundary conditions do not affect the reattachment distance. The generated mesh has 2492 elements and 2616 nodal points, 17 and 29 nodes radially and 14 and 82 axially in each guiding and enlarged pipes as shown in Fig. 2. A few points from the wall are put in the sublayer to treat the wall influences effectively. Linear isotropic elements are used and the penalty function formulation with the consistent integration method for pressure recovery is employed. Each node has 4 unknowns and the total number of unknowns after reduction for boundary conditions is 9,873.

The equations of motion are nondimensionalized with respect to D, U_0, and ρ_0 . The initial guess is provided by a Stokes' flow solution for the velocity field with constant values of 0.001 for both k and ε The nonlinear system of equations was solved by

successive substitution with underrelaxation, the value of which is taken at 0.5. The clipping process for k, ε, and μ_t for better convergence rate, which limits the maximum and minimum values, was required in the early stage of the iteration. The computing time for each iteration was 39 seconds on an IBM 3091 vector compiler at optimization level 3 and 30 iterations were required for the L_2 −norm of the relative error of solution vector with respect to the Stokes' flow solution to reach no greater than 10^{-4}.

5.1.2 Comparison with Measurements and Other Predictions

The calculated streamlines and velocity vectors are drawn in Fig. 3, which apparently shows the streamline split and recirculation zone. Fig. 4 demonstrates the friction coefficient variation along the pipe wall downstream of the step. The reattachment distance is predicted where C_f becomes zero at 7.4 step heights downstream of the step, resulting in a good agreement with measurements[13-16] and other predictions by the $k-\varepsilon$ models[20-22] and the Reynolds stress model[23]. The measured reattachment distances are 6 to 9 step heights as can be seen in Fig. 5. Generally, the reattachment distance is dependent on the inflow conditions, pressure gradient, step height ratio, and Reynolds number. The maximum velocity of the reversed flow, according to this figure, occurs around 3 step heights downstream of the step and reaches 10% of the central velocity at the same axial location. The small values in C_f right behind the step indicate the corner eddy, missing in the streamline plot.

The axial velocity and the turbulent kinetic energy profiles at the eight different stations downstream of the step are shown in Figs. 6 and 7. The reversed flow before the reattachment and the newly generated sub-boundary layer growth behind it are well

demonstrated in the velocity plot. The flow in the central region loses its momentum to share with the flow in the outer part and gains turbulence transported laterally which stems from the step. Near the wall, the turbulence is gradually increased as the new boundary layer begins to grow up. It should be noted that the maximum turbulent kinetic energy occurs between the step and the reattachment point according to Fig. 7. The value and trace of the maximum turbulent kinetic energy along the streamline direction are plotted in Fig. 8 with the axial distance nondimensionalized by the reattachment distance for the comparison with a couple of measurements for flow over a backward facing step[36]. The point of the maximum turbulent kinetic energy moves outwards as the streamlines do, while after the reattachment, it moves inwards as the sub-boundary layer grows. The overall maximum turbulent kinetic energy occurs about 1 step height upstream of the reattachment point which is in an excellent agreement with the observation of Eaton and Johnston[36], where they surveyed about 20 experiments and came to that conclusion.

5.2 Stern Region Flow of an Axisymmetric Slender Body

5.2.1 Experimental Conditions and Solution Method

The simulation of a turbulent flow in the stern region of a slender axisymmetric body corresponds to the experiment of Mitra *et al.*[196]. This study provides the nominal wake field at the location of a propeller, which is necessary to calculate the adjusted thrust and torque of the propeller. The characteristics of the experiment are as follows:

free stream velocity, $U_0 = 210$ ft/s

free stream air density, $\rho_0 = 0.002186$ slug/ft^3

Reynolds number, $Re_D = \rho_0 U_0 D_0/\mu = 0.60 \times 10^6$

body diameter, $D_0 = 0.5$ ft

measured locations, $X_m = 0.021$ and 0.5 ft behind body tail

The inflow boundary is located 1.804 body diameters upstream of the body tail, where the boundary layer measurements were made. The outflow plane stands at 4 body diameters downstream of the body tail to see the development of the wake behind the body tail, while the free stream boundary stretches out to 1.2 body diameters where the flow can be considered to be fully inviscid, as shown in Fig. 9(a). The boundary conditions are well described in Section 3.1 and in Fig. 9(b). Briefly, the boundary values at the inlet plane were supplied from the measurement, and no slip conditions on the body surface and the traction-free and flux-free boundary conditions at the open ends were employed except the radial velocity along the axisymmetric line specified as zero.

From the measurement, the boundary layer thickness at the inlet plane is 0.075 ft. from the body surface. The Reynolds number based on the free stream velocity U_0 and the boundary layer thickness δ at the inlet plane is 90,000. At this Reynolds number the skin friction coefficient can be estimated from the skin friction law,

$$\sqrt{\frac{2}{C_f}} = A \log \left(Re_\delta \sqrt{\frac{C_f}{2}}\right) + C - B, \tag{5.2}$$

where 5.6, -2.5, and 4.9 were suggested for the values of A, B, and C [105]. The above formula was obtained from the defect law and the law of the wall, which are valid only for a flow over flat plate without a pressure gradient. But, this formula can give a rough value for C_f of 0.00272, which is required for the wall treatment for the

$k-$ and ε –equations. The friction velocity, $u_*(=\sqrt{\frac{\tau_w}{\rho}})$, calculated from the friction coefficient is 3.69% of the free stream velocity.

The generated mesh has 2,496 elements and 2,607 nodal points, 33 nodes radially and 79 nodes axially. The first point from the body is well inside the sublayer to treat the wall influences effectively. To account for the boundary layer growth, the mesh near the body becomes thicker in the direction of streamline. Linear isotropic elements are used and the penalty function formulation with the consistent integration method for a pressure recovery is employed. Each node has 4 unknowns and the total number of unknowns after the reduction for boundary conditions is 10,068.

The equations of motion are nondimensionalized with respect to D, U_0, and ρ_0. The initial guess is provided by the Stokes' flow solution for the velocity field with constant values of 0.001 for both k and ε The nonlinear system of equations was solved by the successive substitution with underrelaxation, the value of which is taken at 0.5. A clipping process was employed in the early stage of iterations for forcing convergence. The computing time for each iteration was 47 seconds on the IBM 3091 vector compiler at an optimization level 3 and 18 iterations were required for the L_2 –norm of the relative error of solution vector with respect to Stokes' solution to reach no greater than 10^{-4}.

5.2.2 Comparison with Measurements and Analysis

The measurements[196] for the two components of the mean flow velocity, pressure, and the six components of the fluctuating velocity correlations were made at two stations downstream of the propeller, $x/D_0 = 0.042$ and 1.0. The data used for comparison with these axisymmetric calculations are along the radius straight below the

body. In Figs. 10 through 13, the predicted results are compared with the measured data along that radial direction at two locations behind the propeller. The axial velocity predictions are in an exellent agreement with the measurements except in the central region right behind the slender body tail, where the prediction shows a slower momentum buildup.

The radial velocities from the measurements were expected to be larger than they should be because of the velocity defect due to the presence of the flat plate strut on the body top. Behind the body, the flow direction is off upward to fill the momentum deficit. This fact can be clearly seen in Fig. 11. Away from the centerline, the upward velocity was measured much larger than the calculated values and did not fall down even in the free stream region. At station $x/D_0 = 1.0$, a zero radial velocity occurred at $r/D_0 = 0.1$ below the centerline.

The radial variations of the pressure coefficient, $C_P = (P - P_{ref})/\frac{1}{2}\rho_0 U_0^2$, are predicted very well at $x/D_0 = 0.042$, but are more gradual than the data measured at $x/D_0 = 1.0$. This also might be due to the three-dimensional effects mentioned above. The flow might have been vertically readjusted downstream to end up with the smaller pressure gradient.

The turbulent kinetic energy is examined in Fig. 13. The predicted data reveal less radial transport than the measurements. The maximum turbulent kinetic energy calculated around $r/D_0 = 0.10$ and 0.11 at two stations of $x/D_0 = 0.042$ and 1.0, while the maximum turbulent kinetic energy measured inside of $r/D_0 = 0.16$ at two stations. The calculated peak values are about 20 % higher than the measured values. This is much better prediction than the one, 35 % higher prediction than the measured data of a similar experiment[43], obtained by the formulation of the vorticity-stream function

with an integrated turbulent kinetic energy equation solved by Schetz *et al* [41]. The sharp extremum of the turbulent kinetic energy at $x/D_0 = 0.042$ on the centerline is due to the large radial gradient of the axial velocity as shown in Fig. 10.

The boundary layer profiles for the tangential velocity and turbulent kinetic energy predicted at five different locations on the body surface are presented in Figs. 14 and 15. RW($= r - r_w$) denotes the normal distance from the body surface at each axial location. The boundary layer growth is illustrated well and its thickness at $x/D_0 = -0.2$ is about twice that at inlet plane, $x/D_0 = -1.8$. Generally, the point with the maximum turbulent kinetic energy is located around at $y^+ = 20$, but due to the convex geometry the point of the peak turbulent kinetic energy moves away from the body surface.

The skin friction coefficient on the surface is shown in Fig. 16. It is deduced from the nearest three tangential velocities to the body surface including zero velocity at the surface, which provides the values of the second order of accuracy. The estimated friction coefficient, C_f of 0.00272, at the inflow boundary is proved to be an excellent choice according to this figure. Note that the skin friction coefficent near the body tail is diminished to about 1/3 of that at the inlet plane. The occurrence of wiggles around the inlet plane is due to the inaccurate boundary conditions very near the body surface, where measured data were not provided. The streamline upwinding is employed, but there still remain wiggles, which can be removed by providing better inlet boundary conditions and/or by increasing upwinding effects.

The predicted wake downstream of the body are illustrated in Figs. 17 and 18. At station $x/D_0 = 0.042$ the axial velocity profile is similar to the boundary layer profile, while after $x/D_0 = 1.0$ it turns into the normal wake profile with inflection points. The centerline velocity gains momentum and the width of the wake grows. The similarity

between the velocity profiles are not obtained. The sharp peak of the turbulent kinetic energy coming off from the body tail disappears as the flow proceeds downstream and the points of the maximum velocity gradient and maximum turbulent kinetic energy move outwards as the width of the wake grows. The maximum value of the turbulent kinetic energy also diminishes downstream.

5.3 Nonducted Propeller

5.3.1 Solution Informations

This simulation of a turbulent shear flow past a propeller operating at two rotational speeds behind a slender body of revolution corresponds to the experiment of Mitra at al[197]. The characteristics of the experiment were mentioned in detail in Chapter 4.

The inflow boundary is located 1.804 body diameters upstream of the propeller, where the boundary layer measurements were made. The outflow plane stands at 4 body diameters downstream of the propeller, while the free stream boundary stretches out to 1.2 body diameters, as shown in Fig. 19(a). The boundary conditions are basically the same as the ones for the wake behind a streamlined body explained earlier. See Fig. 19(b).

The skin friction coefficient at the inlet plane was obtained by the same way explained in the previous section. The Reynolds number based on the free stream velocity U_0 and the boundary layer thickness δ at the inlet plane is 58,000. At this

Reynolds number the skin friction coefficient C_f resulted in 0.00292 and the friction velocity u_* was 3.82% of the free stream velocity.

The selected mesh has 2,607 elements and 2,720 nodal points, 34 nodes radially and 80 nodes axially. The first point from the body is well inside the sublayer to treat the wall influences effectively. To account for the boundary layer growth, the mesh near the body becomes thicker in the direction of streamline. Linear isotropic elements are used and the penalty function formulation with the consistent integration method for a pressure recovery is employed. Each node has 5 unknowns and the total number of unknowns after the reduction for boundary conditions is 13,147.

The equations of motion are nondimensionalized with respect to D, U_0, and ρ_0. The initial guess for the self-propelled case is provided by the Stokes' flow solution for the velocity field and constant values of 0.001 for both k and ε and for the over-thrusted the converged solution of the self-propelled. The nonlinear system of equations is solved by the successive substitution with underrelaxation, the value of which is varied between 0.5 and 0.7 for the better convergence rate. The computing time for each iteration was 74 seconds on the IBM 3091 vector compiler at an optimization level 3, and 37 and 14 iterations for both cases respectively were required for the L_2 −norm of the relative error of solution vector with respect to Stokes' solution to reach no greater than 10^{-4}.

5.3.2 Analysis for Self-Propelled Case

The measurements[197] for the three components of the mean flow velocity, pressure, and the six components of the fluctuating velocity correlations were made at two stations, $x/D_0 = 0.208$ and 1.0, downstream of the propeller. The data used for

comparison are the one straight below the body. In Figs. 21 through 25 the simulated results are compared with the measured data along the radial direction at two locations behind the propeller. The axial velocity predictions are in an exellent agreement with the measurements except in the central region right behind the slender body tail, where the prediction shows a faster momentum buildup.

The radial velocities at the centerline of the measurements were off from zero values due to the aforementioned three-dimensional effects. If zero correction is made, the predictions at two locations of $x/D_0 = 0.208$ and 1.0 are in a good agreement with the measured values. The maximum radial velocity predicted at station $x/D_0 = 0.208$ reaches 4.3% of the free stream velocity and occurs at $r/D_0 = 0.27$, while it was 3.3% at $r/D_0 = 0.23$ for the case without the propeller shown in Fig. 11. This illustrates the strong contraction of streamlines caused by the propeller action. The radial velocity quickly relaxes downstream.

Fig. 23 presents the swirl profiles in the radial direction, which are entirely dependent on the torque distribution. The predicted values compare very well with the measured data except in the central region. The swirl velocity is slightly greater at $x/D_0 = 1.0$ than at $x/D_0 = 0.208$ and the maxmum values occur between $r/D_0 = 0.17$ and 0.25 and reach 20% or more of the free stream velocity. The maximum torque for the calculation was given at $r/D_0 = 0.237$, where the predicted circumferential velocities have their maximum magnitudes, which are also in a fair agreement with the measurement. The swirl velocity can be improved further by providing a more realistic torque distribution.

The pressure coefficients compare well away from the centerline at two stations, but show some discrepancies in the central region as seen in Fig. 24. This also might be due

to the reason of nonaxisymmetry explained earlier. The augmented pressure due to the propeller action relaxes quickly down below the free stream reference pressure in the central region at the station of $x/D_0 = 1.0$. Further analysis will be followed later in the pressure contour plot.

The turbulent kinetic energy, one of the major concerns, is plotted in Fig. 25 for both the predicted and the measured values. The comparison cannot be direct because of the periodic large-scale mean motion with high frequencies emanating from the three-bladed propeller. The time scale of the periodic mean motion is about 1.55×10^{-3} seconds at 12,900 rpm. The characteristic time scale of the turbulent motion can be obtained using the calculated k and ε. Those nondimensionalized values are approximately 0.005 and 0.0035 at $x/D_0 = 1.0$ near the centerline. The dimensional values are

$$k \simeq 0.005\, U_0^2 = 112.5 \text{ ft}^2/\text{sec}^2,$$
$$\varepsilon \simeq 0.0035\, U_0^3/D_0 = 23{,}400 \text{ ft}^2/\text{sec}^3,$$

and from these quantities

$$u = \sqrt{k} = 10.6 \text{ ft/s},$$
$$L = k^{3/2}/\varepsilon = 0.0505 \text{ ft},$$
$$t = L/u = 4.76 \times 10^{-3} \text{ sec},$$

where u, L, and t denote the characteristic velocity, length, and time scales. Since both the times scales are of the same order of magnitude, the X-wire probes measured not only the fluctuating velocities but also the periodic mean-motion velocities. The captured data shown in the figure was obtained by averaging for three seconds. The high level of the peak values of the turbulent kinetic energy around $r/D_0 = 0.413$, where the maximum thrust occurs, is not only because of the high turbulence caused by the

trailing vortices, but also because of the large-scale pulsating motion. Therefore, the comparison with the measured data is not meaningful. However, at two points on the axisymmetric line, the measured and the predicted values show good agreement. The comparison with and without the propeller operation can be made. From Figs. 13 and 25, the maximum values of the turbulent kinetic energy are increased by about 33% at two stations, but the peak points are shifted into the central region at $x/D_0 = 0.208$ by the streamline contraction and away from the center line at $x/D_0 = 1.0$.

The boundary layer profiles for the tangential velocity and turbulent kinetic energy predicted at five different locations on the body surface are presented in Figs. 26 and 27. The notation $RW(= r - r_w)$ denotes the normal distance from the body surface at each axial location. The boundary layer grows and its thickness at $x/D_0 = -0.2$ is more than twice that at the inlet plane, $x/D_0 = -1.8$. At station $x/D_0 = -0.2$ it is clearly seen that the flow is pulled forward around $r/D_0 = 0.4$. The development of the turbulent kinetic energy shows the similar shape and magnitude as that without propeller operation. The convex geometry makes the point of the peak turbulent kinetic energy move away from the body surface.

The skin friction coefficient on the body surface is shown in Fig. 28. The estimated friction coefficient at the inlet plane, C_f of 0.00292, is shown to be underpredictive. In fact, the skin friction law, Eq.(5.1), is valid only for the flow with no pressure gradient. Note that the skin friction coefficient at the propeller location is diminished to about 1/4 of that at the inlet plane. Upstream of the propeller the magnitude of the skin friction when the propeller operates is increased by 30% to 50% over the case without the propeller. However, the skin friction reduces quickly around the propeller because the flow is pulled away from the body surface by the propeller action.

The pressure contour plot in Fig. 29 describes the sudden jump across the propeller and the relaxation centered at 1.7 body diameters downstream of the propeller. The relaxed pressure is even smaller than the free stream reference pressure. The contour lines steming from the inlet plane is due to a defect in the boundary condition. A small defect in the continuity condition resulted in the large pressure near the inlet plane, which is typical phenomenon in the penalty function method. This defect in pressure does not seem to affect the flow field noticeably. It should be mentioned that the values in the legend represent the nondimensinalized pressure, $(P - P_{ref})/\rho_0 U_0^2$, which is twice the nominal pressure coefficient.

The predicted wake downstream of the propeller is illustrated in Figs. 30 and 31. The accelerated flow around $r/D_0 = 0.4$ maintains its momentum, while the wake in the central region coming off from the body tail continuously gains momentum and expands laterally. The turbulent kinetic energy also transports radially, but the maximum value gradually reduces.

5.3.3 Analysis for Over-Thrusted Case

The measurements[197] for the three components of the mean flow velocity, pressure, and the six components of the fluctuating velocity correlations for the over-thrusted condition were made at the same two stations, $x/D_0 = 0.208$ and 1.0, downstream of the propeller as the self-propelled condition. The data used for comparison are the one straight below the body. In Figs. 32 through 36, the simulated results are compared with the measured data along that radial direction at two locations

behind the propeller. The axial velocity predictions are in a good agreement with the measurements except the outer region than the propeller diameter.

The radial velocities at the centerline of the measurements were off from zero values due to the aforementioned three-dimensional effects. If zero correction is made, the predictions at two locations of $x/D_0 = 0.208$ and 1.0 are in a fair agreement with the measured values. The maximum radial velocity predicted at station $x/D_0 = 0.208$ reaches 6.2% of the free stream velocity and occurs around $r/D_0 = 0.40$, while it was 4.3% at $r/D_0 = 0.27$ for the self-propelled and 3.3% at $r/D_0 = 0.23$ for the case without the propeller shown in Figs. 22 and 11. This shows that the larger power makes the streamlines more contracted even when the total speed increase due to the larger power is accounted for.

Fig. 34 presents the swirl profiles in the radial direction, which are entirely dependent on the torque distribution. The predicted values compare very well with the measured data. The different feature of the swirl velocity for the over-thrusted case from the self-thrusted is that the region in which the maximum velocity is greater at $x/D_0 = 1.0$ than at $x/D_0 = 0.208$ is confined around $r/D_0 = 0.2$. The measurement and the prediction agree well each other in this fact. The maximum values at two locations reach 30% or more of the free stream velocity.

The pressure coefficients compare well away from the centerline at two stations, but show some discrepancies in the central region as shown in Fig. 35. This also might be due to the reason of the nonaxisymmetry explained earlier. The calculated pressure relaxation is much larger than that for the self-propelled case due to the larger velocity, and the pressure at $x/D_0 = 1.0$ is much less than the free stream reference pressure.

The turbulent kinetic energy is plotted in Fig. 36 for both the predicted and the measured. But it does make little sense to compare both due to the aforementioned reasons in the previous section. A comparison of the calculated data of the self-propelled and the over-thrusted can be made. From Figs. 25 and 36, the maximum values of the turbulent kinetic energy for the latter are increased by about 30% to 40% over the former at two stations and the peak point is slightly shifted into the central region.

The boundary layer profiles for the tangential velocity and turbulent kinetic energy predicted at five different locations on the body surface are presented in Figs. 37 and 38. The notation $RW(=r-r_w)$ denotes the normal distance from the body surface at each axial location. The boundary layer growth is shown well, and its thickness at $x/D_0=-0.2$ is about twice the one at the inlet plane, $x/D_0=-1.8$. However, the boundary layer growth is the smallest in the case of the over-thrusted and the largest in the case of no propeller. This can be explained by a favorable pressure gradient upstream of the propeller induced by the propeller motion. At station $x/D_0=-0.2$ it is clearly seen that the flow is pulled forward around $r/D_0=0.4$. The development of the turbulent kinetic energy shows the similar shape as the one for the self-propelled case. But the level is a little enhanced. The convex geometry makes the point of the peak turbulent kinetic energy move away from the body surface.

The skin friction coefficient on the the surface is shown in Fig. 39. It is depicted 10% to 30% larger than that for the self-propelled case. The skin friction coefficient at the propeller location is reduced to about 1/3 of that at the inlet plane.

The pressure contour plot in Fig. 40 describes clearly the abrupt jump across the propeller and the relaxation centered between 1 and 2 body diameters downstream of the

propeller. The contours show the same characteristics as the ones for the self-propelled case. The values in the legend represent the nondimensinalized pressure which is twice the pressure coefficient as explained earlier.

The predicted wake downstream of the propeller are illustrated in Figs. 41 and 42 The accelerated flow around $r/D_0 = 0.4$ keeps its momentum, while the wake in the central region coming off from the body tail continuously gains momentum and expands laterally. The turbulent kinetic energy also transports radially but the maximum value of it gradually reduces. The overall trend is very similar to the case of the self-propelled.

The variations of the three velocity components and pressure along the streamwise direction at $r/R_p = 0.8$ where the maximum thrust is generated are displayed in Figs. 43 through 46 for both cases. Note that at the inflow boundary the radial distance from the body surface($r_w/D_0 = 0.388$) to this line is very short. In Fig. 43, one clearly sees the strong streamline acceleration of the flow between upstream and downstream of the propeller. The accelerated flow at $r/R_p = 0.8$ does not lose speed even after 4 body diameters downstream of the propeller. The radial velocity profiles are shown in Fig. 44. If there were no solid boundary, the radial velocity would make a sharp V-letter type profile across the propeller[81,82]. Generally, the propeller effect on the radial velocity is confined in a small region upstream and downstream of the propeller. The strong streamline contraction is demonstrated well in the figure. Far upstream of the propeller, the radial component of velocity adjusts itself to satisfy the continuity along the convex surface in the proximity. The radial velocity is reduced along the streamline downstream.

Fig. 45 shows that the upstream influence of the propeller on the swirl velocity is negligible compared with the downstream influence as depicted by the inviscid vortex

theory[127,128]. The high rotational speed does not slow down until 4 body diameters downstream of the propeller. The small wiggles upstream of the propeller are typical phenomena when the Galerkin formulation is applied to the flow problems with a sudden change.

The streamline variation of the pressure coefficients along $r/R_p = 0.8$, where the maximum thrust occurs, is well described in Fig. 46. A large drop right in front of the propeller and discontinuous sudden jump is typical for the actuator disk theory. Downstream of the propeller the pressure relaxation follows.

5.4 Ducted Propeller

5.4.1 Solution Informations

This simulation is aimed wholly at the qualitative comparison of the predicted wake fields downstream of ducted and nonducted propellers at a self-propelled condition. For this purpose, the axial momentum increase past the propulsive system and the global torque due to the propeller in action should remain same. The characteristics of the ducted propeller were mentioned in detail in Chapter 4.

The computational domain is exactly the same as the one for the nonducted propeller case. The inflow boundary is located at 1.804 body diameters upstream of the propeller. The outflow plane stands at 4 body diameters downstream of the propeller, while the free stream boundary stretches out to 1.2 body diameters, as shown in Fig. 47.

The boundary conditions are described in the same figure. Briefly, at the inlet plane the measured boundary layer values were used, and no slip conditions on the slender body and duct surfaces and the traction-free and flux-free boundary conditions at the open ends were employed. And also along the axisymmetric line the radial velocity was constrained to zero. See Fig. 47.

The computed result for the skin friction coefficient at the nonducted self-propelled condition was used for the wall treatment, assuming that the presence of the duct does not affect the boundary layer profile. The boundary layer profile around the duct is totally unknown; the boundary layer thicknesses on both sides of the duct were assumed initially. After several iterations in the solution process, the boundary layer profiles could be obtained and the skin friction coefficients were updated. After two repetitions of the update of the coefficients, they did not change appreciably.

The effective wall treatment for the $k-\varepsilon$ model needs many points near wall. The presence of the three solid surfaces, the central slender body and two sides of the duct, required many nodal points near the surfaces and made the global system of equations very large. The mesh was generated in such a way that the number of nodal points was kept as small as possible while many points to treat the wall influence effectively were put near the walls. The selected mesh had 4,370 elements and 4,512 nodal points, 47 nodes radially and 96 nodes axially. The first point from the body was well inside the sublayer. To account for the boundary layer growth, the mesh near the body became thicker in the streamline direction. Linear isotropic elements were used and the penalty function formulation with the consistent integration method for a pressure recovery was employed. Each node has 5 unknowns and the total number of unknowns after the reduction for boundary conditions is 21,897.

The equations of motion were nondimensionalized with respect to D, U_0, and ρ_0. The initial guess for the self-propelled case was provided by the Stokes' flow solution for the velocity field and constant values of 0.001 for both k and ε. The nonlinear system of equations was solved by the successive substitution with underrelaxation, the value of which was fixed at 0.5 for the better convergence rate. The computing time for each iteration was 176 seconds on the IBM 3091 vector compiler at an optimization level 3, and 41 iterations was required for the L_2 –norm of the relative error of solution vector with respect to Stokes' solution to reach no greater than 10^{-4}.

5.4.2 Analysis for Self-Propelled Case

Since the drag and the duct interaction with other components of the propulsive system were not known a priori, the global thrust of the propeller alone for the self-propelled condition was obtained after a couple of sample runs with different levels of thrust. The global thrust of the propeller alone was obtained as 24 % larger than the thrust of the nonducted propeller to cancel the increased drag due to the duct. The large increase in the thrust is, as mentioned earlier, due to the fact that the combination of the selected duct, propeller, and slender body is not optimal.

The predicted mass flow rates and momentum fluxes through the free stream boundary of a circular cross section of radius of $1.2D_0$ for four cases of the non-propelled(stern region flow of a slender body), and the self-propelled, over-thrusted, and ducted propeller were presented in Fig. 48. Around the axial location of the duct, the mass entrainment from the free stream predicted for the ducted propeller is slightly less than that for the nonducted propeller at the same self-propelled condition. The

increase of momentum flux across the propeller plane of the ducted propeller was predicted larger than that of the nonducted propeller. Since the momentum changes between far upstream and far downstream for both propellers were shown same, the condition of the same net thrust was verified.

The boundary layer profiles of the axial velocity and the turbulent kinetic energy on the slender body are shown in Figs. 49 and 50. They do not show a substantial difference up to $-0.6D_0$ from the profiles of the nonducted self-propelled case. At the station of $-0.2D_0$ the axial velocity and the turbulent kinetic energy show stiff gradients due to the presence of the duct. The skin friction coefficient of the ducted propeller is slightly larger than that of the nonducted propeller as shown in Fig. 51. The larger skin friction is obvious inside the duct because the boundary layer growth is now damped due to the presence of the duct, which can be seen in a comparison of Figs. 26 and 49.

Fig. 52 shows the boundary layer profiles on the inside and outside surfaces of the duct. The boundary layers on both sides grow rapidly due to adverse pressure gradients. Upstream and downstream wakes due to the presence of the duct are also seen in the figure. Fig. 53 represents the skin friction coefficients on the both sides of the duct. The boundary layer growths are well indicated in the figure. The velocity vectors around the duct were plotted in Fig. 54, where wake and its development downstream of the duct was displayed well.

In the pressure contour plot around the duct of Fig. 55, the pressure jump past the propeller is clearly seen. In the central region, the pressure relaxation can be seen, but downstream of the duct there follows a slight increase in pressure in a finite region, which seems to be due to a momentum deficit. The contour values shown in the legend

are of the nondimensionalized value, $(P - P_{ref})/\rho_0 U_0^2$, which is one half of the pressure coefficient.

The predicted axial velocity and the turbulent kinetic energy profiles downstream of the propeller, ducted and nonducted, at the self-propelled condition, were compared in Figs. 56 and 57. The velocity deficit and recovery is well described. The ducted propeller has larger momentum in the central region, but smaller in the outer region than the momentum of the nonducted propeller, ending up with an equal magnitude of momentum. The wake downstream of the duct generates high level of turbulence as can be seen in Fig. 57. The turbulence gradually diminishes and spreads laterally.

The predictions for the three velocity components and the pressure coefficient along 80% of the propeller radius, around where the maximum thrust occurs, were shown in Figs. 58 through 61. Up to two propeller diameters downstream of the ducted propeller, the axial velocity is larger than that of the nonducted propeller. Far downstream, the axial velocity is diminished, because the region is in the wake caused by the duct. The stronger streamline constraction and upstream influence on the radial velocity of the ducted propeller is seen in Fig. 59. In Fig. 60, the same shape of the swirl velocity as the axial velocity is shown; since the ducted propeller generates larger angular momentum towards the blade tip than the nonducted propeller, the magnitude of the swirl velocity around $r/R_p = 0.8$ for the ducted propeller is larger than that for the nonducted propeller. The swirl velocity is reduced in the wake region downstream of the duct. The upstream influence on the swirl velocity is negligible for both cases. The predicted pressure coefficient along the same axial line were compared for the ducted and nonducted cases in Fig. 61. The ducted propeller generates the larger pressure change across the propeller plane.

6. CONCLUSIONS AND RECOMMENDATIONS

This work has successfully applied the Navier-Stokes equations and the two-equation turbulence model with the low Reynolds number wall modifications to four flow problems. The result demonstrated the applicability of the finite element method to the two-equation turbulence model for solving complex turbulent shear flows. The results can be summarized as:

1. The predicted reattachment distance was in a good agreement with measurements and other predictions.

2. The predictions of the mean flow field were in an excellent agreement with the measurement for the stern region flow of an axisymmetric slender body. The predicted turbulent kinetic energy was about 20% larger than the measured, which is a big improvement over the similar attempt[41].

3. The predictions for the nonducted propeller problem at two rotational speeds resulted in a very good agreement with the experiment for the mean flow variables. The improvement in the swirl velocity is remarkable compared to the similar analysis[42].

4. The numerical simulations showed that the propeller exerted a strong upstream influence on the axial, radial, and pressure field. The upstream influence of the propeller on the swirl was negligible.

5. The ducted propeller produced larger momentum increase across the propeller plane than the nonducted propeller. Also, the ducted propeller had larger concentrated momentum in the central region and smaller momentum in the wake region behind the duct, summing up the same magnitude of total momentum.

6. A propeller in action generated turbulence, but it was confined in the central region. The presence of a duct generated a large amount of turbulence, which transported axially and radially.

7. The two-equation turbulence model with the proper wall treatment showed a great feasibility for solving complex flows with separation, steep pressure gradient, and swirl.

8. Solving up to wall, using the two-equation model with the low Reynolds number wall modification, not only enhances the quality of the solution, but also makes easier the implementation of the boundary conditions. There is no need for the special treatment for the slip condition as done in the wall function method, which

is problem-dependent and sometimes very difficult to specify for complex flows. In this sence the wall treated two-equation model is very versatile and robust.

9. For the ducted propeller the combination of the duct geometry, the radial distribution of the thrust and torque, and the aft body was not optimal. More realistic treatment of them is suggested.

10. The predicted turbulence generated by the nonducted propeller at the self-propelled condition agreeed well in the central region with the measurements. However, away from the axisymmetric line, the predicted value could not be compared with measurements, which included not only turbulence, but also pulsating large-scale motion with high frequency.

11. An appropriate method to measure or to make data reduction for the velocity correlations downstream of the propeller should be made.

Appendix A. Derivation of Global Stiffness Matrix Coefficients

The manipulation required to transform the governing partial differential equations in cylindrical coordinates into a discrete system is detailed here. Both the mixed and the penalty formulations are considered. For convenience, the composite form of the high- and low-Reynolds-number versions of the nondimensionalized equations to be discretized is recalled:

$$U_x \frac{\partial U_x}{\partial x} + U_r \frac{\partial U_x}{\partial r} = \frac{\partial}{\partial x}(\sigma_{xx}) + \frac{1}{r}\frac{\partial}{\partial r}(r\sigma_{xr}) + f_x \qquad (A1)$$

$$U_x \frac{\partial U_r}{\partial x} + U_r \frac{\partial U_r}{\partial r} - \frac{U_\theta^2}{r} = \frac{\partial}{\partial x}(\sigma_{xr}) + \frac{1}{r}\frac{\partial}{\partial r}(r\sigma_{rr}) - \frac{\sigma_{\theta\theta}}{r} + f_r \qquad (A2)$$

$$U_x \frac{\partial U_\theta}{\partial x} + U_r \frac{\partial U_\theta}{\partial r} + \frac{U_r U_\theta}{r} = \frac{\partial}{\partial x}(\sigma_{x\theta}) + \frac{1}{r^2}\frac{\partial}{\partial r}(r^2\sigma_{r\theta}) + f_\theta \qquad (A3)$$

$$\frac{\partial U_x}{\partial x} + \frac{1}{r}\frac{\partial}{\partial r}(rU_r) = 0 \qquad (A4)$$

$$U_x \frac{\partial k}{\partial x} + U_r \frac{\partial k}{\partial r} = \frac{\partial}{\partial x}\left[(\nu + \frac{\nu_t}{\sigma_k}) \frac{\partial k}{\partial x} \right] + \frac{1}{r} \frac{\partial}{\partial r}\left[r(\nu + \frac{\nu_t}{\sigma_k}) \frac{\partial k}{\partial r} \right]$$

$$+ P_k - 2\left(\frac{\partial \sqrt{k}}{\partial r} \right)^2 - \tilde{\varepsilon} \qquad (A5)$$

$$U_x \frac{\partial \tilde{\varepsilon}}{\partial x} + U_r \frac{\partial \tilde{\varepsilon}}{\partial r} = \frac{\partial}{\partial x}\left[(\nu + \frac{\nu_t}{\sigma_\varepsilon}) \frac{\partial \tilde{\varepsilon}}{\partial x} \right] + \frac{1}{r} \frac{\partial}{\partial r}\left[r(\nu + \frac{\nu_t}{\sigma_\varepsilon}) \frac{\partial \tilde{\varepsilon}}{\partial r} \right]$$

$$+ \frac{\tilde{\varepsilon}}{k}(c_{\varepsilon 1} f_1 P_k - c_{\varepsilon 2} f_2 \tilde{\varepsilon}) \qquad (A6)$$

$$+ 2\nu\nu_t \left\{ \frac{\partial}{\partial r}\left[\left(\frac{\partial U_x}{\partial r} \right)^2 + \left(r \frac{\partial (U_\theta / r)}{\partial r} \right)^2 \right]^{1/2} \right\}^2$$

where the nondimensionalization process in Chapter 3 is utilized and the asterisks are omitted for brevity. The diffusion terms in the momentum equations are expressed in terms of the divergence of stresses, which results in natural boundary conditions when the Galerkin finite element procedure is used. The stress components are defined by:

$$\sigma_{xx} = -P + 2\mu_e \frac{\partial U_x}{\partial x} \qquad \sigma_{xr} = \mu_e \left(\frac{\partial U_x}{\partial r} + \frac{\partial U_r}{\partial x} \right)$$

$$\sigma_{rr} = -P + 2\mu_e \frac{\partial U_r}{\partial r} \qquad \sigma_{r\theta} = \mu_e r \frac{\partial}{\partial r}(\frac{U_\theta}{r}) \qquad (A7)$$

$$\sigma_{\theta\theta} = -P + 2\mu_e \frac{U_r}{r} \qquad \sigma_{x\theta} = \mu_e \frac{\partial U_\theta}{\partial x}$$

where the dimensionless effective viscosity μ_e is either μ or $\mu + \mu_t$ where appropriate. The production of turbulent kinetic energy P_k is written as:

$$P_k = 2\nu_t \left[\left(\frac{\partial U_x}{\partial x}\right)^2 + \left(\frac{\partial U_r}{\partial r}\right)^2 + \left(\frac{U_r}{r}\right)^2 \right] + \nu_t \left[\left(\frac{\partial U_x}{\partial r} + \frac{\partial U_r}{\partial x}\right)^2 + \left(r \frac{\partial}{\partial r}\left(\frac{U_\theta}{r}\right)\right)^2 + \left(\frac{\partial U_\theta}{\partial x}\right)^2 \right] \tag{A8}$$

The dimensionless Reynolds stresses are written as:

$$-\overline{u_i u_j} = \nu_t \left(\frac{\partial U_i}{\partial x_j} + \frac{\partial U_j}{\partial x_i}\right) - \frac{2}{3} k \delta_{ij} \tag{A9}$$

and the nondimensionalized eddy viscosity is

$$\nu_t = c_\mu f_\mu \frac{k^2}{\tilde{\varepsilon}} \tag{A10}$$

The boundary conditions are generally expressed as

$$U_i = \overline{U}_i \,,\; k = \overline{k} \,,\; \tilde{\varepsilon} = \overline{\varepsilon} \quad \text{on } S_1 \text{ (inlet plane and wall)}$$

$$U_r = 0 \,,\; t_x = t_\theta = \frac{\partial k}{\partial n} = \frac{\partial \tilde{\varepsilon}}{\partial n} = 0 \quad \text{on } S_2 \text{ (symmetry line)} \tag{A11}$$

$$t_x = t_r = t_\theta = \frac{\partial k}{\partial n} = \frac{\partial \tilde{\varepsilon}}{\partial n} = 0 \quad \text{on } S_3 \text{ (exit plane and far field)}$$

where the bar denotes specified values.

In the Galerkin formulation the dependent variables and their variations are approximated by the same interpolation functions as

$$
\begin{aligned}
U_i(x_j) &= \sum_{J=1}^{N} U_{iJ}\,\phi_J(x_j), \qquad \delta U_i(x_j) \sim \phi_I(x_j) \\
P(x_j) &= \sum_{J=1}^{N} P_J\,\psi_J(x_j), \qquad \delta P(x_j) \sim \psi_I(x_j) \\
k(x_j) &= \sum_{J=1}^{N} k_J\,\phi_J(x_j), \qquad \delta k(x_j) \sim \phi_I(x_j) \\
\tilde{\varepsilon}(x_j) &= \sum_{J=1}^{N} \tilde{\varepsilon}_J\,\phi_J(x_j), \qquad \delta\tilde{\varepsilon}(x_j) \sim \phi_I(x_j)
\end{aligned}
\tag{A12}
$$

By applying the Galerkin preocedure to equations (A1) - (A11), the following equations can be obtained;

x - momentum ;

$$
\begin{aligned}
&\left[\int_B \left(U_x\,\phi_I\,\frac{\partial\phi_J}{\partial x} + U_r\,\phi_I\,\frac{\partial\phi_J}{\partial r}\right)dB\right]U_{xJ} \\
&= -\left[\int_B \nu_e\left(2\,\frac{\partial\phi_I}{\partial x}\,\frac{\partial\phi_J}{\partial x} + \frac{\partial\phi_I}{\partial r}\,\frac{\partial\phi_J}{\partial r}\right)dB\right]U_{xJ} \\
&- \left[\int_B \nu_e\,\frac{\partial\phi_I}{\partial r}\,\frac{\partial\phi_J}{\partial x}\,dB\right]U_{rJ} \\
&+ \left[\int_B \frac{\partial\phi_I}{\partial x}\,\psi_J\,dB\right]P_J \\
&+ \int_B f_x\,\phi_I\,dB + \int_S \tilde{t}_x\,\phi_I\,dS
\end{aligned}
\tag{A13}
$$

r - momentum ;

$$
\begin{aligned}
&\left[\int_B \phi_I \left(U_x \frac{\partial \phi_J}{\partial x} + U_r \frac{\partial \phi_J}{\partial r}\right) dB\right] U_{rJ} \\
&- \left[\int_B \frac{U_\theta}{r} \phi_I \phi_J \, dB\right] U_{\theta J} \\
&= -\left[\int_B \nu_e \frac{\partial \phi_I}{\partial x} \frac{\partial \phi_J}{\partial r} \, dB\right] U_{xJ} \\
&- \left[\int_B \nu_e \left(\frac{\partial \phi_I}{\partial x} \frac{\partial \phi_J}{\partial x} + 2 \frac{\partial \phi_I}{\partial r} \frac{\partial \phi_J}{\partial r} + \frac{2}{r^2} \phi_I \phi_J\right) dB\right] U_{rJ} \\
&+ \left[\int_B \left(\frac{\partial \phi_I}{\partial r} + \frac{\phi_I}{r}\right) \psi_J \, dB\right] P_J \\
&+ \int_B f_r \phi_I \, dB + \int_S \bar{t}_r \phi_I \, dS
\end{aligned}
\tag{A14}
$$

θ - momentum ;

$$
\begin{aligned}
&\left[\int_B \phi_I \left(U_x \frac{\partial \phi_J}{\partial x} + U_r \frac{\partial \phi_J}{\partial r} + \frac{U_r}{r} \phi_J\right) dB\right] U_{\theta J} \\
&= -\left[\int_B \nu_e \left(\frac{\partial \phi_I}{\partial x} \frac{\partial \phi_J}{\partial x} + \frac{1}{r^2} \phi_I \phi_J\right) dB\right] U_{\theta J} \\
&+ \int_B f_\theta \phi_I \, dB + \int_S \bar{t}_\theta \phi_I \, dS
\end{aligned}
\tag{A15}
$$

continuity ;

$$
-\left[\int_B \psi_I \frac{\partial \phi_J}{\partial x} \, dB\right] U_{xJ} - \left[\int_B \psi_I \left(\frac{\partial \phi_J}{\partial r} + \frac{\phi_J}{r}\right) dB\right] U_{rJ} = 0 \tag{A16}
$$

turbulent kinetic energy ;

$$
\begin{aligned}
&\left[\int_B \phi_I\left(U_x\frac{\partial\phi_J}{\partial x}+U_r\frac{\partial\phi_J}{\partial r}\right)dB\right]k_J\\
&=\left\{\int_B v_t\left[2\frac{\partial U_x}{\partial x}\phi_I\frac{\partial\phi_J}{\partial x}+\left(\frac{\partial U_x}{\partial r}+\frac{\partial U_r}{\partial x}\right)\phi_I\frac{\partial\phi_J}{\partial r}\right]dB\right\}U_{xJ}\\
&+\left\{\int_B v_t\left[2\frac{\partial U_r}{\partial r}\phi_I\frac{\partial\phi_J}{\partial r}+\left(\frac{\partial U_x}{\partial r}+\frac{\partial U_r}{\partial x}\right)\phi_I\frac{\partial\phi_J}{\partial x}+\frac{U_r}{r^2}\phi_I\phi_J\right]dB\right\}U_{rJ}\\
&+\left\{\int_B v_t\left[\frac{\partial U_\theta}{\partial x}\phi_I\frac{\partial\phi_J}{\partial x}+\left(\frac{\partial U_\theta}{\partial r}-\frac{U_\theta}{r}\right)\phi_I\left(\frac{\partial\phi_J}{\partial r}-\frac{\phi_J}{r}\right)\right]dB\right\}U_{\theta J}\\
&-\left\{\int_B\left[\left(v+\frac{v_t}{\sigma_k}\right)\left(\frac{\partial\phi_I}{\partial x}\frac{\partial\phi_J}{\partial x}+\frac{\partial\phi_I}{\partial r}\frac{\partial\phi_J}{\partial r}\right)+\frac{v}{2k}\frac{\partial k}{\partial r}\phi_I\frac{\partial\phi_J}{\partial r}\right]dB\right\}k_J\\
&-\left[\int_B\phi_I\phi_J dB\right]\tilde{\varepsilon}_J+\int_S\left(v+\frac{v_t}{\sigma_k}\right)\phi_I\frac{\partial\bar{k}}{\partial n}\,dS
\end{aligned}
\tag{A17}
$$

rate of dissipation of turbulent kinetic energy ;

$$
\begin{aligned}
&\left[\int_B \phi_I\left(U_x\frac{\partial\phi_J}{\partial x}+U_r\frac{\partial\phi_J}{\partial r}\right)dB\right]\tilde{\varepsilon}_J \\
&=\left\{\int_B c_1'\,c_\mu'\,k\left[2\frac{\partial U_x}{\partial x}\phi_I\frac{\partial\phi_J}{\partial x}+\left(\frac{\partial U_x}{\partial r}+\frac{\partial U_r}{\partial x}\right)\phi_I\frac{\partial\phi_J}{\partial r}\right]dB\right\}U_{xJ} \\
&-\left[2\nu\int_B \nu_t\frac{\partial^2 U_x}{\partial r^2}\frac{\partial\phi_I}{\partial r}\frac{\partial\phi_J}{\partial r}\,dB\right]U_{xJ} \\
&+\left[\int_B c_1'c_\mu'k\left(2\frac{\partial U_r}{\partial r}\phi_I\frac{\partial\phi_J}{\partial r}+\left(\frac{\partial U_x}{\partial r}+\frac{\partial U_r}{\partial x}\right)\phi_I\frac{\partial\phi_J}{\partial x}+2\frac{U_r}{r^2}\phi_I\phi_J\right)dB\right]U_{rJ} \\
&+\left\{\int_B c_1'c_\mu'k\left[\frac{\partial U_\theta}{\partial x}\phi_I\frac{\partial\phi_J}{\partial x}+\left(\frac{\partial U_\theta}{\partial r}-\frac{U_\theta}{r}\right)\phi_I\left(\frac{\partial\phi_J}{\partial r}-\frac{\phi_J}{r}\right)\right]dB\right\}U_{\theta J} \\
&-\left[2\nu\int_B \nu_t\left(\frac{\partial^2 U_x}{\partial r^2}-\frac{1}{r}\frac{\partial U_\theta}{\partial r}+\frac{U_\theta}{r^2}\right)\frac{\partial\phi_I}{\partial r}\left(\frac{\partial\phi_J}{\partial r}-\frac{\phi_J}{r}\right)dB\right]U_{\theta J} \\
&-\left\{\int_B\left[(\nu+\frac{\nu_t}{\sigma_\varepsilon})\left(\frac{\partial\phi_I}{\partial x}\frac{\partial\phi_J}{\partial x}+\frac{\partial\phi_I}{\partial r}\frac{\partial\phi_J}{\partial r}\right)+c_2'\frac{\tilde{\varepsilon}}{k}\phi_I\phi_J\right]dB\right\}\tilde{\varepsilon}_J \\
&+\int_S(\nu+\frac{\nu_t}{\sigma_\varepsilon})\phi_I\frac{\partial\bar{\varepsilon}}{\partial n}\,dS
\end{aligned}
\qquad (A18)
$$

where $\tilde{\varepsilon}/k$ is replaced by $c'_\mu\,k/\nu_t$ for the generation term in Eq.(A.6). The new parameters ν_e, c_1', c_2', and c_μ' are defined as

$$
\begin{aligned}
\nu_e &= \nu+\nu_t && \text{for wall dominant region} \\
\nu_e &= \nu_t && \text{for fully turbulent region} \\
c_1' &= c_{\varepsilon 1}f_1 \\
c_2' &= c_{\varepsilon 2}f_2 \\
c_\mu' &= c_\mu f_\mu,
\end{aligned}
$$

f_1, f_2, and f_μ being the modification functions near wall expressed in Chapter 3. In deriving the above equations, the Green-Gauss theorem has been used to reduce the second-order diffusion terms in the momentum and turbulence transport equations and the penalty pressure terms to first-order terms plus surface integrals. The appearance of the surface integrals containing the applied surface stresses corresponds to the natural boundary conditions for the problem.

Once the form of the interpolation functions ϕ and ψ is specified, the integrals in the equations (A11)-(A16) may be evaluated to produce the required coefficient matrices. Combining all the equations into a single matrix equation produces a system of algebraic equations of the form

$$\begin{bmatrix} K_{11} & K_{12} & K_{13} & C_1 & 0 & 0 \\ K_{21} & K_{22} & K_{23} & C_2 & 0 & 0 \\ K_{31} & K_{32} & K_{33} & C_3 & 0 & 0 \\ -C_1^T & -C_2^T & -C_3^T & 0 & 0 & 0 \\ K_{41} & K_{42} & K_{43} & 0 & K_{44} & K_{45} \\ K_{51} & K_{52} & K_{53} & 0 & K_{54} & K_{55} \end{bmatrix} \begin{bmatrix} U_x \\ U_r \\ U_\theta \\ P \\ k \\ \tilde{\varepsilon} \end{bmatrix} = \begin{bmatrix} F_x \\ F_r \\ F_\theta \\ 0 \\ F_k \\ F_\varepsilon \end{bmatrix} \qquad (A19)$$

for the mixed formulation. The coefficient matrices are defined by

$$K_{11} = \int_B \left[U_x \phi_I \frac{\partial \phi_J}{\partial x} + U_r \phi_I \frac{\partial \phi_J}{\partial r} + \nu_e Re_D \left(2 \frac{\partial \phi_I}{\partial x} \frac{\partial \phi_J}{\partial x} + \frac{\partial \phi_I}{\partial r} \frac{\partial \phi_J}{\partial r} \right) \right] dB \qquad (A20)$$

$$K_{12} = \int_B \nu_e \frac{\partial \phi_I}{\partial r} \frac{\partial \phi_J}{\partial x} dB \qquad (A21)$$

$$K_{13} = 0 \qquad (A22)$$

$$K_{21} = \int_B v_e \frac{\partial \phi_I}{\partial x} \frac{\partial \phi_J}{\partial r} \, dB \tag{A23}$$

$$\begin{aligned} K_{22} = & \int_B \left[U_x \phi_I \frac{\partial \phi_J}{\partial x} + U_r \phi_I \frac{\partial \phi_J}{\partial r} \right] dB \\ & + \int_B v_e \left(\frac{\partial \phi_I}{\partial x} \frac{\partial \phi_J}{\partial x} + 2 \frac{\partial \phi_I}{\partial r} \frac{\partial \phi_J}{\partial r} + \frac{2}{r^2} \phi_I \phi_J \right) dB \end{aligned} \tag{A24}$$

$$K_{23} = - \int_B \frac{U_\theta}{r} \phi_I \phi_J \, dB \tag{A25}$$

$$K_{31} = 0 \tag{A26}$$

$$K_{32} = 0 \tag{A27}$$

$$\begin{aligned} K_{33} = & \int_B \left(U_x \phi_I \frac{\partial \phi_J}{\partial x} + U_r \phi_I \frac{\partial \phi_J}{\partial r} + \frac{U_r}{r} \phi_I \phi_J \right) dB \\ & + \int_B v_e \left(\frac{\partial \phi_I}{\partial x} \frac{\partial \phi_J}{\partial x} + \frac{\partial \phi_I}{\partial r} \frac{\partial \phi_J}{\partial r} + \frac{1}{r^2} \phi_I \phi_J \right) dB \end{aligned} \tag{A28}$$

$$C_1 = - \int_B \frac{\partial \phi_I}{\partial x} \psi_J \, dB \tag{A29}$$

$$C_2 = - \int_B \left(\frac{\partial \phi_J}{\partial r} + \frac{\phi_J}{r} \right) \psi_I \, dB \tag{A30}$$

$$C_3 = 0 \tag{A31}$$

$$K_{41} = - \int_B v_t \left[2 \frac{\partial U_x}{\partial x} \phi_I \frac{\partial \phi_J}{\partial x} + \left(\frac{\partial U_x}{\partial r} + \frac{\partial U_r}{\partial x} \right) \phi_I \frac{\partial \phi_J}{\partial r} \right] dB \tag{A32}$$

$$K_{42} = - \int_B v_t \left[2 \frac{\partial U_r}{\partial r} \phi_I \frac{\partial \phi_J}{\partial r} + \left(\frac{\partial U_x}{\partial r} + \frac{\partial U_r}{\partial x} \right) \phi_I \frac{\partial \phi_J}{\partial x} + 2 \frac{U_r}{r^2} \phi_I \phi_J \right] dB \tag{A33}$$

$$K_{43} = -\int_B \nu_t \left[\frac{\partial U_\theta}{\partial x} \phi_I \frac{\partial \phi_J}{\partial x} + \left(\frac{\partial U_\theta}{\partial r} - \frac{U_\theta}{r} \right) \phi_I \left(\frac{\partial \phi_J}{\partial r} - \frac{\phi_J}{r} \right) \right] dB \quad (A34)$$

$$K_{44} = \int_B \left(U_x \phi_I \frac{\partial \phi_J}{\partial x} + U_r \phi_I \frac{\partial \phi_J}{\partial r} \right) dB + \int_B \left[(\nu + \frac{\nu_t}{\sigma_\varepsilon}) \left(\frac{\partial \phi_I}{\partial x} \frac{\partial \phi_J}{\partial x} + \frac{\partial \phi_I}{\partial r} \frac{\partial \phi_J}{\partial r} \right) + \frac{\nu}{2k} \frac{\partial k}{\partial r} \phi_I \frac{\partial \phi_J}{\partial r} \right] dB \quad (A35)$$

$$K_{45} = \int_B \phi_I \phi_J \, dB \quad (A36)$$

$$K_{51} = -\int_B c_1' \, c_\mu' \, k \left[2 \frac{\partial U_x}{\partial x} \phi_I \frac{\partial \phi_J}{\partial x} + \left(\frac{\partial U_x}{\partial r} + \frac{\partial U_r}{\partial x} \right) \phi_I \frac{\partial \phi_J}{\partial r} \right] dB - 2\nu \int_B \nu_t \frac{\partial^2 U_x}{\partial r^2} \frac{\partial \phi_I}{\partial r} \frac{\partial \phi_J}{\partial r} \, dB \quad (A37)$$

$$K_{52} = -\int_B c_1' \, c_\mu' \, k \left[2 \frac{\partial U_r}{\partial r} \phi_I \frac{\partial \phi_J}{\partial r} + \left(\frac{\partial U_x}{\partial r} + \frac{\partial U_r}{\partial x} \right) \phi_I \frac{\partial \phi_J}{\partial x} + 2 \frac{U_r}{r^2} \phi_I \phi_J \right] dB \quad (A38)$$

$$K_{53} = -\int_B c_1' \, c_\mu' \, k \left[\frac{\partial U_\theta}{\partial x} \phi_I \frac{\partial \phi_J}{\partial x} - \left(\frac{\partial U_\theta}{\partial r} - \frac{U_\theta}{r} \right) \frac{\partial \phi_I}{\partial r} \phi_J \right] dB - 2\nu \int_B \nu_t \left[\left(\frac{\partial^2 U_\theta}{\partial r^2} - \frac{1}{r} \frac{\partial U_\theta}{\partial r} + \frac{U_\theta}{r^2} \right) \frac{\partial \phi_I}{\partial r} \left(\frac{\partial \phi_J}{\partial r} - \frac{\phi_J}{r} \right) \right] dB \quad (A39)$$

$$K_{54} = 0 \quad (A40)$$

$$K_{55} = \int_B \left(U_x \phi_I \frac{\partial \phi_J}{\partial r} + U_r \phi_I \frac{\partial \phi_J}{\partial r} \right) dB + \int_B (\nu + \frac{\nu_t}{\sigma_\varepsilon}) \left(\frac{\partial \phi_I}{\partial x} \frac{\partial \phi_J}{\partial x} + \frac{\partial \phi_I}{\partial r} \frac{\partial \phi_J}{\partial r} \right) dB + \int_B c_2' \frac{\tilde{\varepsilon}}{k} \phi_I \phi_J \, dB \quad (A41)$$

$$F_x = \int_B f_x \phi_I \, dB + \int_S \bar{t}_x \phi_I \, dS \tag{A42}$$

$$F_r = \int_B f_r \phi_I \, dB + \int_S \bar{t}_r \phi_I \, dS \tag{A43}$$

$$F_\theta = \int_B f_\theta \phi_I \, dB + \int_S \bar{t}_\theta \phi_I \, dS \tag{A44}$$

$$F_k = \int_S (\nu + \frac{\nu_t}{\sigma_k}) \frac{\partial \bar{k}}{\partial n} \phi_I \, dS \tag{A45}$$

$$F_\varepsilon = \int_S (\nu + \frac{\nu_t}{\sigma_\varepsilon}) \frac{\partial \bar{\varepsilon}}{\partial n} \phi_I \, dS \tag{A46}$$

When the penalty formulation is applied, the row and column corresponding to the pressure unknown P are deleted and either K^{PR} or K^{PC} is added to the left hand side of the equation. The resultant matrix equation is written as

$$\begin{bmatrix} K_{11}+\lambda K_{11}^P & K_{12}+\lambda K_{12}^P & K_{13}+\lambda K_{13}^P & 0 & 0 \\ K_{21}+\lambda K_{21}^P & K_{22}+\lambda K_{22}^P & K_{23}+\lambda K_{23}^P & 0 & 0 \\ K_{31}+\lambda K_{31}^P & K_{32}+\lambda K_{32}^P & K_{33}+\lambda K_{33}^P & 0 & 0 \\ K_{41} & K_{42} & K_{43} & K_{44} & K_{45} \\ K_{51} & K_{52} & K_{53} & K_{54} & K_{55} \end{bmatrix} \begin{bmatrix} U_x \\ U_r \\ U_\theta \\ k \\ \tilde{\varepsilon} \end{bmatrix} = \begin{bmatrix} F_x \\ F_r \\ F_\theta \\ F_k \\ F_\varepsilon \end{bmatrix} \tag{A47}$$

where the new coefficients of the matrix, K_{ij}^P, are given either by

$$K_{11}^{PR} = -\int_B \frac{\partial \phi_I}{\partial x} \frac{\partial \phi_J}{\partial x} \, dB \tag{A48}$$

$$K_{12}^{PR} = -\int_B \frac{\partial \phi_I}{\partial x}\left(\frac{\partial \phi_J}{\partial r} + \frac{\phi_J}{r}\right) dB \qquad (A49)$$

$$K_{21}^{PR} = [K_{12}^{PR}]^T \qquad (A50)$$

$$K_{22}^{PR} = \int_B \left(\frac{\partial \phi_I}{\partial r} + \frac{\phi_I}{r}\right)\left(\frac{\partial \phi_J}{\partial r} + \frac{\phi_J}{r}\right) dB \qquad (A51)$$

$$K_{13}^{PR} = K_{31}^{PR} = K_{23}^{PR} = K_{32}^{PR} = K_{33}^{PR} = 0 \qquad (A52)$$

when the reduced integration is applied, or by

$$K_{ij}^{PC} = C_i M^{-1} C_j^T \qquad (A53)$$

when the consistent integration is applied. The pressure mass matrix, M is defined as in Eq.(3.42);

$$M = \int_B \psi_I \psi_J dB \qquad (A54)$$

and C_i is defined at Eqs.(A29)-(A31).

References

1. Huang, T. T., Wang, H. T., Santelli, N., and Groves, N. C., "Propeller/Stern/Boundary Layer Interaction on Axisymmetric Bodies: Theory and Experiment", *DTNSRDC, Ship Performance Dept.*, Rpt. 76-0113, December 1976.

2. Huang, T. T. and Cox, B. D., "Interaction of Afterbody Boundary Layer and Propeller", *Symposium on Hydrodynamics of Ship and Offshore Propulsion Systems*, March 20-25, 1977.

3. Huang, T. T. and Groves, N. C., "Effective Wake: Theory and Experiment", *Proc. 13th Symposium on Naval Hydrodynamics*, Tokyo, 1980.

4. Küchemann, D. and Weber, J., *Aerodynamics of Propulsion*, Chapter 6 - The Ducted Propeller, McGraw-Hill, 1953.

5. Van Manen, J. D. and Oosterveld, M. W. C., "Analysis of Ducted Propeller Design", *SNAME Transaction*, Vol.74, 1966, pp.522-562.

6. Glover, E. J. and Ryan, P. G., "A Comparison of the Theoretical and Experimental Performance of a Ducted Propeller System", *Proc. of the Symposium on Ducted Propeller*, Paper No.5, 1973

7. Ryan, P. G. and Glover, E. J., "A Ducted Propeller Design Method : A New Approach Using Surface Vorticity Distribution Techniques and Lifting Line Theory", *Trans. RINA*, Vol.114, 1972.

8. Morgan, W. B. and Wrench, J. W. Jr., "Some Computational Aspects of Propeller Design", *Methods in Computational Physics*, Vol.4, 1965, pp.301-331.

9. Gibson, I. S. and Lewis, R. I., "Ducted Propeller Analysis by Surface Vorticity and Actuator Disc Theory", *Proc. of the Symposium on Ducted Propeller*, Paper No.1, 1973

10. Hough, G. R. and Ordway, D. E., "The Generalized Actuator Disc", *Developmens in Theoretical and Applied Mechanics*, Vol.2, Pergamon Press, 1965, pp.317-336.

11. Oden, J. T. and Reddy, J. N., *Mathematical Theory of Finite Elements*, John Wiley and Sons, New York, 1976, pp.323-326.

12. Engelman, M. S., "FIDAP(A Fluid Dynamics Analysis Program)", *Advanced Engineering Software*, Vol.4, 1982.

13. Back, L. H. and Roschke, E. J., "Shear-Layer Flow Regimes and Wake Instabilities and Reattachment Lengths Downstream of an Abrupt Circular Channel Expansion", *J. of Applied Mechanics*, September 1972, pp.59-75.

14. Moon, L. F. and Rudinger, G., "Velocity Distribution in an Abruptly Expanding Circular Duct", *J. of Fluids Engineering*, March 1977, pp.226-230.

15. Krall, K. M. and Sparrow, E. M., "Turbulent Heat Transfer in the Separated, Reattachted and Reveloped Region of a Circular Tube", *J. of Heat Transfer*, Trans. ASME, Vol.88c, 1966, pp.131-136.

16. Runchal, A. K., "Mass Transfer Investigation in Turbulent Flow Downstream of Sudden Enlargement of a Circular Pipe for Very High Schmidt Numbers", *Int'l J. of Heat and Mass Transfer*, Vol.14, 1971, pp.781-791.

17. Kline, S. J., Morkovin, M. V., Sovran, G., and Cockrell, D. J. (editors), "Computation of Turbulent Boundary Layers", *Proc. AFOSR-IFP Stanford Conference*, Mech. Engr. Dept., Stanford Univ., 1968.

18. Smith, R. M., "On the Finite-Element Solution of Turbulent Flow Using the $k-\varepsilon$ Model", *CEGB Report*, TPRD/B/0161/N82, 1982.

19. Smith, R. M., "A Practical Method of Two-Equation Turbulence Modeling Using Finite Element", *CEGB Report*, TPRD/B/0182/N82, 1982.

20. Chieng, C. C. and Launder, B. E., "On the Calculation of Turbulent Heat Transfer Downstream from an Abrupt Pipe Expansion", *Numerical Heat Transfer*, Vol.3, 1980, pp.189-207.

21. Amano, R. S., "A Study of Turbulent Flow Downstream of an Abrupt Pipe Expansion", *AIAA J.*, Vol.21, 1985, pp.1400-1405.

22. Amano, R. S. "Development of a Turbulent Near-Wall Model and Its Application to Separated and Reattached Flows", *Numerical Heat Transfer*, Vol.7, 1984, pp.59-75.

23. Amano, R. S. and Goel, P., "A Numerical Study of a Separating and Reattaching Flow by Using Reynolds-Stress Turbulence Closure", *Numerical Heat Transfer*, Vol.7, 1984, pp.343-357.

24. Launder, B. E., Reece, G. J., and Rodi, W., "Progress in the Development of a Reynolds-Stress Turbulence Closure", *J. of Fluid Mechanics*, Vol.68, 1975, pp.537-566.

25. Bradshaw, P. and Wong, F. Y. F., "The Reattachment and Relaxation of a Turbulent Shear Layer", *J. of Fluid Mechanics*, Vol.52, 1972, pp.113-135.

26. Chandrsuda, C. and Bradshaw, P. "Turbulence Structure of a Reattaching Mixing Layer", *J. of Fluid Mechanics*, Vol.110, 1981, pp.171-194.

27. Kuehn, D. M., "Some Effects of Adverse Pressure Gradient on the Incompressible Reattaching Flow over a Rearward-Facing Step", *AIAA J.*, Vol. 18, pp.343-344, 1980.

28. Sindir, M. M., "Effects of Expansion Ratio on the Calculation of Parallel-Walled Backward Facing Step Flows : Comparison of Four Models of Turbulence", *ASME Paper*, 83-FE-10, 1983.

29. Westphal, R. V. and Johnston, J. P., "Effect of Initial Conditions on Turbulent Reattachment Downstream of a Backward-Facing Step", *AIAA J.*, Vol.22, 1984, pp.1727-1732.

30. Driver, D. M. and Seegmiller, H. L., "Features of a Reattaching Turbulent Shear Layer in Divergent Channel Flow", *AIAA J.*, Vol.23, No.2, 1985, pp.163-171.

31. Gosman, A. D., Khalil, E. E., and Whitelaw, J. H., "The Calculation of Two-Dimensional Turbulent Recirculating Flows", *Symposium on Turbulent Shear Flow*, Vol.1, University Park, Pennsylvania, April 18-20, 1977.

32. Amano, R. S. and Goel, P., "Computation of Turbulent Flow beyond Backward-Facing Steps Using Reynolds-Stress Closure", *AIAA J.*, Vol.23, No.9, 1985, pp.1356-1361.

33. Tayler, C., Thomas, C. E., and Morgan, K., "Analysis of Turbulent Flow with Separation Using the Finite Element Method", *Recent Advances in Numerical Methods in Fluids*, Vol.2, 1981.

34. Taylor, C., Thomas, C. E., and Morgan, K., "Finite Element Method and the Two Equation Model of Turbulence", *Numerical Methods in Laminar and Turbulent Flow*, Proceedings of the Second Int'l Conference, Venice, July 13-16, 1981.

35. Thomas, C. E., Morgan, K., and Taylor, C., "A Finite Element Analysis of Flow over a Backward Facing Step", *Computers and Fluids*, Vol.9, 1981, pp.265-278.

36. Eaton, J. K. and Johnston, J. P., "A Review of Research on Subsonic Turbulent Flow Reattachment", *AIAA J.*, Vol.19, No.9, 1981.

37. Simpson, R. L., "Two-Dimensional Turbulent Separated Flow", *AGARD*, No.287, Vol.1.

38. Simpson, R. L., "A Review of Two-Dimensional Turbulent Separated Flow Calculation Methods", IUTAM August 1986 Symposium on Boundary Layer Separation.

39. Nelson, N. E., Private Communication, 1972.

40. Breslin, J. P., Van Houten, R. J., Kerwin, J. E., Jonsson, C.-A., "Theoretical and Experimental Propeller-Induced Hull Pressures Arising from Intermittent Blade Cavitation, Loading, and Thickness", *Trans. SNAME*, Vol.90, 1982, pp.111-151.

41. Schetz, J. A. and Favin, S., "Numerical Solution for the Near Wake of a Body with Propeller", *J. of Hydronautics*, Vol.11, No.4, 1977.

42. Schetz, J. A. and Favin, S., "Numerical Solution of a Body-Propeller Combination Flow Including Swirl and Comparisons with Data", *J. of Hydronautics*, Vol.13, No.2, 1979.

43. Schetz, J. A. and Jakubowski, A. K., "Experimental Studies of the Turbulent Wake behind Self-Propelled Slender Bodies", *AIAA J.*, Vol.13, 1975, pp.1568-1575.

44. Stipa, L., "Experiments with Intubed Propellers", *NACA TM 655*, January 1932.

45. Kort, L., "Der Neue Düsenschrauben - Antrieb", *Werft-Reederei-Hafen*, Jahrgang 15, Heft 4, 1934.

46. Van Manen, J. D., "Recent Research on Propelers in Nozzles", *J. of Ship Research*, July 1957, pp.13-46.

47. Sacks, A. H. and Burnell, J. A., "Ducted Propellers - A Critical Review of the State of the Art", *Aeronautical Sciences*, Vol.3, 1963, pp.87-135.

48. Morgan, W. B. and Caster, E. B. "Comparison of Theory and Experiment on Ducted Propellers", *Seventh Symposium Naval Hydrodynamics*, August 1968, Rome, Italy, pp.1311-1349.

49. Weissinger, J. and Maass, D., "Theory of the Ducted Propeller - A Review", *Seventh Symposium on Naval Hydrodynamics*, August 1968, Rome, Italy, pp.1209-1264.

50. Morgan, W. B., "Theory of the Annular Airfoil and Ducted Propeller", *Fourth Symposium on Naval Hydrodynamics*, ONR, ACR-73, 1962, pp.151-197.

51. Chaplin, H. R., "A Method of a Shrouded Impulse Disk in the Static Case with Application to Other Axisymmetric Potential Flow Problems", DTMB Report 1857, Jan. 1964.

52. Meyerhoff, L., "Discussion to Paper by Van Manen, J. D. and Oosterveld, M. W. C., Analysis of Ducted-Propeller Design", *Trans. SNAME*, Vol.74, 1966, pp.549-550.

53. Kerwin, J. E., Kinnas, S. A., Lee, J.-T., and Shih, W.-Z., "A Surface Panel Method for the Hydrodynamic Analysis of Ducted Propeller", SNAME Paper No.4, November 11-14,1987.

54. Bercovier, M. and Engelman, M., "A Finite Element for the Numerical Solution of Viscous Incompressible Flows", *J. of Computational Physics*, Vol.30, 1979, pp.181-201.

55. Brooks, A. N. and Hughes, T. J. R., "Streamline Upwind/Petrov-Galerkin Formulations for Convection Dominated Flows with Particular Emphasis on the Incompressible Navier-Stokes Equations", *Computer Methods in Applied Mechanics and Enginering*, Vol.32, 1982, pp.199-250.

56. Gartling, D. K. and Becker, E. B., "Finite Element Analysis of Viscous Incompressible Fluid Flow", *Computer Methods in Applied Mechanics and Engineering*, Vol.8, 1976, pp.51-60(Part 1) and pp.127-138(Part 2).

57. Gresho, P. M. and Lee, R. L., " On the Time-Dependent Solution of the Incompressible Navier-Stokes Equations in Two and Three Dimensions", *Recent Advances in Numerical Methods in Fluids*, Vol.1, 1980.

58. Gresho, P. M., Lee, R. L., and Upson, C. D., "A Modified Finite Element Method for Solving the Time-Dependent, Incompressible Navier-Stokes Equations", *Int'l J. for Numerical Methods in Fluids*, Part 1:Theory, pp.557-598, Part 2:Applications, pp.619-640 , 1984.

59. Hughes, T. J. R., Liu, W. K., and Brooks, A., "Finite Element Analysis of Incompressible Viscous Flows by the Penalty Function Formualtion", *J. of Computational Physics*, Vol.30, 1979, pp.1-60.

60. Reddy, J. N., "Penalty-Finite-Element Analysis of Three-Dimensional Navier-Stokes Equations", *Computer Methods in Applied Mechanics and Engineering*, Vol.35, 1982, pp.87-106.

61. Reddy, J. N., "On Penalty Function Methods in the Finite-Element Analysis of Flow Problems", *Int'l J. for Numerical Methods in Fluids*, Vol.2, 1982, pp.151-171.

62. Shen, S.-F., "Finite-Element Methods in Fluid Mechanics", *Annual Review of Fluid Mechanics*, Vol.9, 1977, pp.421-445.

63. Thomasset, F., *Implementation of Finite Element Methods for Navier-Stokes Equations*, Springer-Verlag, New York, 1981.

64. Carey, G. F. and Oden, J. T., *Finite Elements : A second Cource* , Vol.2, Prentice Hall, 1983.

65. Zienkiewicz, O. C., *The Finite Element Method*, Third edition, McGraw-Hill, 1977.

66. Reddy, J. N., *An Introduction to the Finite Element Method*, McGraw-Hill, 1984.

67. Tayler, C., Hughes, T. G., and Morgan, K., "A Numerical Analysis of Turbulent Flow in Pipes", *Computers and Fluids*, Vol.5, 1977, pp.191-204.

68. Tayler, C., Harper, J. J., Hughes, T. G., and Morgan, K., "An Analysis of Developing Turbulent Flow in a Circular Pipe by the Finite Element Method", *Turbulent Boundary Layers*, The Joint ASME-CSME Conference, Niagara Falls, NY, June 18-20, 1979.

69. Morgan, K., Hughes, T. G., Taylor, C., "A Numerical Model of Turbulent Shear Flow behind a Prolate Spheroid", *Applied Mathematical Modeling*, Vol.2, 1978.

70. Tayler, C., Hughes, T. G., and Morgan, K., "A Finite Element Model of One and Two Equation Models of Turbulent Flow", *Recent Advances in Numerical Methods in Fluids*, Vol.1, 1980.

71. Morgan, K., Hughes, T. G., and Taylor, C., "The Analysis of Turbulent Free-Shear, and Channel Flows by the Finite Element Method", *Computer Methods in Applied Mechanics and Engineering*, Vol.19, 1979, pp.117-125.

72. Baker, A. J., "Finite Element Analysis of Turbulent Flows", *Turbulent Boundary Layers*, The Joint ASME-CSME Conference, Niagara Falls, NY, June 18-20, 1979.

73. Ecer, A., Spyropoulos, J., and Maul, J. D., "A Three-Dimensioanl, Block-Structured Finite Element Grid Generation Scheme", *AIAA J.*, Vol.23, 1985, pp.1483-1490.

74. Baker, A. J. and Manhardt, P. D., "Numerical Prediction of Mean and Fluctuating Velocities for Jet-Flap Flows", *AIAA J.*, Vol.16, 1978.

75. Soliman, M. O. and Baker, A. J., "Accuracy and Convergence of a Finite Element Algorithm for Turbulent Boundary Layer Flow", *Computer Methods in Applied Mechanics and Engineering*, Vol.28, 1981, pp.81-102.

76. Baker, A. J., Yu, A. J., Orzechowski, J. A., and Gatski, T. B., "Prediction and Measurement of Incompressible Turbulent Aerodynamic Trailing Edge Flows", *AIAA J.*, Vol.20, 1982, pp.51-59.

77. Baker, A. J., "On Current Aspects of Finite Element Computational Fluid Mechanics for Turbulent Flows", *Computer Methods in Applied Mechanics and Engineering*, Vol.32, 1982, pp.261-282.

78. Baker, A. J. and Orzechowski, J. A., "A Continuity Constraint Finite Element Algorithm for Three-Dimensional Parabolic Flow Prediction", *Computers in Flow Prediction and Fluid Dynamics Experiments*, ASME Publication, 1981.

79. Hutton, A. G., "Progress in the Development of a Finite Element Wall Model for High Reynolds Number, Turbulent Flow", *Applied Mathematical Modelling*, Vol.3, 1979, pp.322-326.

80. Hutton, A. G. and Smith, R. M., "On the Finite Element Simulation of Incompressible Turbulent Flow in General Two-Dimensional Geometries" , *Numerical Methods in Laminar and Turbulent Flow*, Proceedings of the Second Int'l Conference, Venice, July 13-16, 1981.

81. Pelletier, D. H. and Schetz, J. A., "A Navier-Stokes Calculation of Three-Dimensional Turbulent Flow Near a Propeller in a Shear Flow" , *AIAA Paper*, 85-0365, 1985.

82. Pelletier, D. H. and Schetz, J. A., "Finite Element Navier-Stokes Calculation of Three-Dimensional Turbulent Flow Near a Propeller", *AIAA J.*, Vol.24, No.9, 1986.

83. Thomas, R. H., "Finite Element Solution of 3D Turbulent Navier-Stokes Equations for Propeller-Driven Slender Bodies", Ph. D. Thesis, Virginia Tech., 1987.

84. McCormick, B. W., *Aerodynamics, Aeronautics, and Flight Mechanics*, John Wiley and Sons, 1979.

85. Schamber, D. R. and Larock, B. E., "Computational Aspects of Modeling Turbulent Flows by Finite Elements", *Turbulent Boundary Layers*, The Joint ASME-CSME Conference, Niagara Falls, NY, June 18-20, 1979.

86. Hanjelic, K. and Launder, B. E., "A Reynolds Stress Model of Turbulence and Its Application to Thin Shear Flows", *J. of Fluid Mechanics*, Vol.52, 1972.

87. Gibson, M. M. and Launder, B. E., "On the Calculation of Horizontal, Turbulent, Free Shear Flows under Gravitational Influence", *J. of Heat Transfer*, Trans. ASME, 1976, pp.81-87.

88. Rodi, W., "Basic Equations for Turbulent Flow in Cartesian and Cylindrical Coordinates", Imperial College, Mechanical Engineering, Report BL/TN/A/36, 1970.

89. Schlichting, H., *Boundary Layer Theory*, Seventh ed., McGraw-Hill, 1979.

90. Cebeci, T. and Smith, A. M. O., *Analysis of Turbulent Boundary Layers*, John Wiley and Sons, 1974.

91. Launder, B. E. and Spalding, D. B., *Lectures in Mathematical Models in Turbulence*, Academic Press, 1972.

92. Rotta, J. C., "Turbulent Boundary Layers in Incompressible Flow", *Progress in Aeronautical Sciences*, Vol.2, 1962, pp.1-219.

93. Townsend, A. A., *The Structure of Turbulent Shear Flow*, Cambridge University Press, London, 2nd ed., 1976.

94. Bradshaw, P., "The Understanding and Prediction of Turbulent Flow", *Aeronautical Journal*, Vol.76, 1972, pp.403-418.

95. Mellor, G. L. and Herring, H. J., "A Survey of the Mean Turbulent Field Closure Models", *AIAA J.*, Vol.11, 1973, pp.590-599.

96. Reynolds, W. C., "Computation of Turbulent Flows", *Annual Review of Fluid Machanics*, Vol.8, 1976, pp.183-208.

97. Rodi, W., "Turbulence Models and Their Application in Hydraulics-A State of Art Review", *Int'l Association for Hydraulic Research*, Delft, The Netherlands, 1980.

98. Rodi, W., "Examples of Turbulence Models for Incompressible Flows", *AIAA J.*, Vol.20, 1982.

99. Marvin, J. A., "Turbulence Modeling for Compressible Aerodynamics", *AIAA J.*, Vol.21, No.7, 1983.

100. Lumley, J. L., "Turbulence Modelling", *J. of Applied Mechanics*, Vol.50, December 1983.

101. Rubesin, M. W., "Numerical Turbulence Modelling", *AGARD Lecture Series 86 on Computational Fluid Dynamics*, 1977, pp.3.1-3.37.

102. Lakshminarayana, B., "Turbulence Modeling for Complex Shear Flows", *AIAA J.*, Vol.24, No.12, 1986, pp.1900-1916.

103. Nallasamy, M., "Turbulence Models and Their Applications to the Prediction of Internal Flows : A Review", *Computers and Fluids*, Vol.15, No.2, 1987.

104. Launder, B. E., "Trubulence Transport Models for Numerical Computation of Complex Turbulent Flows", Von Karman Inst. for Fluid Dynamics, LS 1980-3, 1980.

105. Schetz, J. A., *Foundations of Boundary Layer Theory for Momentum, Heat, and Mass Transfer*, Prentice-Hall, Inc., 1984.

106. Prandtl, L., "Bericht über Untersuchungen zur Ausgebildeten Turbulenz", *ZAMM*, Bd.5, 1925, pp.136-139.

107. Boussinesq, J., "Theorie de L'ecoulement Tourbillant", *Mem. Pres. Acad. Sci.*, Paris, Vol.23, 1977, P46.

108. Von Karman, Th., "Mechanische Ähnlichkeit und Turbulenz", *Nachr. Ges. Wiss.*, Goettingen, Math.-Phys. Klasse, 1930, p.58, English Trans. "Mechanical Similitude and Turbulence", *NACA TM*, No.611, 1931.

109. Bradshaw, P., "The Analogy between Streamline Curvature and Bouyancy in Turbulent Shear Flow", *J. of Fluid Mechanics*, Vol.36, 1969, pp.177-191.

110. Bradshaw, P., "Effects of Streamline Curvature on Turbulent Flow" , *AGARDograph*, 169, 1973.

111. Rotta, J. C., "A Family of Turbulence Models for Three-Dimensional Boundary Layers", *Turbulent Shear Flows I*, editted by Durst, F., Launder, B. E., Schmidt, F. W., and Whitelaw, J. H., Springer-Verlag, 1979, pp.267-278.

112. Van den Verg, B., Humpreys, D. A., Krause, E., and Lindout, J. F., "Comparison of Three-Dimensional Turbulent Boundary Layer Calculations for Five Experiments", Eurovic Workshop, Wieweg, 1986.

113. Fernholz, H. H. and Krause, E., (eds.), *Three-Dimensional Boundary Layers*, Springer-Verlag, New York, 1982.

114. Kolmogorov, A. N., "Equations of Turbulent Motion of an Incompressible Fluid", 1942, English Translation : Imperial College, Dept. of Mech. Eng., Report ON/6, 1968.

115. Prandtl, L., "Über eine Neues Formelsystem für die Ausgebildete Turbulenz", *Nachr. Akad. Wiss.*, Goettingen, Math.-Phys. Klasse, 1945, pp.6-19.

116. Bradshaw, P., Ferriss, D. H., and Atwell, N. P., "Calculation of Boundary-Layer Development Using the Turbulent Energy Equation", *J. of Fluid Mechanics*, Vol.28, 1967, pp.593-616.

117. Hassid, S. and Poreh, M., "A Turbulent Energy Model for Flows with Drag Reduction", *J. of Fluids Engineering*, Vol.97, June 1975, pp.234-241.

118. Chou, P. Y., "On Velocity Correlations and the Solutions of the Equations of Turbulent Fluctuation", *Quarterly of Applied Mathematics*, Vol.3, 1945, pp.38-54.

119. Davidov, B. I., "On the Statistical Dynamics of an Incompressible Turbulent Fluid, *Dokl. AN SSSR*, 136, 1961.

120. Harlow, F. H. and Nakayama, P. I., 'Turbulence Transport Equations', *The Physics of Fluids*, Vol.10, 1967, pp.2323-2332.

121. Jones, W. P. and Launder, D. B., 'The Prediction of Laminarization with Two-Equation Model of Turbulence', *Int'l J. of Heat and Mass Transfer*, Vol.15, 1972.

122. Rotta, J. C., 'Statistical Theory of Nonhomogeneous Turbulence' , 1951, English Translation : Imperial College, Dept. of Mech. Eng., Report TWF/TN/38,39, 1968.

123. Rodi, W. and Spalding, D. B., 'A Two-Parameter Model of Turbulence and Its Application to Free Jets', *Wärme- und Stoffübertragung*, B.3, 1970.

124. Ng, K. H. and Spalding, D. B., 'Turbulence Model for Boundary Layers Near Walls', *The Physics of Fluids*, Vol.15, No.1, 1972.

125. Ng, K. H. and Spalding, D. B., 'Prediction of Two-Dimensional Boundary Layers on Smooth Walls with a Two-Equation Model of Turbulence' , *Int'l J. of Heat and Mass Transfer*, Vol.19, 1976.

126. Spalding, D. B., 'The k-w Model of Turbulence', Imperial College, Dept. of Mech. Eng., Report TM/TN/A/16, 1972.

127. Gibson, M. M. and Spalding, D. B., 'A Two-Equation Model of Turbulence Applied to the Prediction of Heat Transfer in Wall Boundary Layers', *J. of Heat Transfer*, Trans. ASME, Vol.15, 1972.

128. Saffman, P. G., 'A Model for Inhomogeneous Turbulent Flow', *Proceedings of the Royal Society of London*, Ser.A, Vol.317, 1970, pp.417-433.

129. Saffman, P. G. and Wilcox, D. C., 'Turbulence-Model Predictions for Turbulent Boundary Layers', *AIAA J.*, Vol.12, No.4, 1974, pp.541-546.

130. Wilcox, D. C. and Traci, R. M., 'A Complete Model of Turbulence ", *AIAA Paper 76-351*, San Diego, California, 1976.

131. Launder, B. E. and Spalding, D. B., 'The Numerical Computation of Turbulent Flows', *Computer Methods in Applied Mechanics and Engineering*, Vol.3, 1974.

132. Singhal, A. K. and Spalding, D. B., 'Prediction of Two-Dimensional Boundary Layers with the Aid of the $k-\varepsilon$ Model of Turbulence', *Computer Methods in Applied Mechanics and Engineering*, Vol.25, 1981.

133. Stephenson, P. L., 'A Theoretical Study of Heat Transfer in Two-Dimensional Turbulent Flow in a Circular Pipe and between Parallel and Diverging Plates', *J. of Heat and Mass Transfer*, Vol.19, 1976.

134. Launder, B. E., Morse, A., Rodi, W., and Spalding, D. B., 'The Prediction of Free Shear Flows - A Comparison of the Performance of Six Turbulence Models', *Proceedings of the NASA Langley Free Turbulent Shear Flows Conference*, Vol.1, NASA SP-320, 1972.

135. Durst, F. and Rastogi, A. K., 'Theoretical and Experimental Investigations of Turbulent Flows with Separation', *Symposium on Turbulent Shear Flow*, April 18-20, 1977, University Park, Pennsylvania, Vol.1.

136. Ha Minh, H. and Chassaing, P., 'Perturbations of Turbulent Pipe Flow', *Symposium on Turbulent Shear Flow*, April 18-20, 1977, University Park, Pennsylvania, Vol.1.

137. Rastogi, A. K. and Rodi, W., 'Calculation of General Three-Dimensional Turbulent Boundary Layers', *AIAA J.*, Vol.16, 1978, pp.151-159.

138. Sharma, D., 'Turbulent Convective Phenomena in Straight Rectangular Sectioned Diffusers', Ph. D. Thesis, Univ. of London, 1974.

139. McGuirk, J. J. and Rodi, W., 'The Calculation of Three-Dimensional Turbulent Free Jets', *Turbulent Shear Flows I*, ed. by F. Durst, B. E. Launder, F. W. Schmidt, and J. H. Whitelaw, Springer-Verlag, 1979, pp.71-83..

140. Launder, B. E. and Sharma, B. I., 'Application of the Energy-Dissipation Model of Turbulence to the Calculation of Flow Near a Spinning Disk', *Letters in Heat and Mass Transfer*, Vol.1, 1974, pp.131-138.

141. Rodi, W., 'The Prediction of Free Turbulent Boundary Layers by Use of Two-Equation Model of Turbulence', Ph. D. Thesis, Univ. of London, 1972.

142. Pourahmadi, F. and Humphrey, J. A. C., 'Prediction of Curved Channel Flow with an Extended $k-\varepsilon$ Model of Turbulence', *AIAA J.*, Vol.21, 1983, pp.1365-1373.

143. Rodi, W. and Scheurer, G., 'Calculation of Curved Shear Layers with Two-Equation Turbulence Models', *The Physics of Fluids*, Vol.26, 1983, pp.1422-1436.

144. Kubo, L. and Gouldin, F. C., 'Numerical Calculations of Turbulent Swirling Flow', *J. of Fluids Engineering*, September 1975, pp.310-315.

145. Leschziner, M. A. and Rodi, W., 'Computation fo Strongly Swirling Axisymmetric Free Jets', *AIAA J.*, Vol.22, No.12, 1984.

146. Launder, B. E., Priddin, C. H., and Sharma, B. I., 'The Calculation of Turbulent Boundary Layers on Spinning and Curved Surfaces', *J. of Fluids Engineering*, 1977.

147. Chen, C. J. and Rodi, W., 'A Mathematical Model for Stratified Turbulent Flows and Its Application to Bouyant Jets', *Sixteenth IAHR Congress*, Paper C4, Sao Paulo, 1975.

148. Plumb, O. A. and Kennedy, L. A., 'Applicaiton of the $k-\varepsilon$ Turbulence Model to Natural Convection from a Vertical Isothermal Surface', *J. of Heat Transfer*, Trans. ASME, 99, 1977, pp.79-85.

149. Chien, K.-Y., 'Prediction of Channel and Boundary-Layer Flows with a Low-Reynolds-Number Turbulence Model', *AIAA J.*, Vol.20, No.1, 1982.

150. Mellor, G. L. and Herring, H. J., 'A Survey of the Mean Turbulent Field Closure Models', *AIAA J.*, Vol.11, 1973, pp.590-599.

151. Chou, P. Y., 'Pressure Flow of a Turbulent Fluid between Two Infinite Parallel Planes', *Quarterly of Applied Mathematics* , Vol.3, 1945, pp.198-209.

152. Daly, B. J. and Harlow, F. H., 'Transport Equations in Turbulence' , *The Physics of Fluids*, Vol.13, No.11, 1970.

153. Irwin, H. P. A. H., 'Measurements of a Self-Preserving Plane Wall Jet in a Positive Pressure Gradient', *J. of Fluid Mechanics*, Vol.61, 1973, pp.33.

154. Irwin, H. P. A. H., 'Measurements in Blown Boundary Layers and Their Prediction by Reynolds Stress Modeling', Ph. D. Thesis, McGill Univ., Dept. of Mech. Eng., 1974.

155. Lumley, J. L., 'Prediction Methods for Turbulent Flow - Introduction', Von Karman Inst. for Fluid Dynamics, LS-76, 1975.

156. Naot, D., Shavit, A., and Wolfshtein, M., 'Interactions between Components of the Turbulent Velocity Correlation Tensor Due to Pressure Fluctuations', *Israel J. of Technology*, Vol.8, 1970, p.259.

157. Reynolds, W. C., 'Computation of Turbulent Flows - State-of-the Art', Dept. of Mech. Eng., Stanford Univ., Report MD-27, 1970.

158. Donaldson, C. DuP., 'A Computer Study of an Analytical Model of Boundary-Layer Transition', *AIAA J.*, Vol.7, 1969, pp.271-278.

159. Harlow, F. H. and Nakayama, P. I., 'Turbulence Transport Equations', *The Physics of Fluids*, Vol.10, 1967, pp.2323-2332.

160. Tennekes, H. and Lumley, J. L., *A First Course in Turbulence*, MIT Press, 1972.

161. Lumley, J. L. and Khajeh Nouri, B., 'Computational Modeling of Turbulent Transport', *Advances in Geophysics*, Vol.18A, 1974, pp.169-192.

162. Lewellen, W. S., Teske, M. E., and Donaldson, C. duP., 'Variable Density Flows Computed by a Second-Order Closure Description of Turbulence', *AIAA J.*, Vol.13, No.3, 1976.

163. Gibson, M. M., 'An Algebraic Stress and Heat-Flux Model for Turbulent Shear Flow with Streamline Curvature', *Int'l J. of Heat and Mass Transfer*, Vol.21, 1978, pp.1609-1617.

164. Gibson, M. M., Jones, W. D., Mcguirk, J. J., and Whitelaw, J. H., *Lecture Notes : Turbulence Models for Computational Fluid Dynamics* , Pennsylvania State Univ., Univ. Park, 1981.

165. Gibson, M. M. and Rodi, W., 'A Reynolds-Stress Closure Model of Turbulence Applied to the Calculation of a Highly Curved Mixing Layer' , *J. of Fluid Mechanics*, Vol.103, 1981, pp.161-182.

166. Wilcox, D. C. and Rubesin, M. W., 'Progress in Turbulence Modeling for Complex Flow Fields Including the Effect of Compressibility', NACA TP 1517, 1980.

167. Rodi, W., 'Examples of Turbulence Models for Incompressible Flows', *AIAA J.*, Vol.20, 1982.

168. Deardorff, J. W., 'Three-Dimensional Numerical Study of Turbulence in an Entraining Mixed Layer', *Boundary-Layer Metereology*, Vol.7, 1974, pp.199-226.

169. Schumann, U., 'Realizability of Reynolds-Stress Turbulence Model' , *The Physics of Fluids*, Vol.20, No.5, 1977.

170. Rodi, W., 'A New Algebraic Relation for Calculating the Reynolds Stresses', *ZAMM*, 1976, T219-221.

171. Launder, B. E. and Ying, W. M., 'The Prediction of Flow and Heat Transfer in Ducts of Square Cross-Section', *Proc. Inst. Mech. Engrs.*, 187, 1973, pp.37-73.

172. Meroney, R. N., 'An Algebraic Stress Model for Stratified Turbulent Shear Flows', *Computers and Fluids*, Vol.4, 1976, pp.93-107.

173. Launder, B. E., 'On the Effect of a Gravitational Field on the Turbulence Transport of Heat and Momentum', *J. of Fluid Mechanics*, Vol.67, 1975, pp.569-581.

174. Gibson, M. M. and Launder, B. E., 'Ground Effects on Pressure Fluctuations in the Atmospheric Boundary Layer', *J. of Fluid Mechanics*, Vol.86, 1978, p.491.

175. Lilly, D. K., 'The Representation of Small-Scale Turbulence in Numerical Simulation Experiments', *Proc. of IBM Scientific Computing Symposium on Environmental Science*, 1967, pp.195-210.

176. Deardorff, J. W., 'A Numerical Study of Three-Dimensional Turbulent Channel Flow at Large Reynolds Number', *J. of Fluid Mechanics*, Vol.41, 1970, pp.453-480.

177. Deardorff, J. W., 'The Use of Subgrid Transport Equations in a Three-Dimensional Model of Atmospheric Turbulence', *J. of Fluids Engineering*, Vol.95, 1973, pp.429-438.

178. Schumann, U., 'Subgrid Scale Model for Finite Difference Simulations of Turbulent Flows in Plane Channels and Annuli', *J. of Computational Physics*, Vol.18, 1975, pp.376-404.

179. Kwak, D., Reynolds, W. C., and Ferziger, J. H., 'Three-Dimensional Time Dependent Computations of Turbulent Flow', Dept. of Mech. Eng., Report TF-5, Stanford Univ., 1975.

180. Shaanan, S., Ferziger, J. H., and Reynolds, W. C., 'Numerical Simulation of Trubulence in the Presence of Shear', Dept. of Mech. Eng., Report TF-6, Stanford Univ., 1975.

181. Love, M. D. and Leslie, D. C., 'Studies of Subgrid Modeling with Classical Closures and Burgers Equations', *Turbulent Shear Flows I*, ed. by F. Durst, B. E. Launder, F. W. Schmidt, and J. H. Whitelaw, Springer-Verlag, 1979, pp.353-369.

182. Van Driest, E. R., 'On the Turbulent Flow Near a Wall', *J. of the Aeronautical Sciences*, Vol.23, 1956, pp.1007-1011.

183. Amano, R. S. and Neusen, K. F., 'A Numerical and Experimental Investigation of High Velocity Jets Impinging on a Flat Plate', *Proc. Sixth Int'l Symp. Jet Cutting Technol.*, April 1982, P.107.

184. Hoffman, G. H., 'Improved Form of the Low Reynolds Number $k-\varepsilon$ Turbulence Model', *The Physics of Fluids*, Vol.18, No.3, 1975.

185. Hassid, S. and Poreh, M. 'A Turbulent Energy Dissipation Model for Flows with Drag Reduction', *J. of Fluids Engineering*, Vol.100, March 1978.

186. Dutoya, D. and Michard, P., 'A Program for Calculating Boundary Layers along Compressor and Turbine Blades', *Numerical Methods in Heat Transfer*, edited by R. W. Lewis, K. Morgan, O. C. Zienkiewicz, John Wiley and Sons, New York, 1981.

187. Lam, C. K. G. and Bremhorst, K. A., 'Modified Form of the $k-\varepsilon$ Model for Predicting Wall Turbulence', *J. of Fluids Engineering*, Vol.103, 1981, pp.456-460.

188. Patel, V. C., Rodi, W., and Scheurer, G., 'Turbulence Models for Near-Wall and Low Reynolds Number Flows : A Review', *AIAA J.*, Vol.23, No.9, 1985.

189. Hinze, J. O., *Turbulence*, Second ed., Mcgraw-Hill, New York, 1975.

190. Iacovides, H. and Launder, B. E., 'PSL-an Economical Approach to the Numerical Analysis of Near-Wall, Elliptic Flow', *J. of Fluids Engineering*, Vol.106, June 1984.

191. Launder, B. E., 'Numerical Computation of Convective Heat Transfer in Complex Turbulent Flows : Time to Abandon Wall Functions', *J. of Heat and Mass Transfer*, Vol.27, No.9, 1984, pp.1485-1491.

192. Clauser, F. H., 'The Turbulent Boundary Layer', *Advances in Applied Mechanics*, Vol.4, 1956.

193. Courant, R., 'Variational Methods for the Solution of Problems of Equilibrium and Vibrations', *The Bulletin of the American Mathematical Society*, Vol.49, 1943, pp.1-23.

194. Courant, R., *Calculus of Variations and Supplementary Notes Exercises*, Supplementary Notes by M. Kruskal and H. Rubin, Revised by J. Moser, New York Univ., 1956-1957.

195. Finlayson, B. A., *The Method of Weighted Residuals and Variational Principles*, Academic Press, 1972.

196. Engelman, M. S. and Sani, M. S., 'Consistent and Reduced Integration Penalty Methods for Incompressible Media Using Several Old and New Elements', *Int'l J. for Numerical Methods in Fluids*, Vol.2, 1982, pp.25-42.

197. Mitra, P. S., Neu, W. L., and Schetz, J. A., 'Effects of a Free Surface on the Wake of a Slender Body', Virginia Tech., Dept. of Aero. and Ocean Eng., Report VPI-AERO-146, 1985.

198. Mitra, P. S., Neu, W. L., and Schetz, J. A., 'Effects of a Free Surface on the Wake of a Self-Propelled Slender Body', Virginia Tech., Dept. Aero. and Ocean Eng., Report VPI-AERO-153, 1986.

199. Holland, S., Neu, W. L., and Schetz, J. A., Unpublished Work, Virginia Tech., Dept. Aero. and Ocean Eng., 1986.

200. Kaplan, P., Private Communication, 1987.

201. Schetz, J. A. and Figard, R. L., 'Numerical Solution of the Flow Near the Rotor of a Horizontal-Axis Wind Turbine and Comparison with Data', *AIAA/SERI Wind Energy Conference*, Paper 80-0608, Boulder, Colorado, April 9-11, 1980.

202. Schetz, J. A. and Figard, R. L., 'Numerical Solution of the Flow Near the Rotor of a Wind Turbine', *J. of Energy*, Vol.6, No.2, 1982.

203. Anderson, D. A., Tannehill, J. C., and Pletcher, R. H., *Computational Fluid Mechanics and Heat Transfer*, McGraw-Hill, 1984, pp.191-193.

204. Laufer, J., 'The Structure of Turbulence in Fully Developed Pipe Flow', *NACA Report*, 1174, 1954.

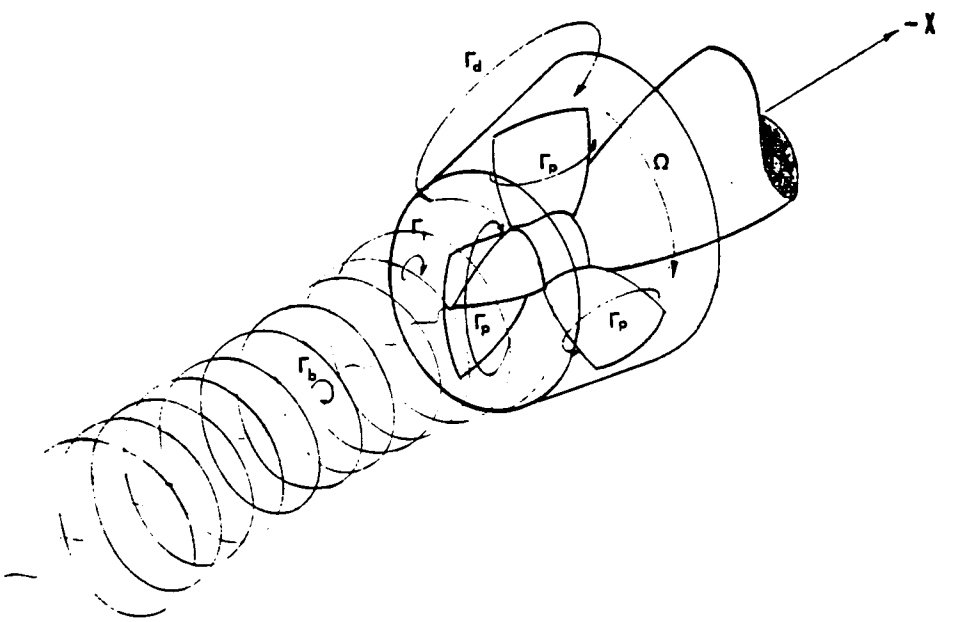

Figure 1. Vortex system of ducted propeller

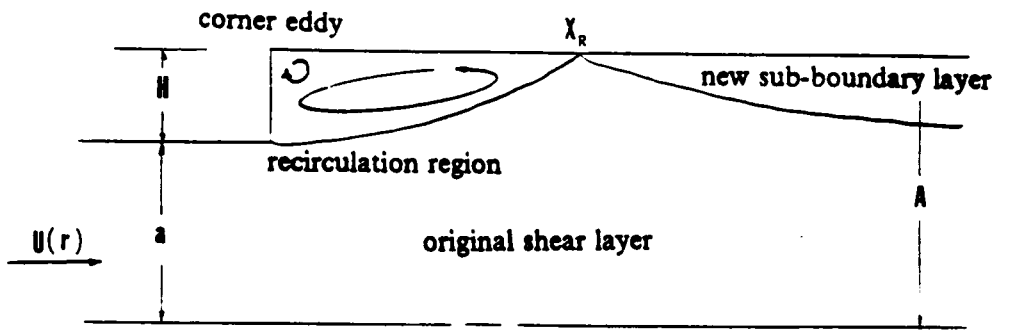

(a) general behavior of reattaching flow

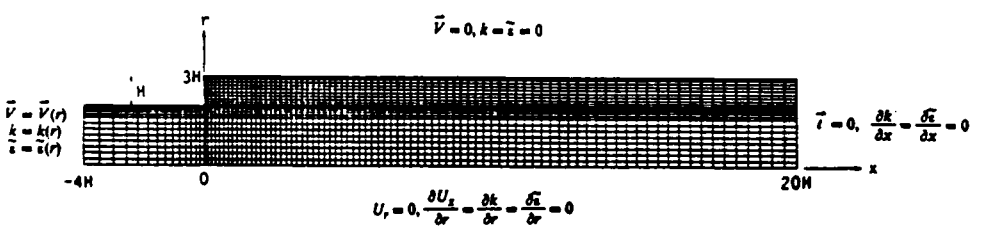

(b) compuational domain, mesh, and boundary conditions

Figure 2. Sudden pipe expansion: General behavior and computational domain. downstream of the step.

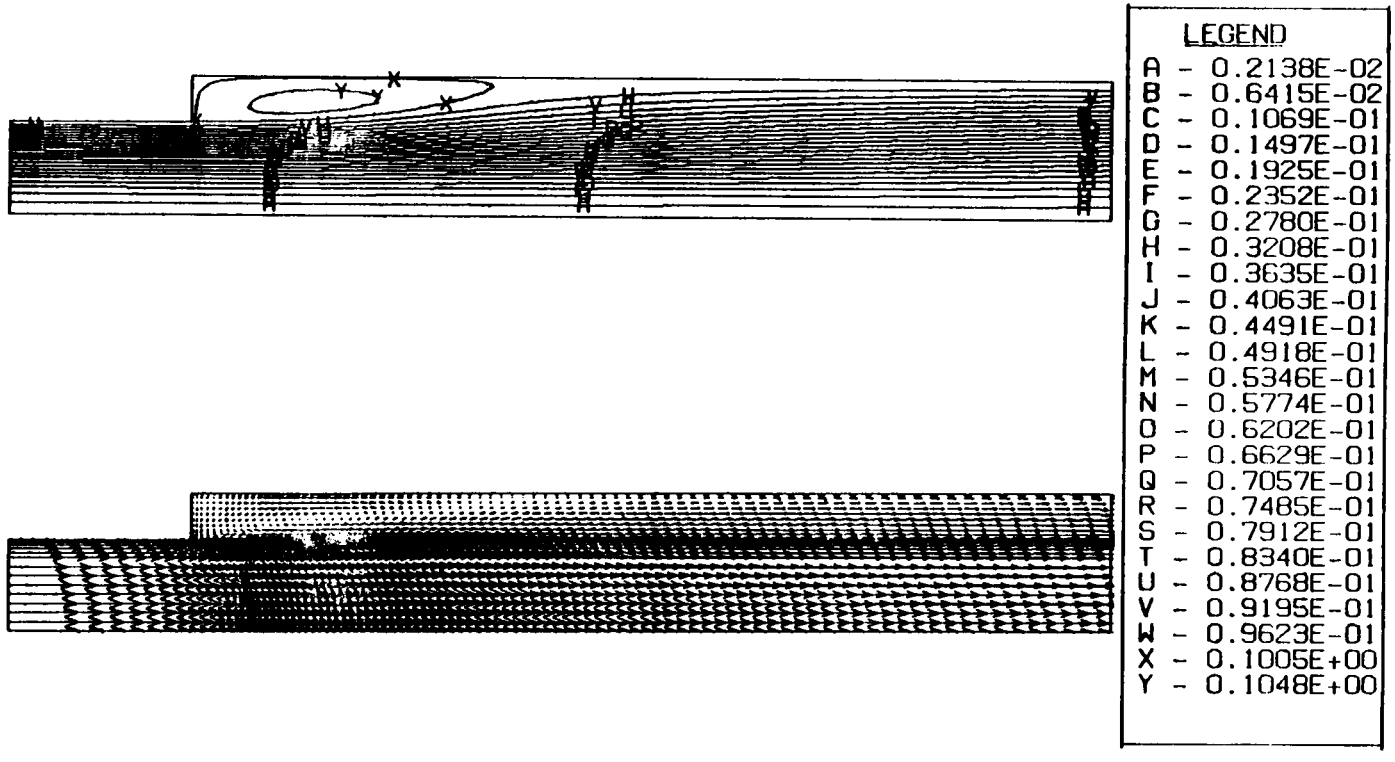

Figure 3. Sudden pipe expansion: Streamline contours and velocity vectors.

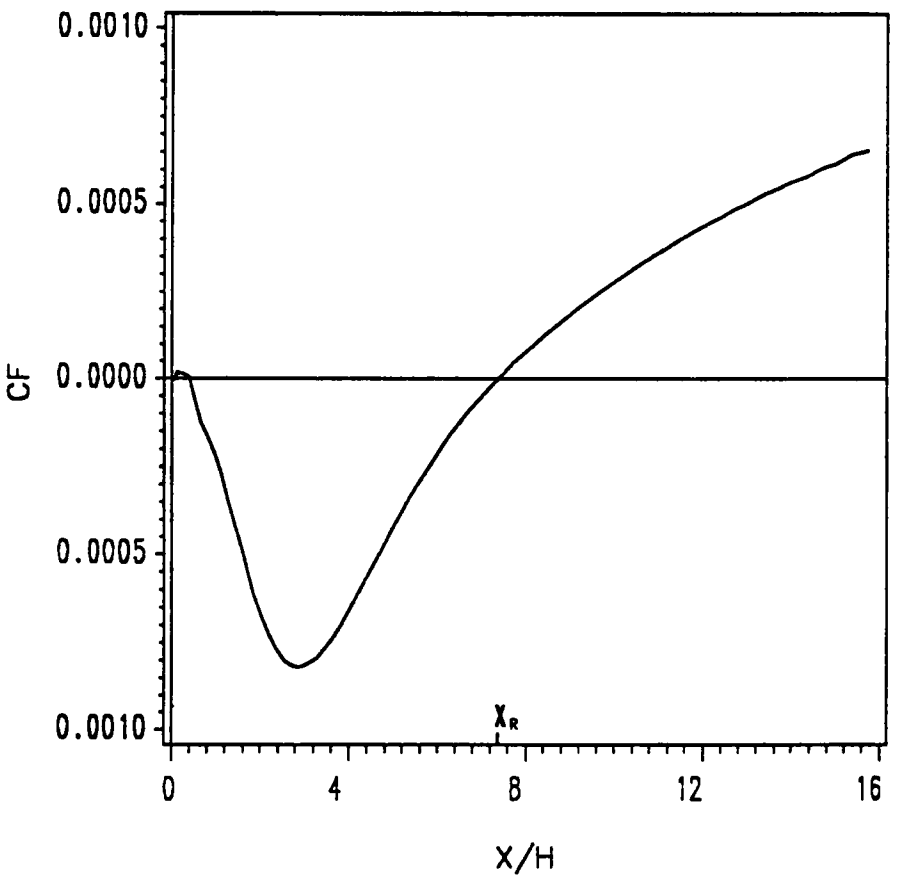

Figure 4. Sudden pipe expansion: Predicted skin friction coefficient variation downstream of the step.

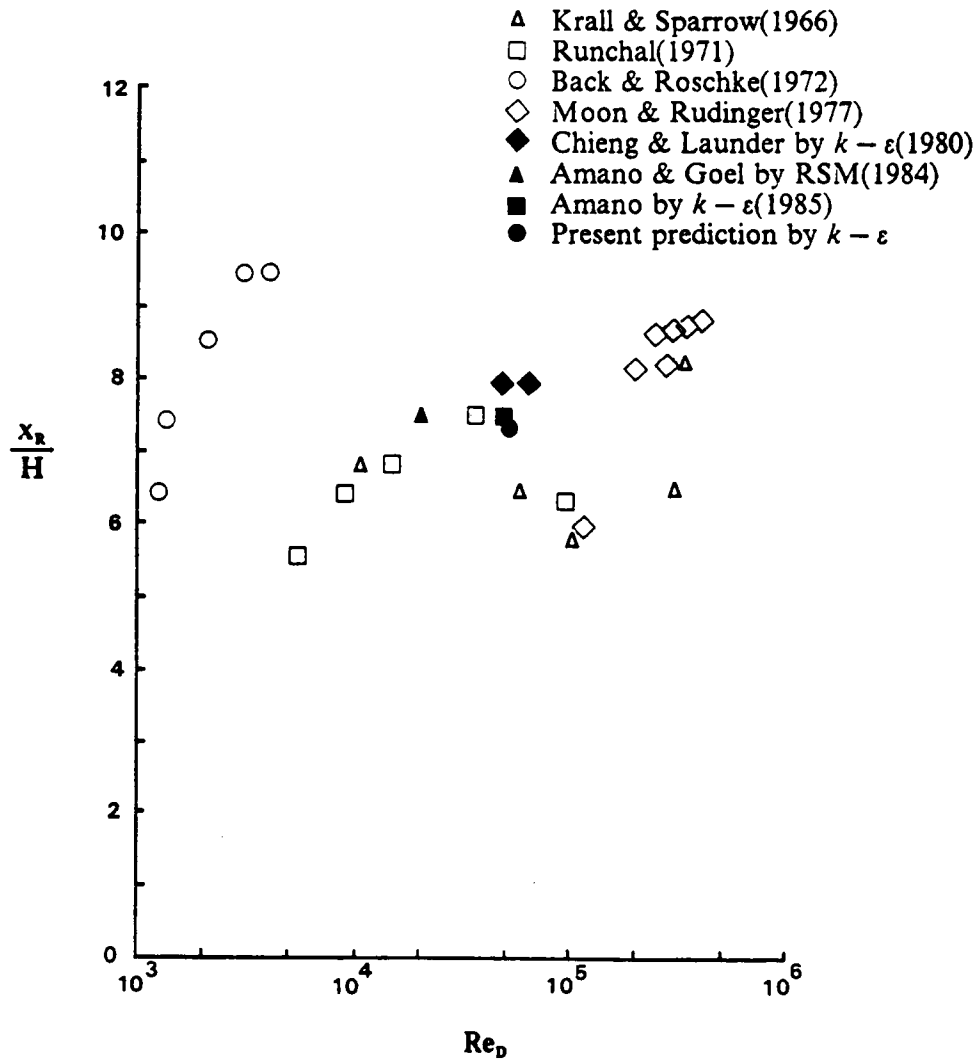

Figure 5. Sudden pipe expansion: Comparison of the predicted reattachment distance with measurements and other predictions.

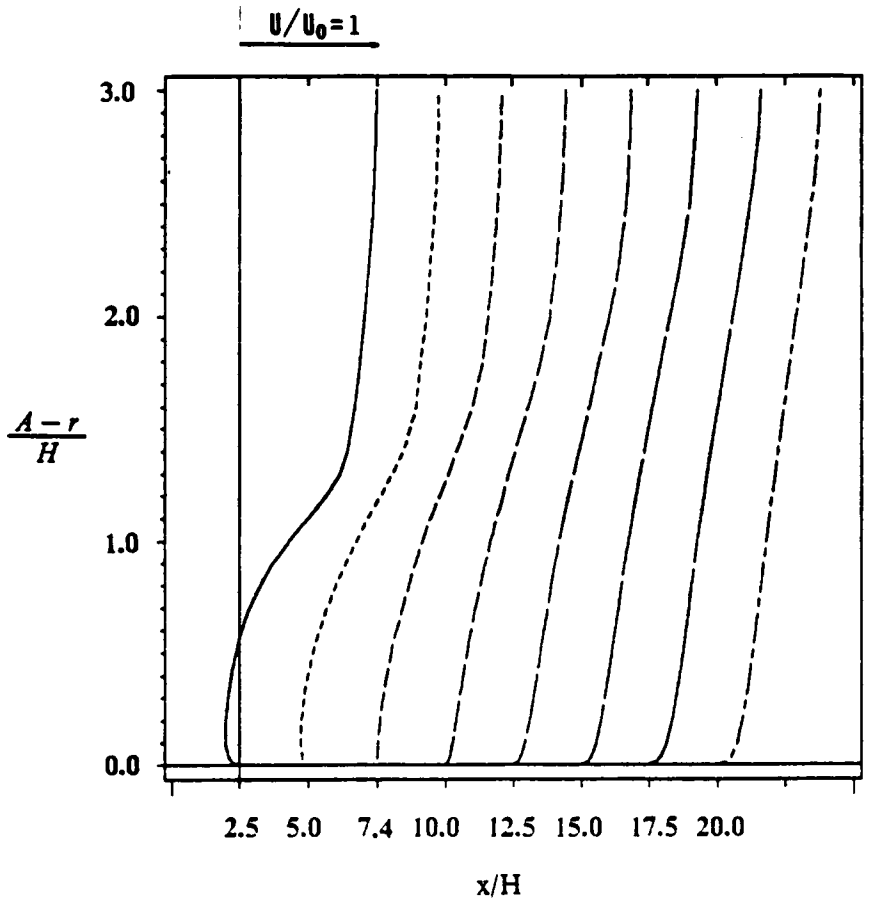

Figure 6. Sudden pipe expansion: Predicted axial velocity profiles along radial direction at eight locations, x/H = 2.5, 5.0, 7.4($= x_R$), 10.0, 12.5, 15.0, 17.5, 20.0, downstream of the step.

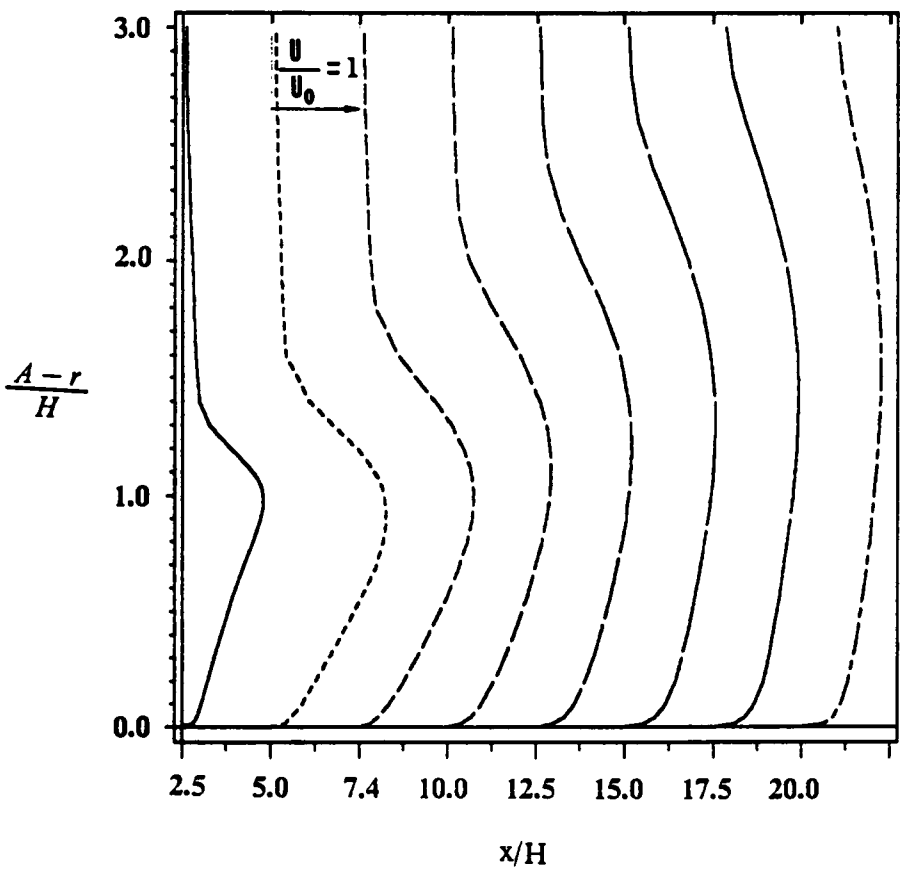

Figure 7. Sudden pipe expansion: Predicted turbulent kinetic energy profiles along radial direction at eight locations, x/H = 2.5, 5.0, 7.4($= x_R$), 10.0, 12.5, 15.0, 17.5, and 20.0, downstream of the step.

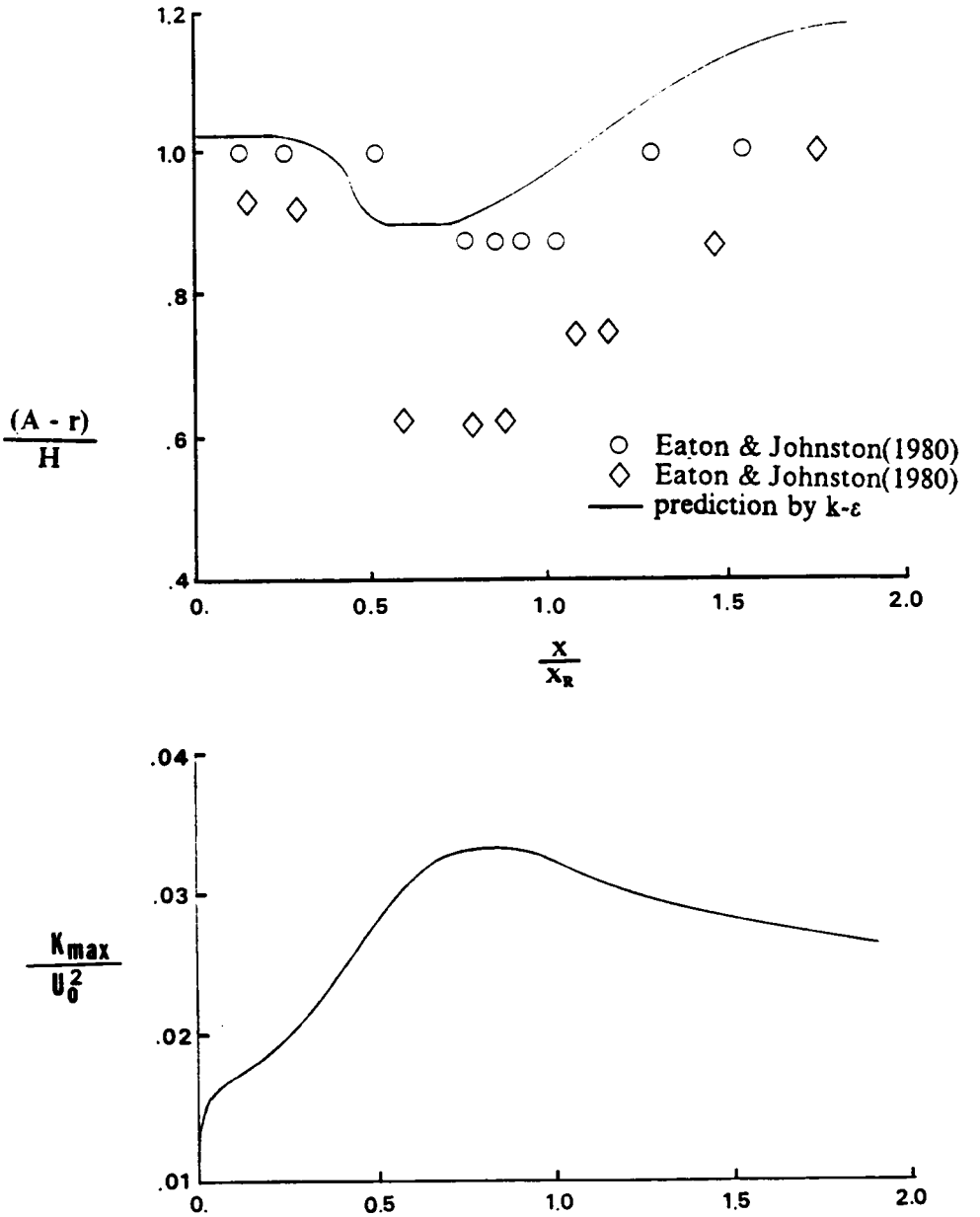

Figure 8. Sudden pipe expansion: The trace and value of the maximum turbulent kinetic energy along streamline direction downstream of the step.

All dimensions in inches

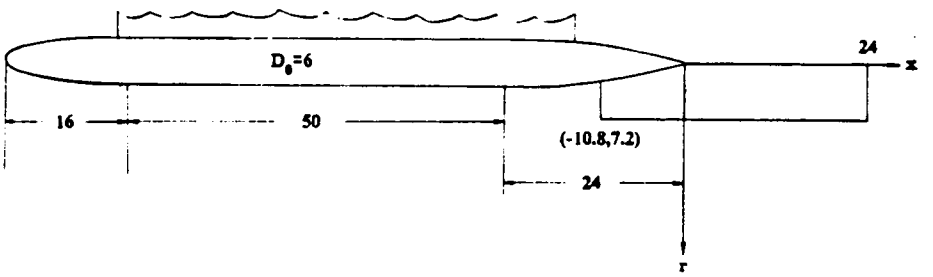

(a) computational domain

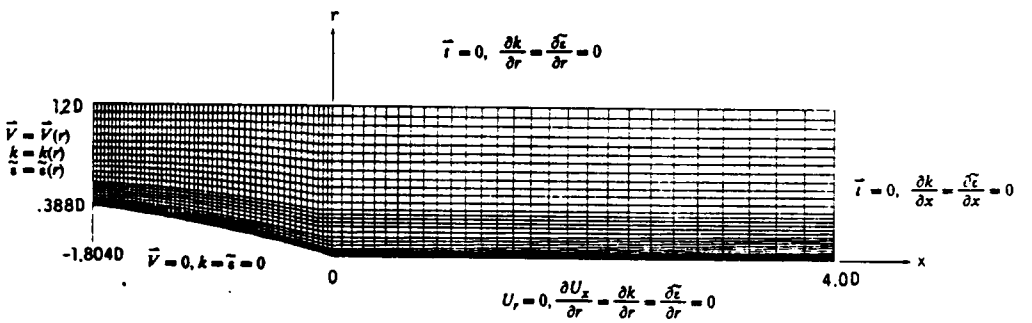

(b) generated mesh and boundary conditions

Figure 9. Stern region flow: Computational domain, mesh, and boundary conditions.

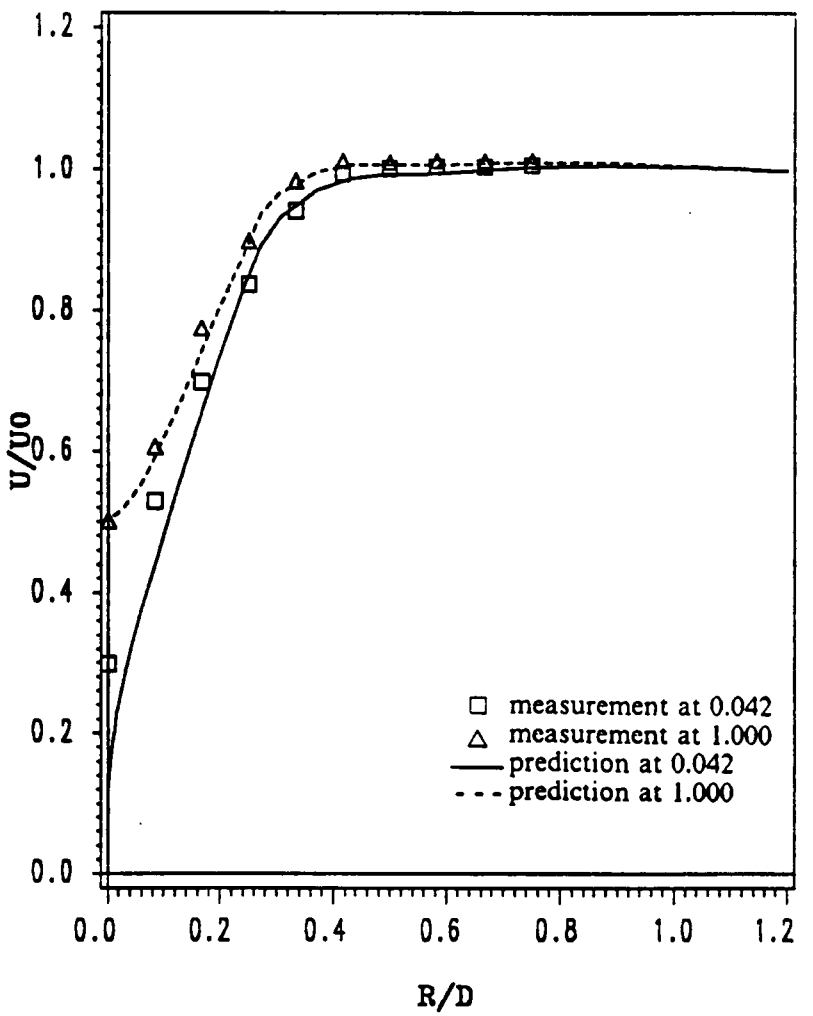

Figure 10. Stern region flow: Comparison of axial velocity profiles along radial direction at two locations, x/D = 0.042 and 1.000.

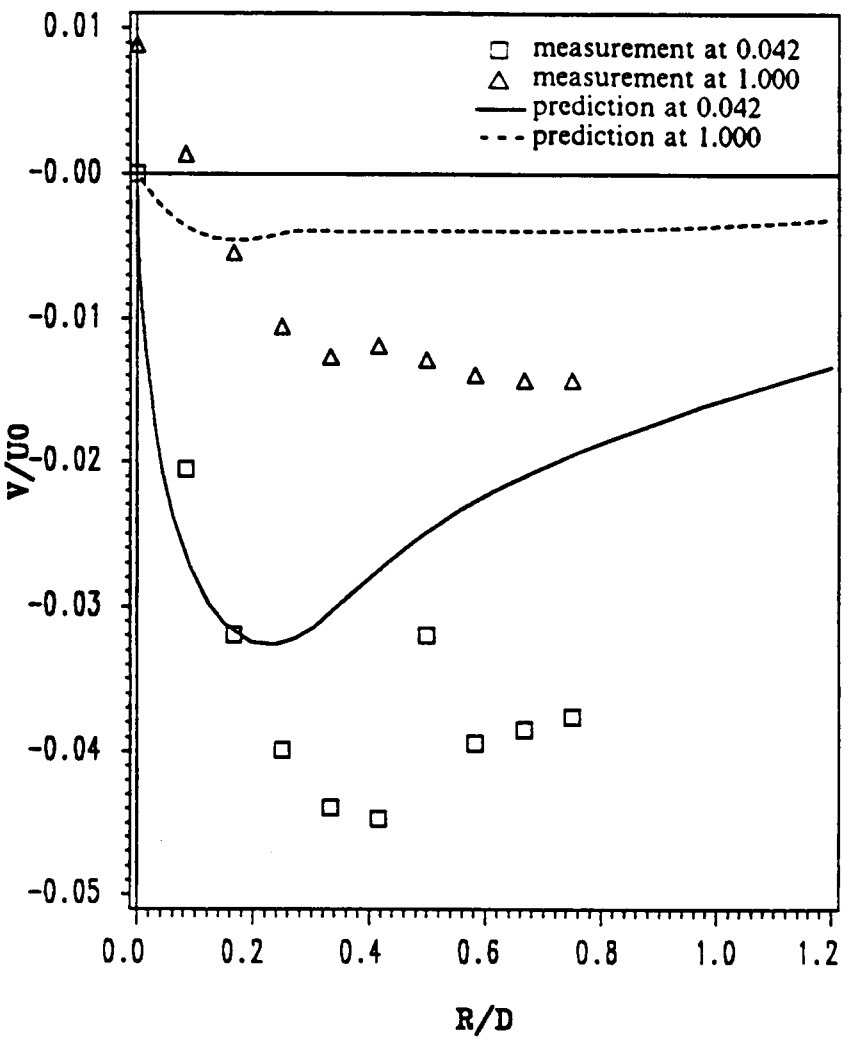

Figure 11. Stern region flow: Comparison of radial velocity profiles along radial direction at two locations, x/D = 0.042 and 1.000.

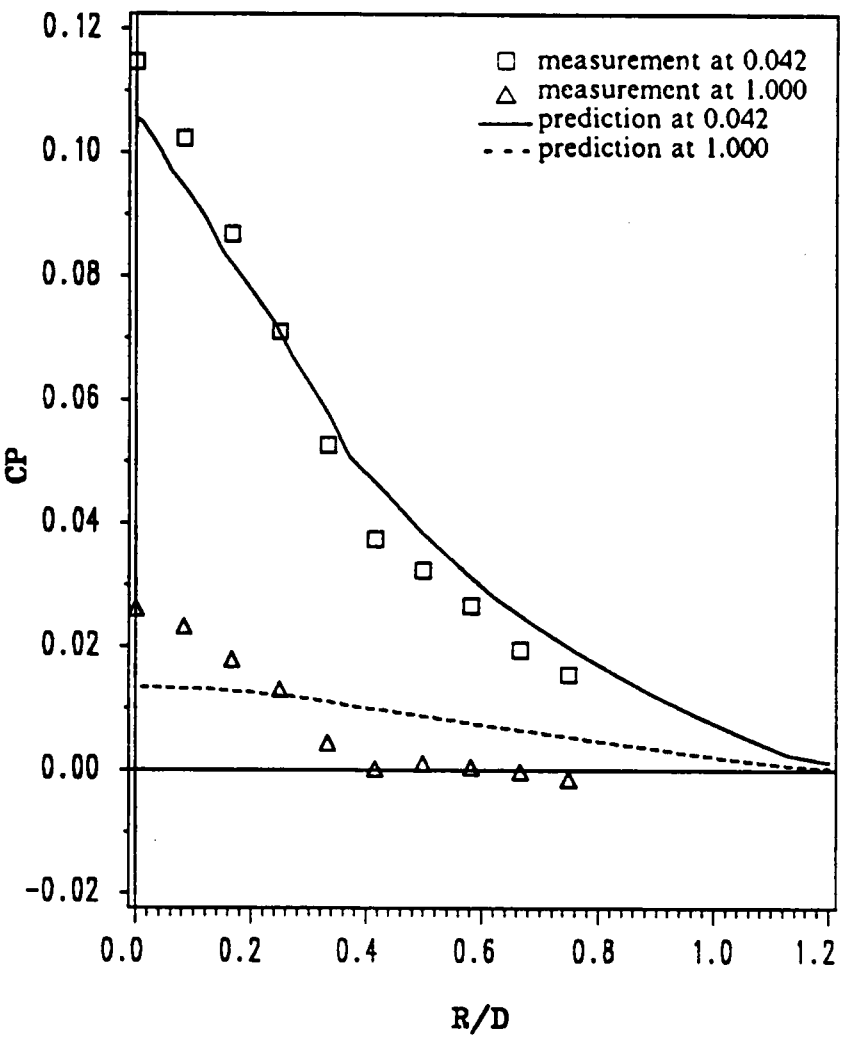

Figure 12. Stern region flow: Comparison of pressure coefficient profiles along radial direction at two locations, x/D = 0.042 and 1.000.

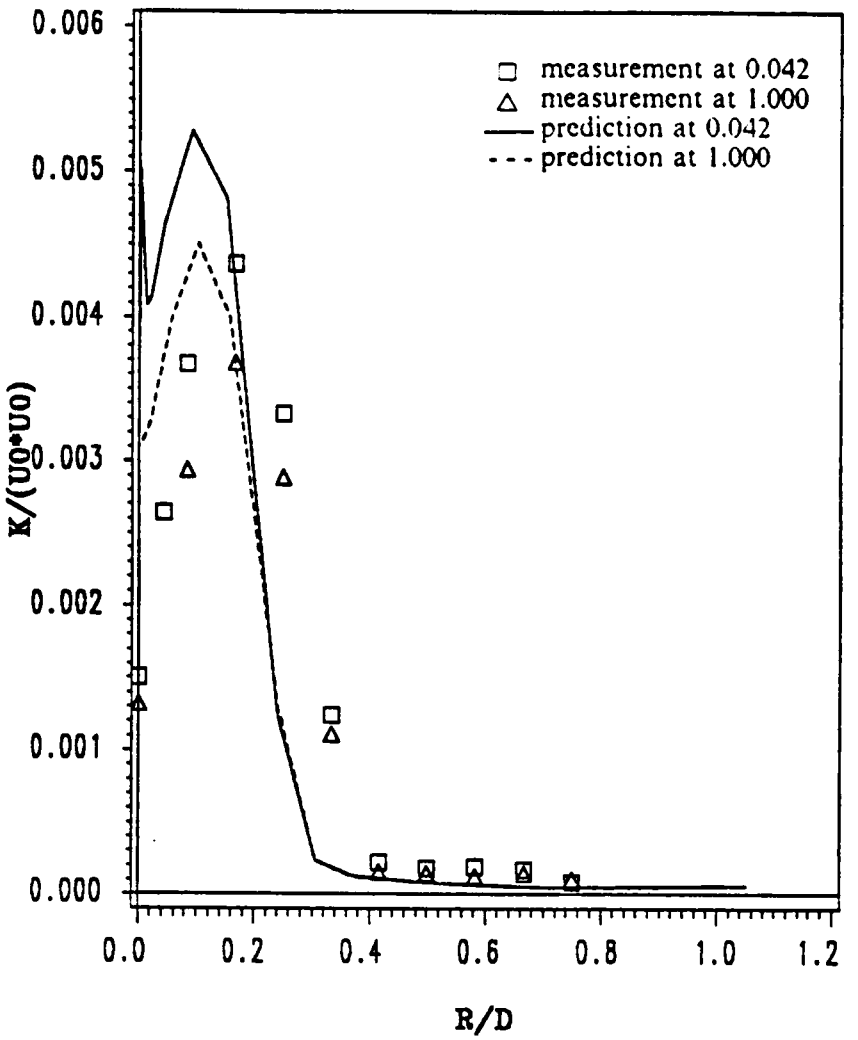

Figure 13. Stern region flow: Comparison of turbulent kinetic energy profiles along radial direction at two locations, x/D = 0.042 and 1.0.

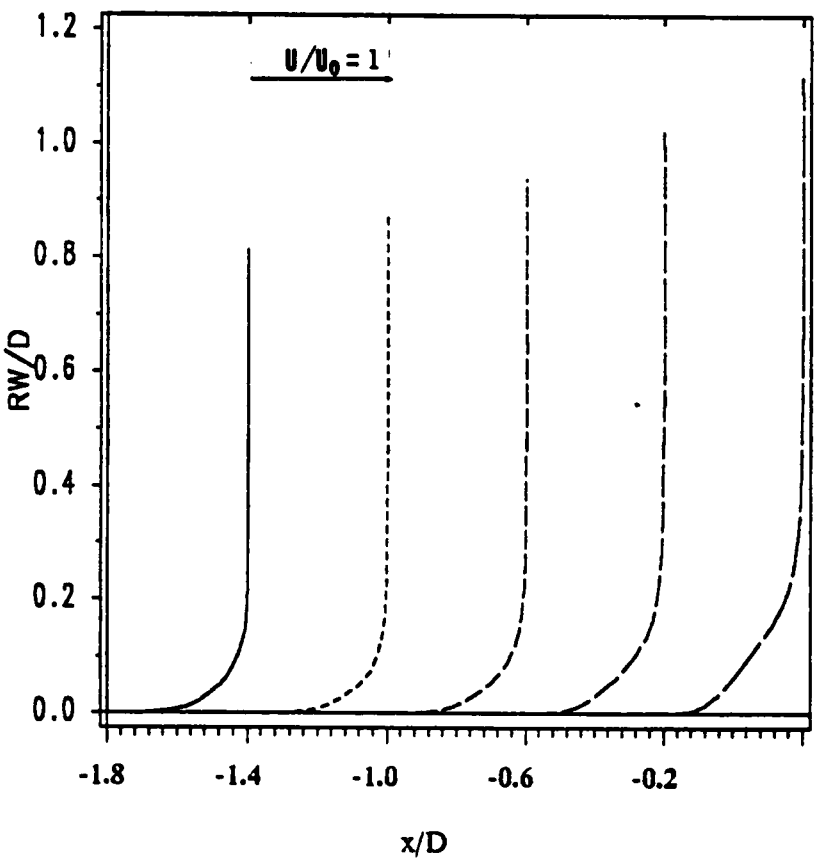

Figure 14. Stern region flow: Prediction of tangential velocity profiles in the boundary layer of the slender body at five locations, x/D = -1.8, -1.4, -1.0, -0.6, and -0.2.

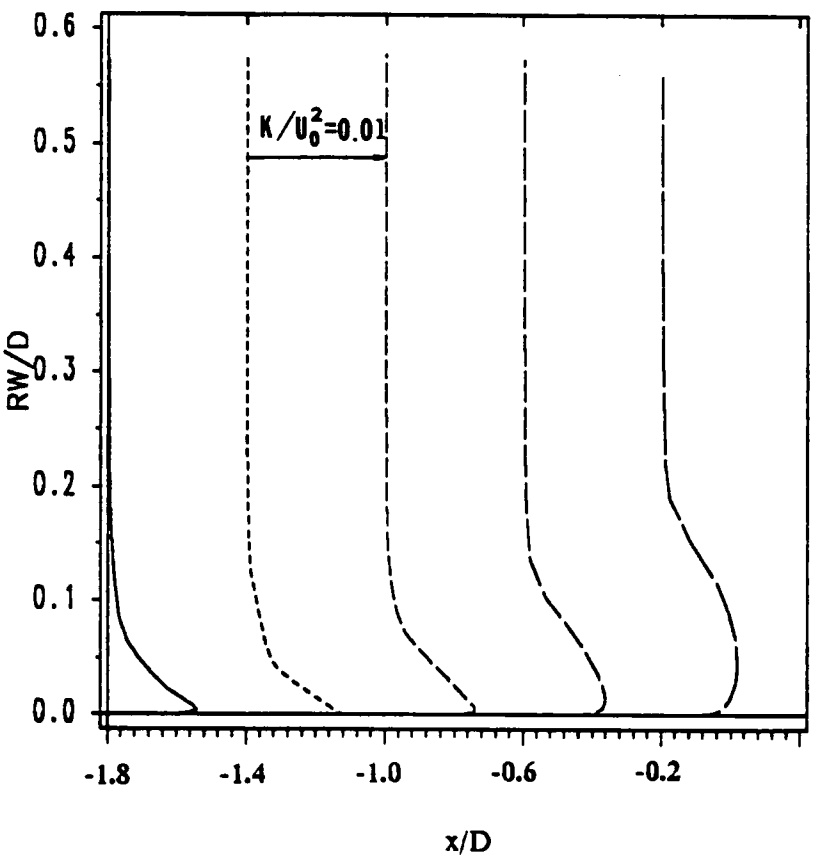

Figure 15. Stern region flow: Prediction of turbulent kinetic energy profiles in the boundary layer of the slender body at five locations, x/D = -1.8, -1.4, -1.0, -0.6, and -0.2.

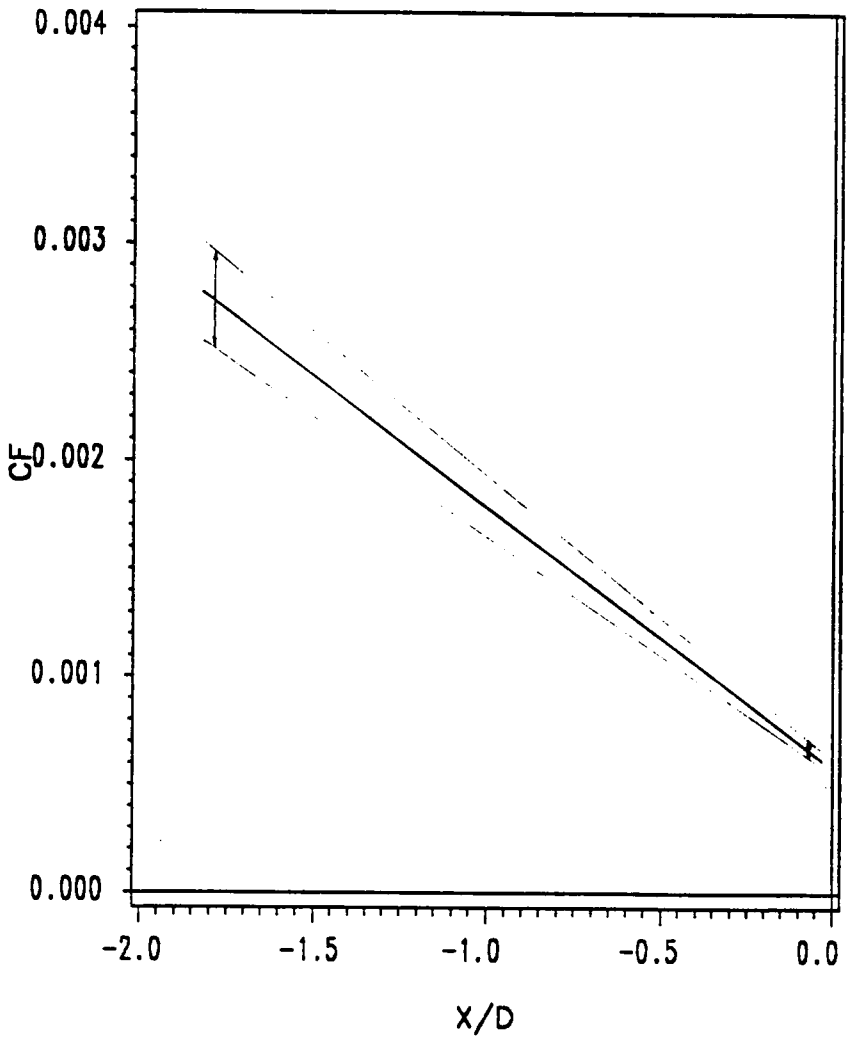

Figure 16. Stern region flow: Prediction of skin friction coefficient along body surface.

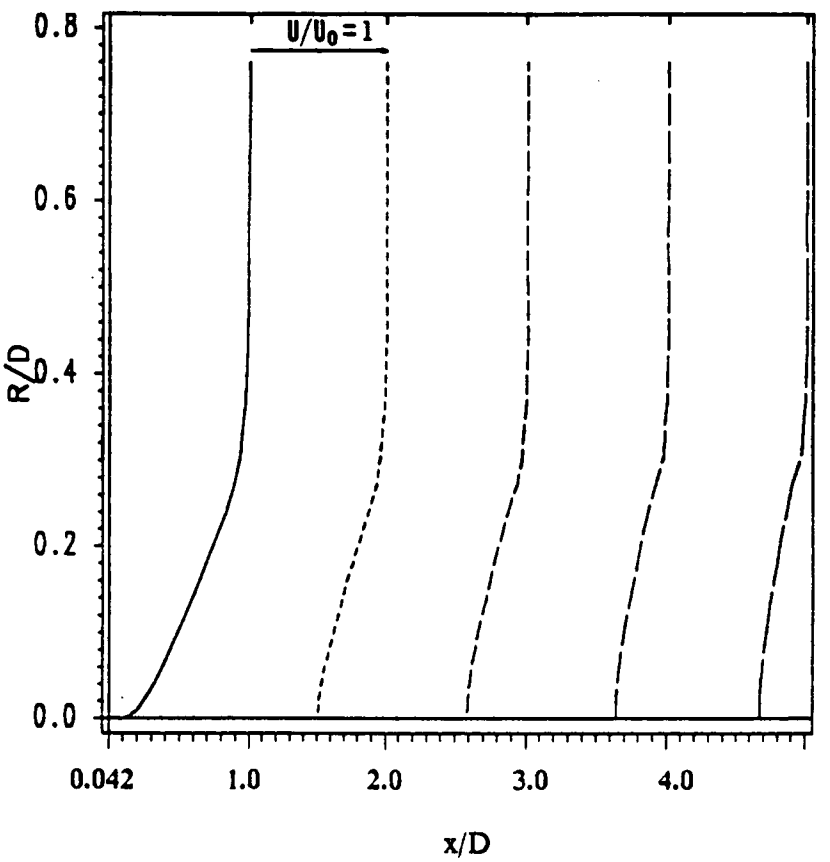

Figure 17. Stern region flow: Prediction of axial velocity profiles behind the slender body at five locations, x/D = 0.042, 1.0, 2.0, 3.0, and 4.0.

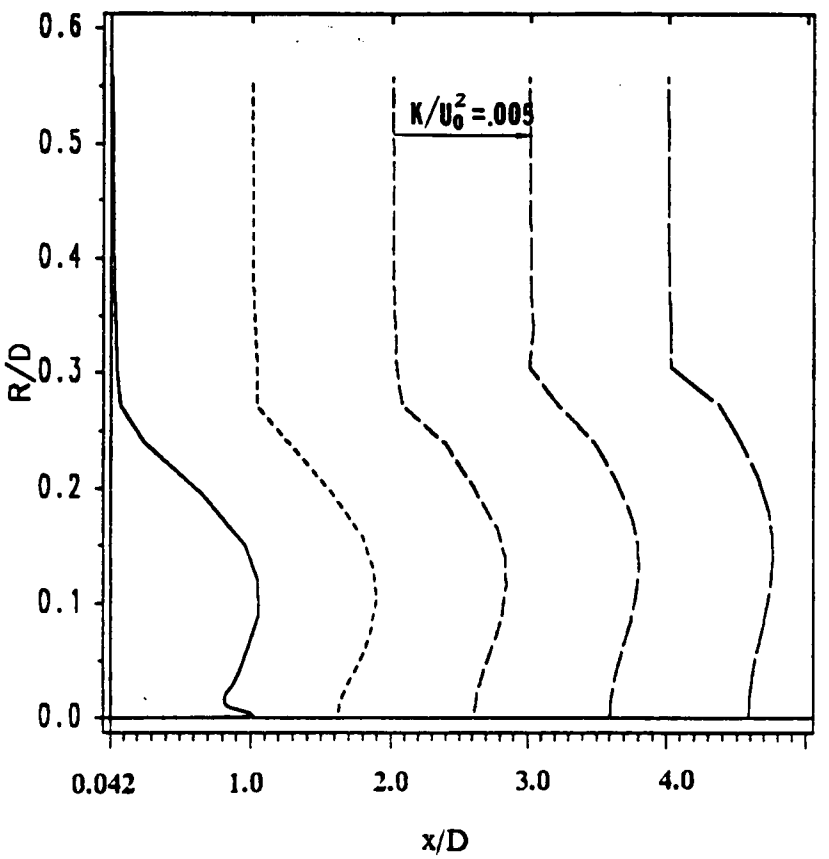

Figure 18. Stern region flow: Prediction of tuebulent kinetic energy profiles behind the slender body at five locations, x/D = 0.042, 1.0, 2.0, 3.0, and 4.0.

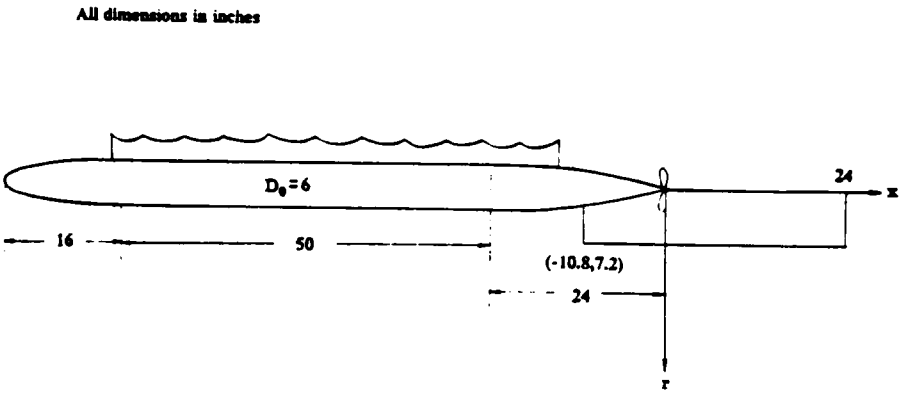

(a) computational domain

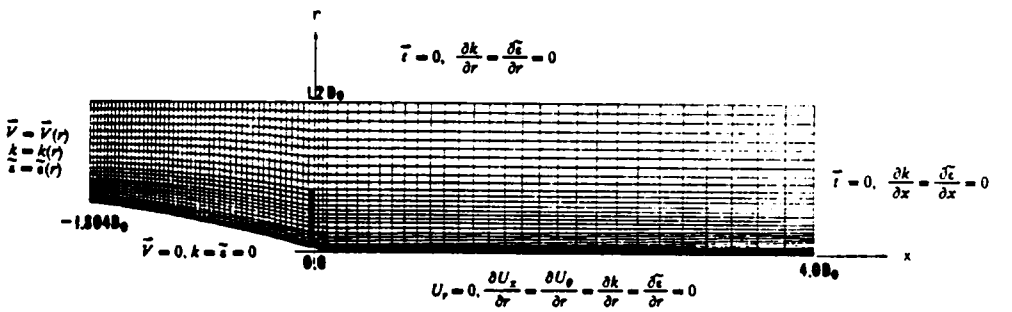

(b) generated mesh and boundary conditions

Figure 19. Self-propelled: Computational domain, mesh, and boundary conditions.

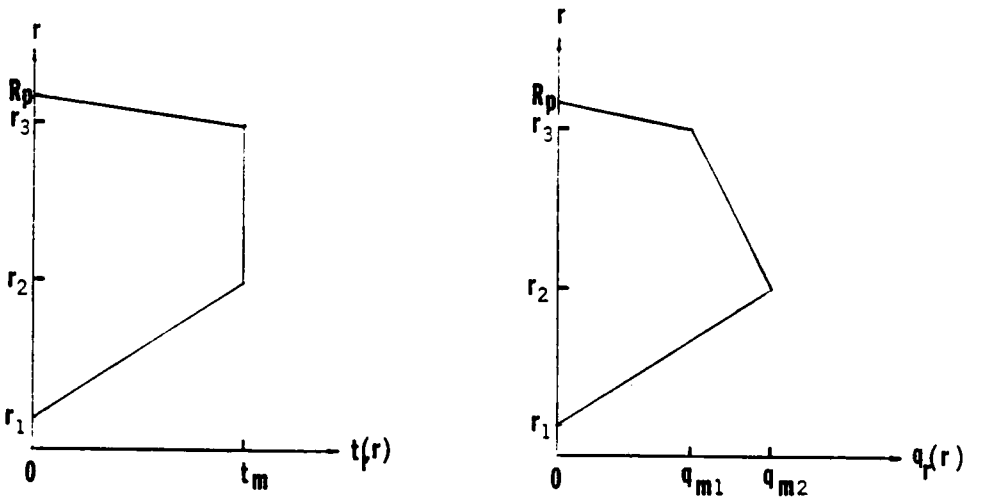

(a) nonducted propeller

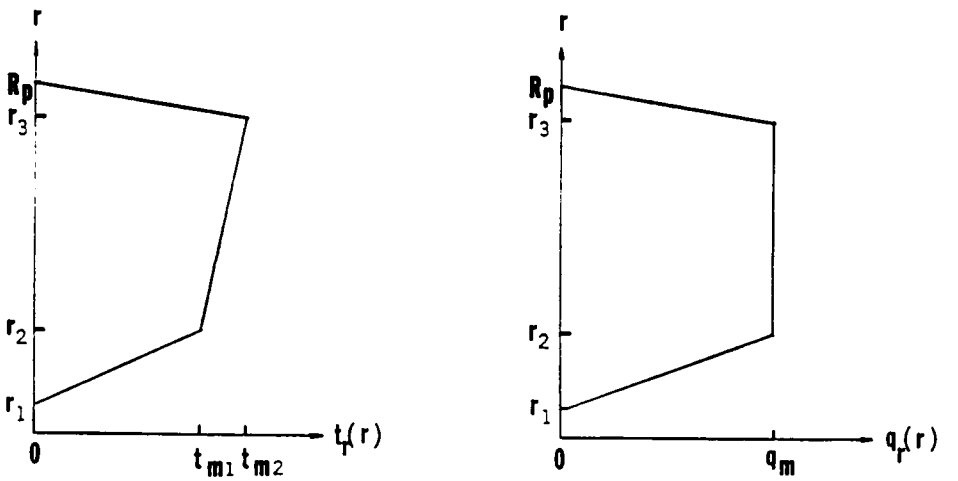

(b) ducted propeller

Figure 20. Radial distributions of thrust and torque: (a) nonducted and (b) ducted propellers.

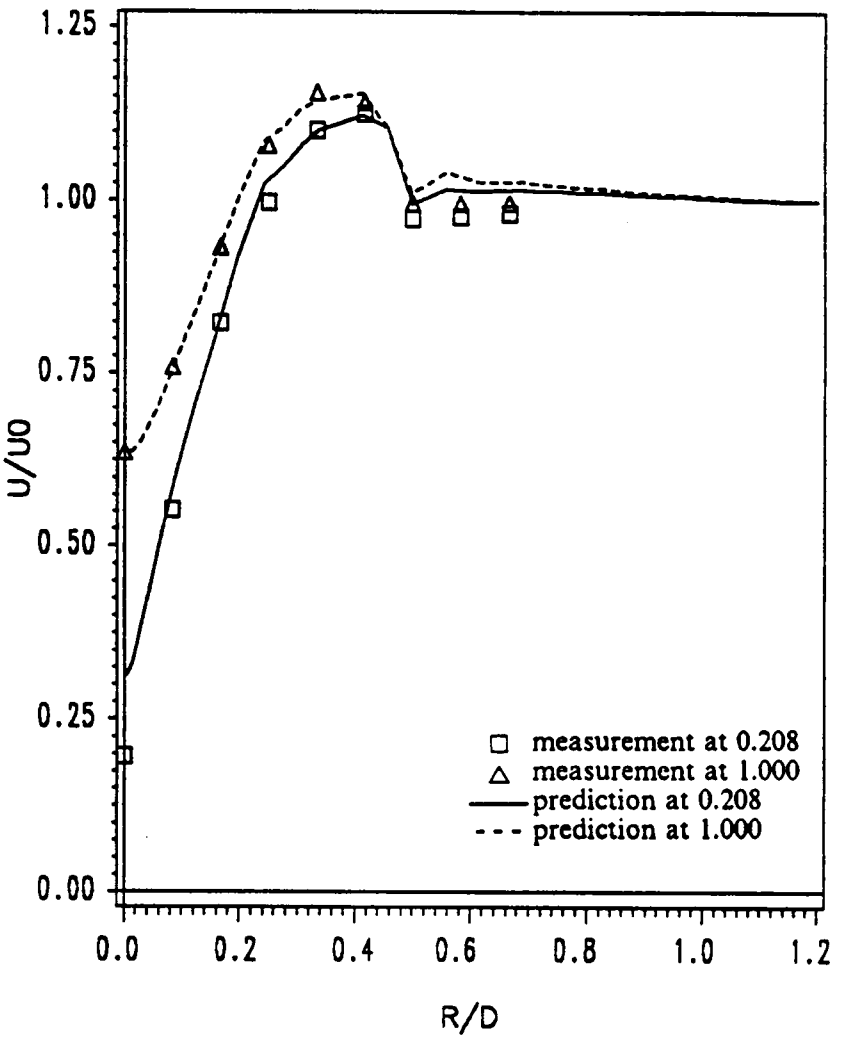

Figure 21. Self-propelled: Comparison of axial velocity profiles along radial direction at two locations, x/D = 0.208 and 1.0.

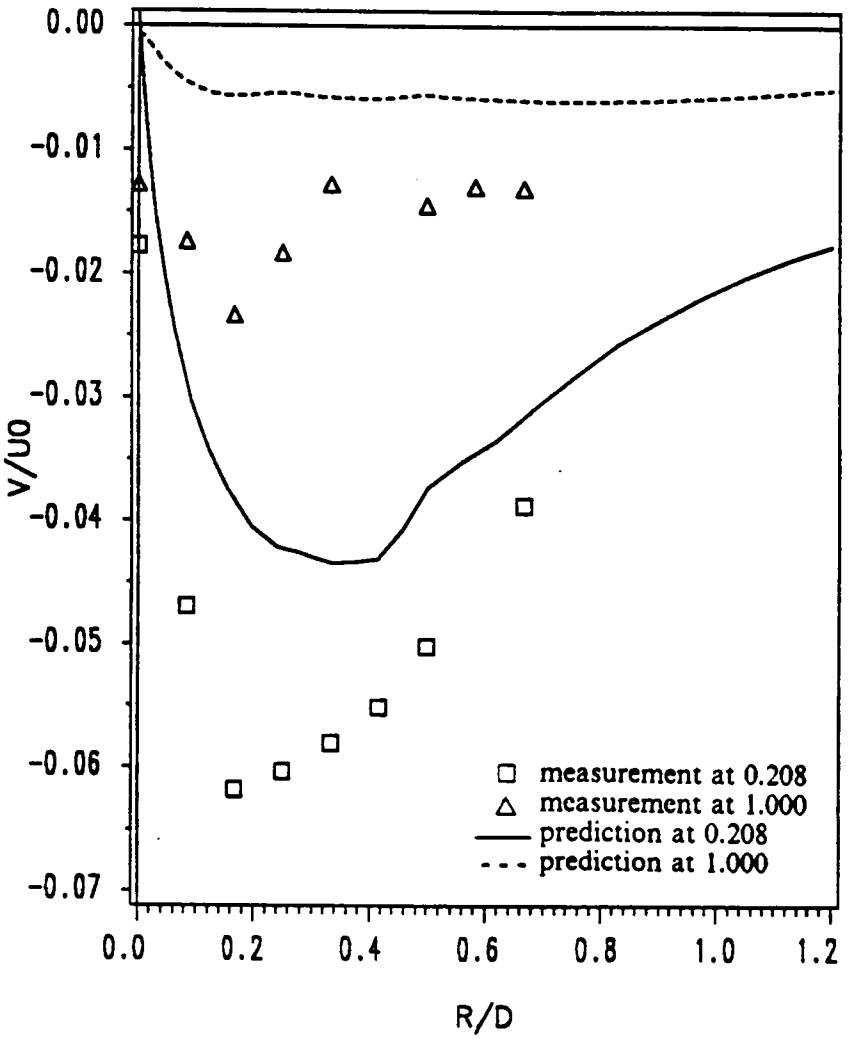

Figure 22. Self-propelled: Comparison of radial velocity profiles along radial direction at two locations, x/D = 0.208 and 1.0.

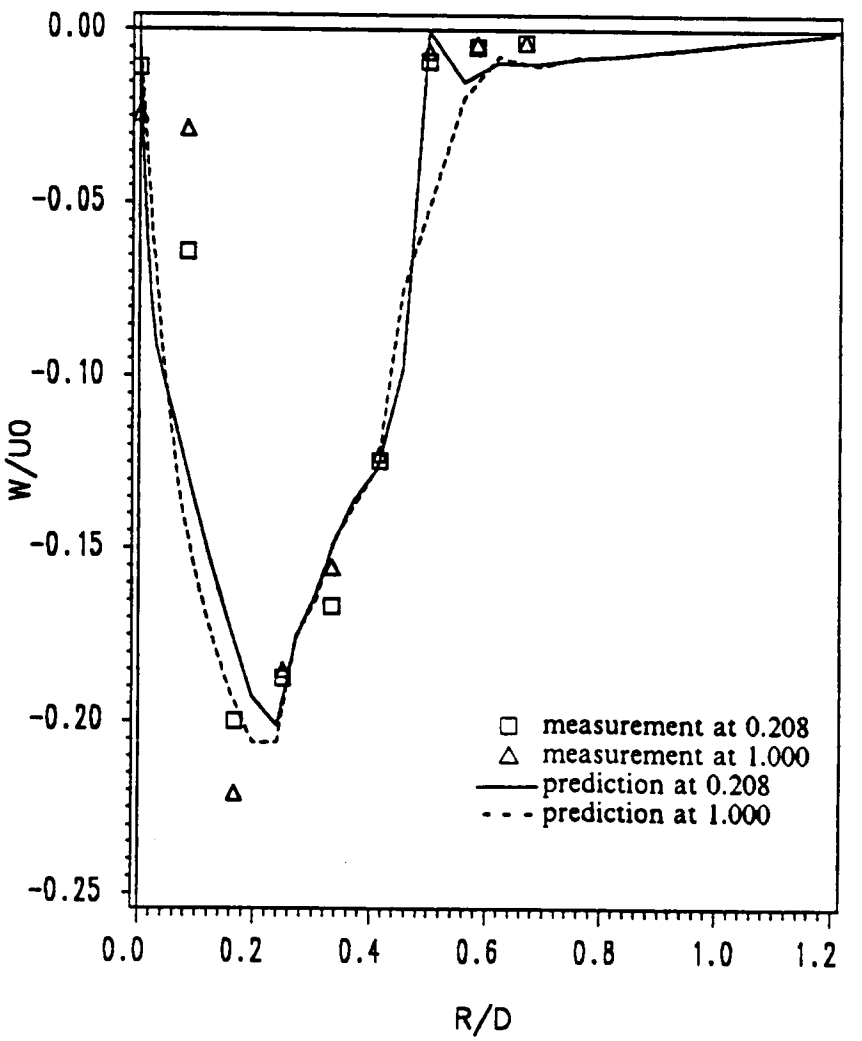

Figure 23. Self-propelled: Comparison of swirl profiles along radial direction at two locations, x/D = 0.208 and 1.0.

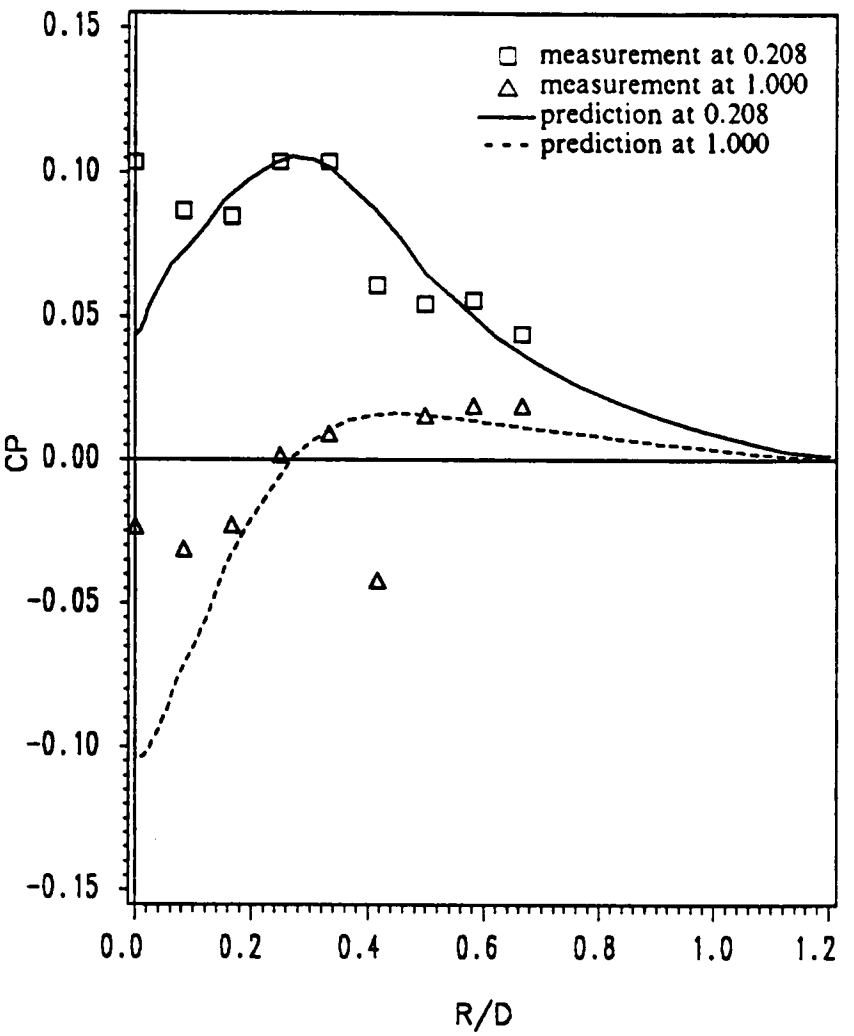

Figure 24. Self-propelled: Comparison of pressure coefficient profiles along radial direction at two locations, x/D = 0.208 and 1.0.

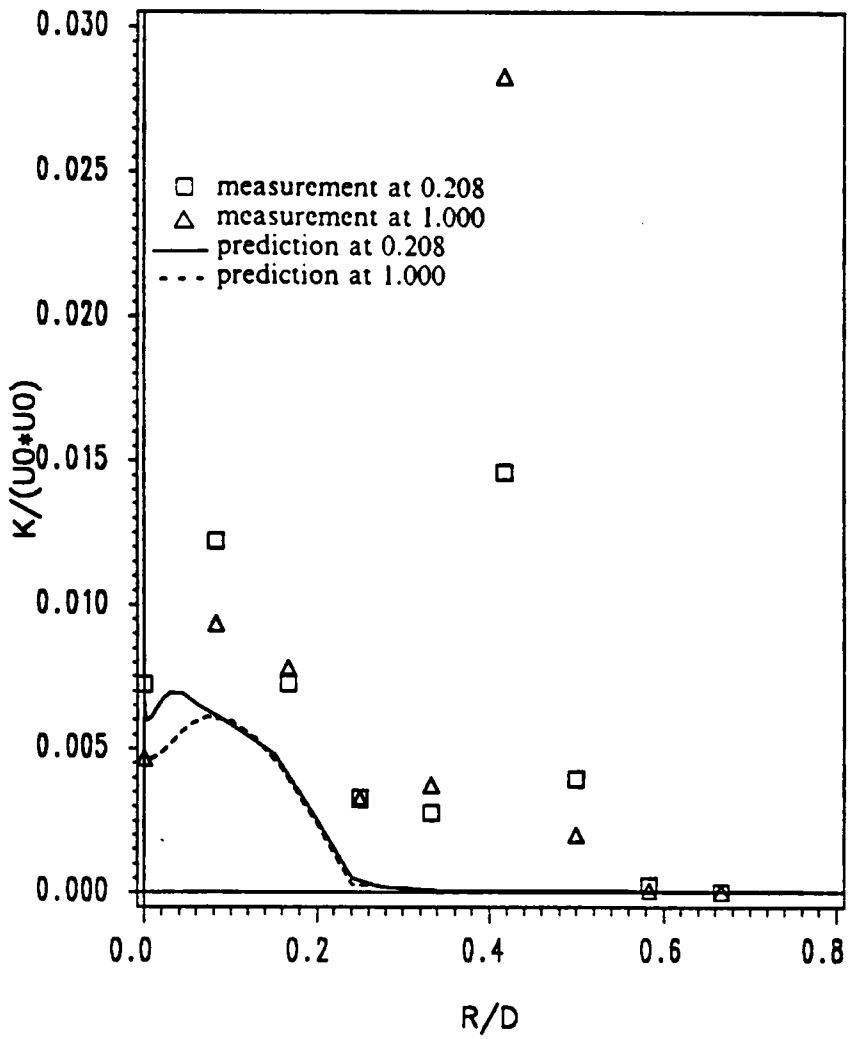

Figure 25. Self-propelled: Comparison of turbulent kinetic energy profiles along radial direction at two locations, x/D = 0.208 and 1.0.

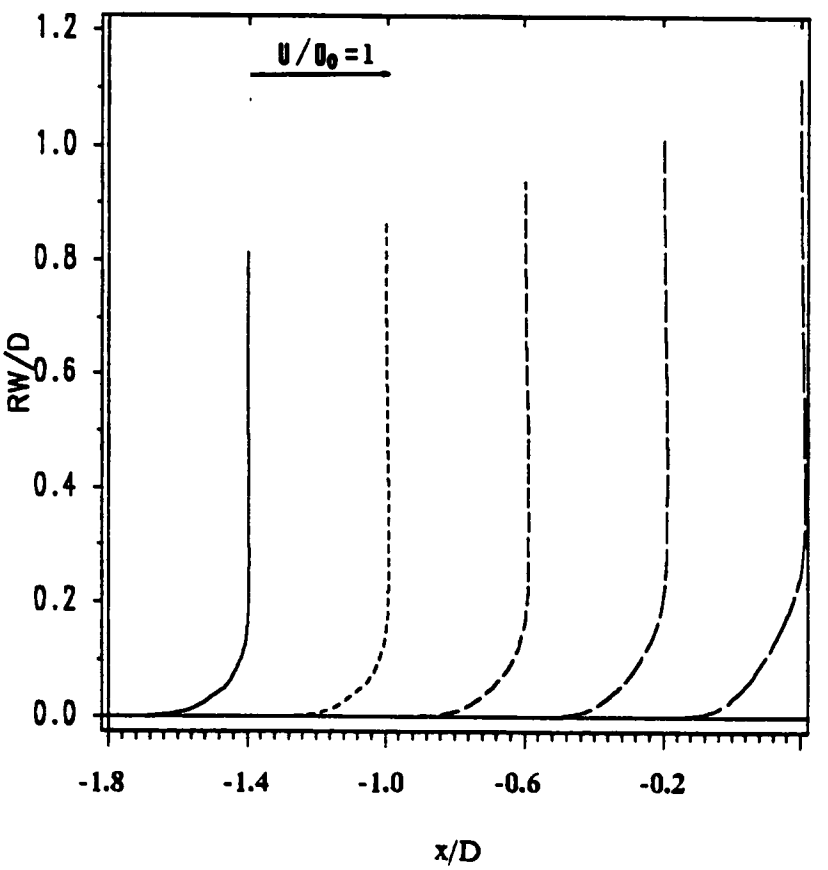

Figure 26. Self-propelled: Prediction of axial velocity profiles in the boundary layer at five locations, x/D = -1.8, -1.4, -1.0, -0.6, and -0.2, on the body surface.

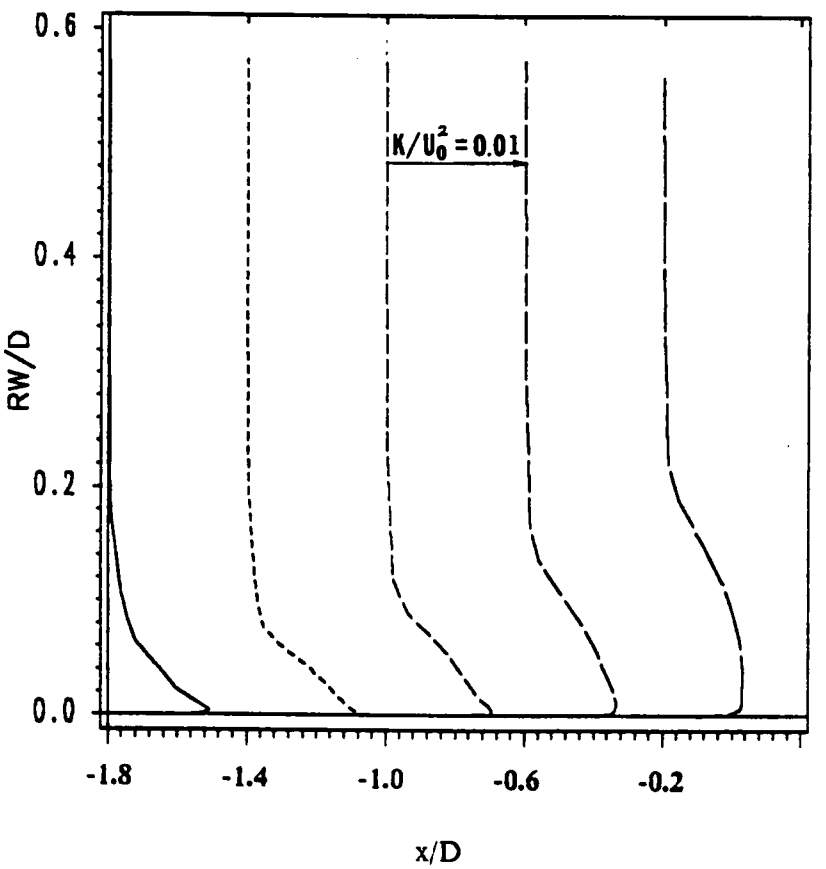

Figure 27. Self-propelled: Prediction of turbulent kinetic energy profiles in the boundary layer at five locations, x/D = -1.8, -1.4, -1.0, -0.6, and -0.2, on the body surface.

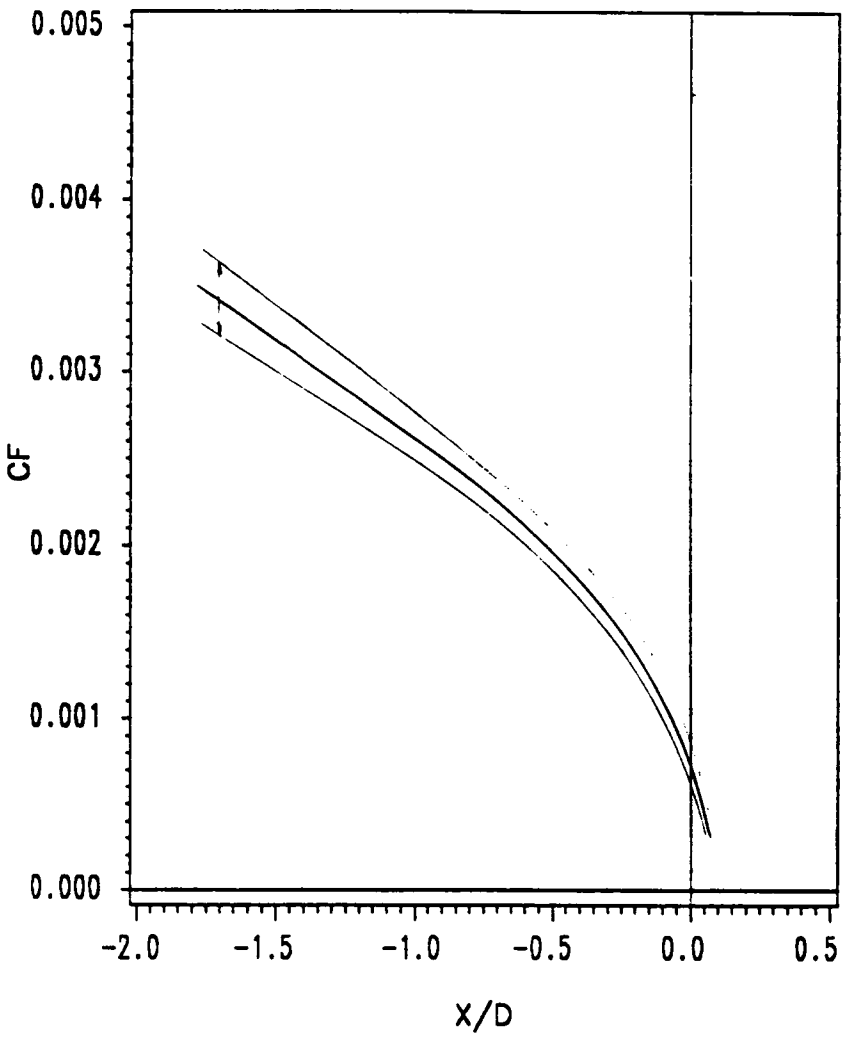

Figure 28. Self-propelled: Prediction of friction coefficient on body surface.

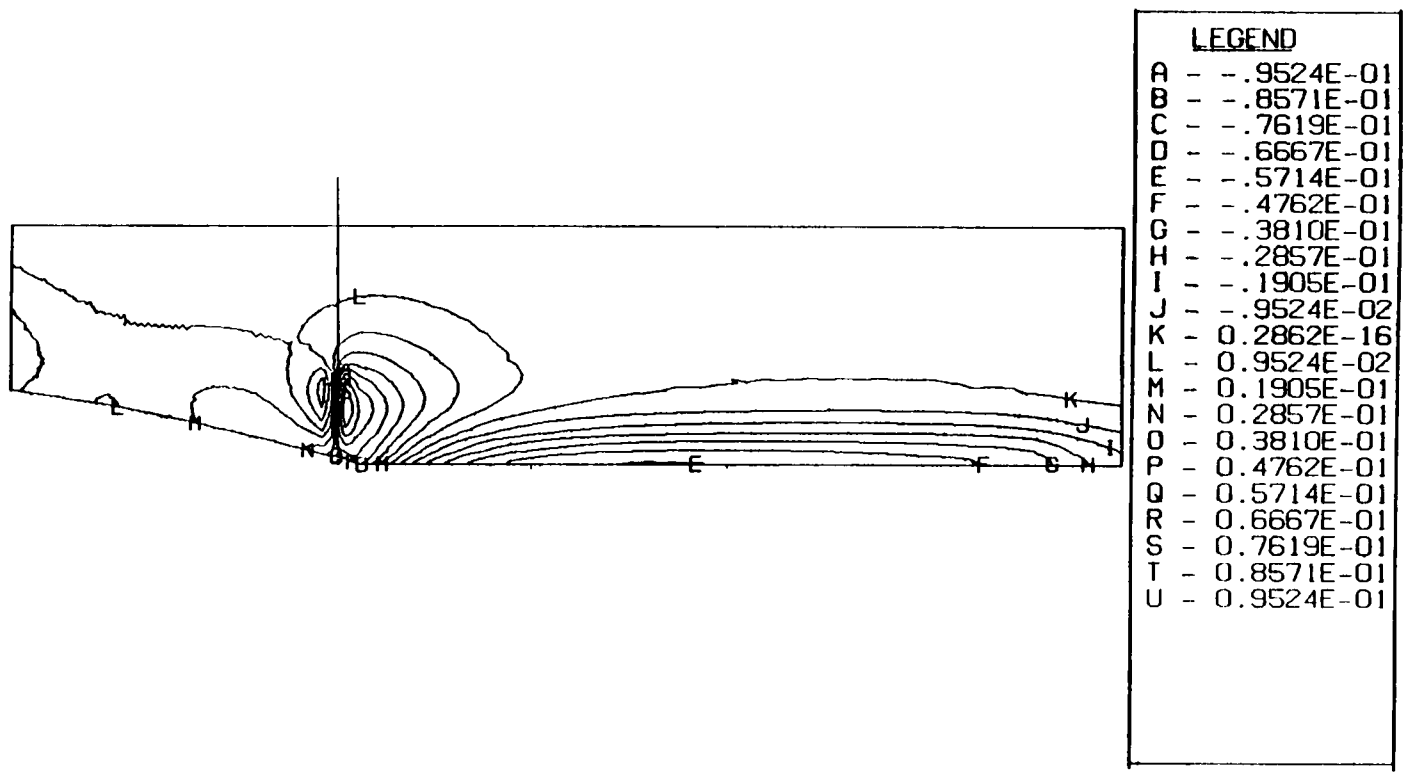

Figure 29. Self-propelled: Pressure contours.

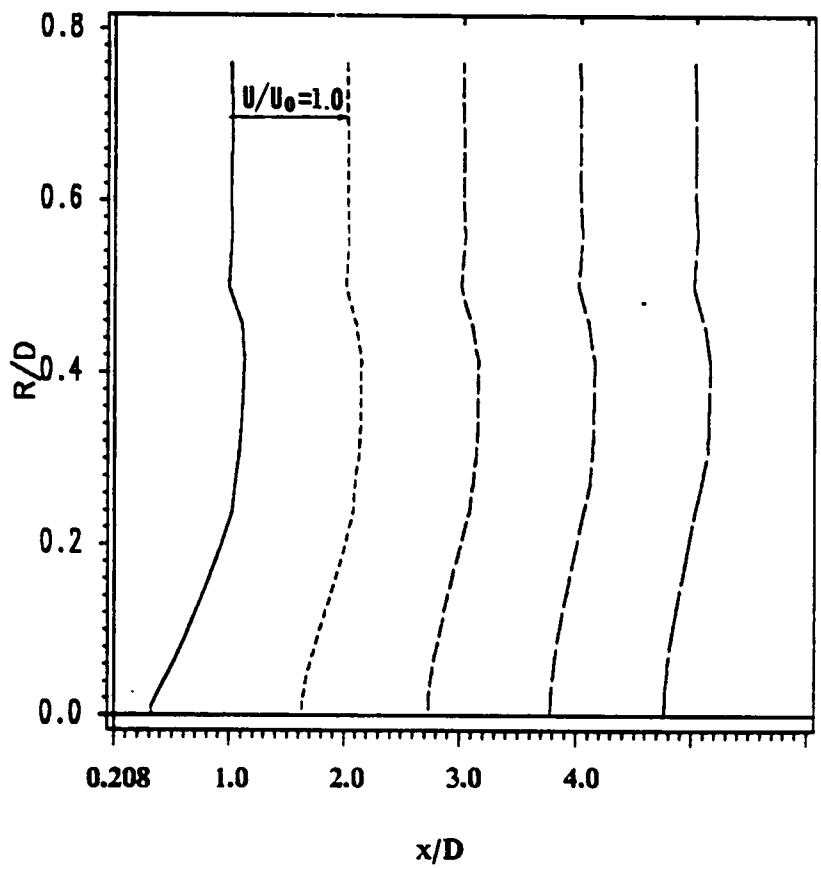

Figure 30. Self-propelled: Prediction of axial velocity profiles along radial direction at five locations, x/D = 0.208, 1.0, 2.0, 3.0, 4.0, downsteam of propeller.

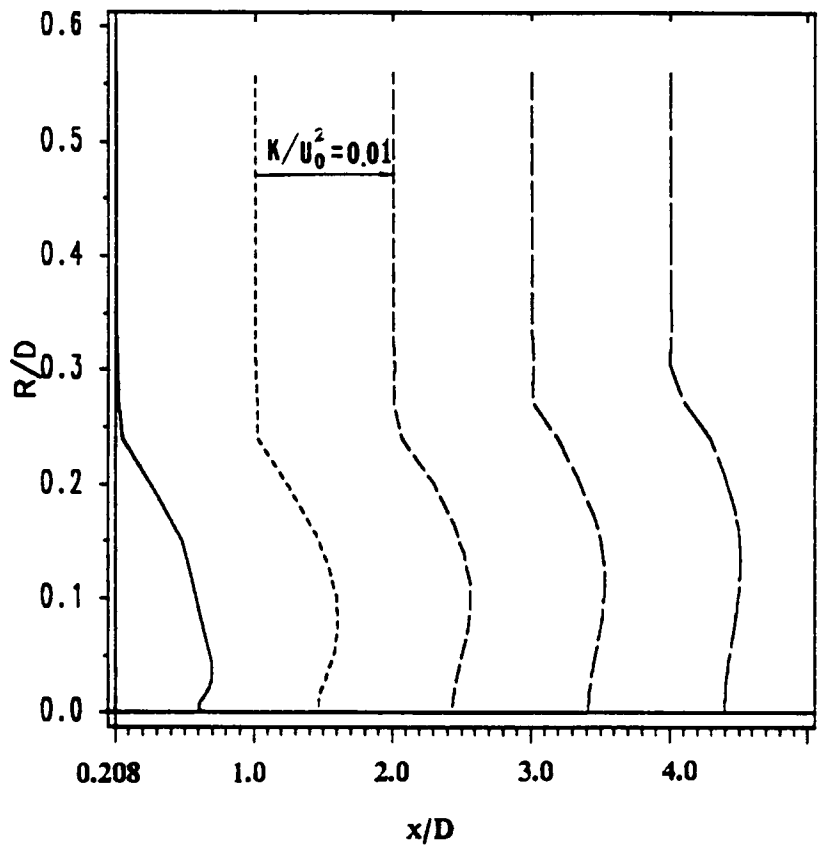

Figure 31. Self-propelled: Prediction of turbulent kinetic energy profiles along radial direction at five locations, x/D = 0.208, 1.0, 2.0, 3.0, 4.0, downsteam of propeller.

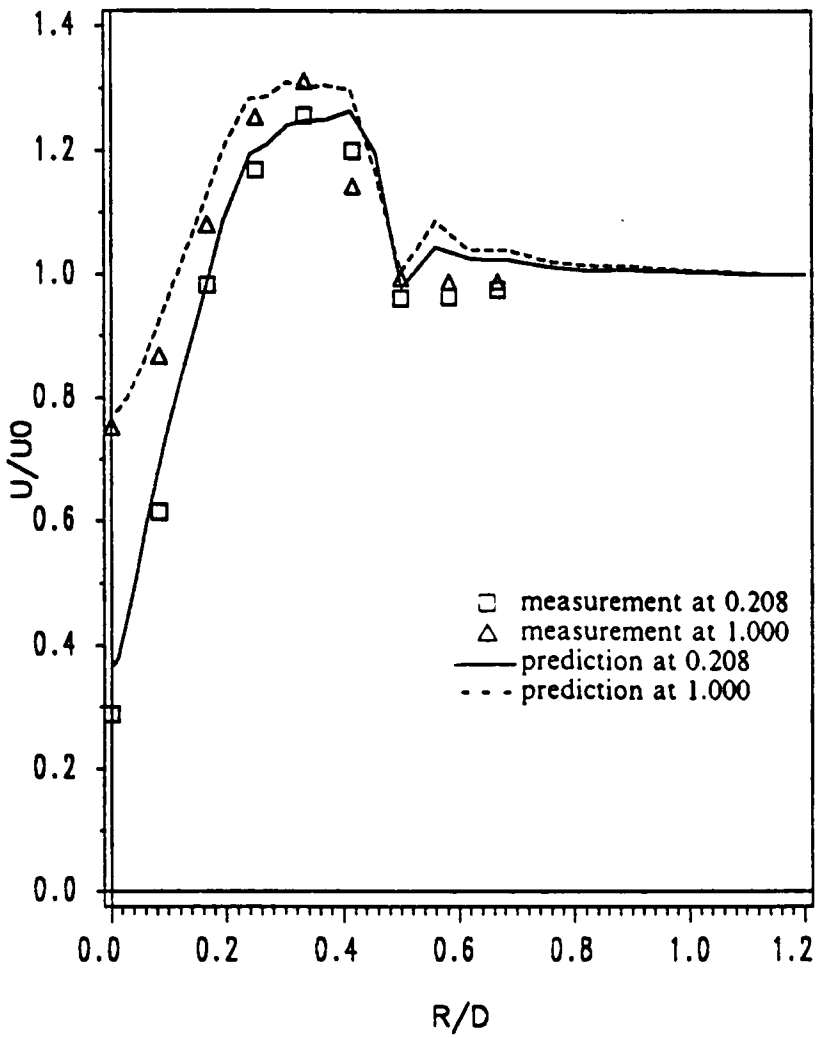

Figure 32. Over-thrusted: Comparison of axial velocity profiles along radial direction at two locations, x/D = 0.208 and 1.0.

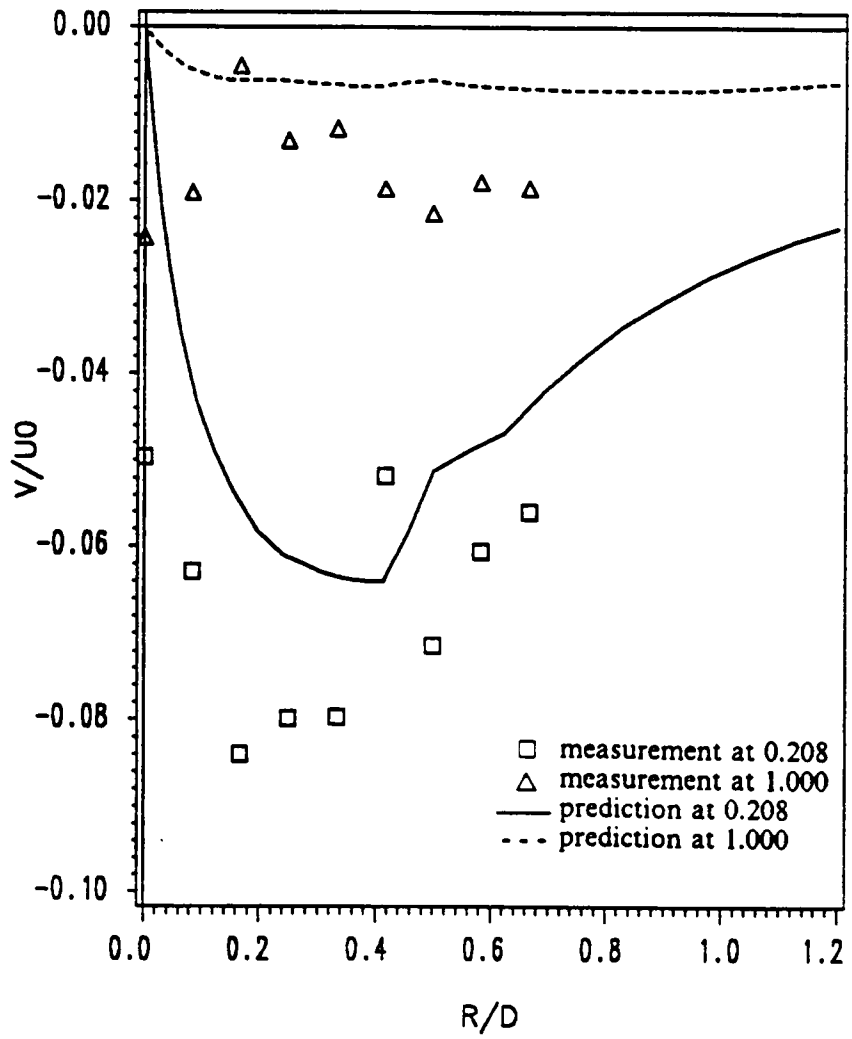

Figure 33. Over-thrusted: Comparison of radial velocity profiles along radial direction at two locations, x/D = 0.208 and 1.0.

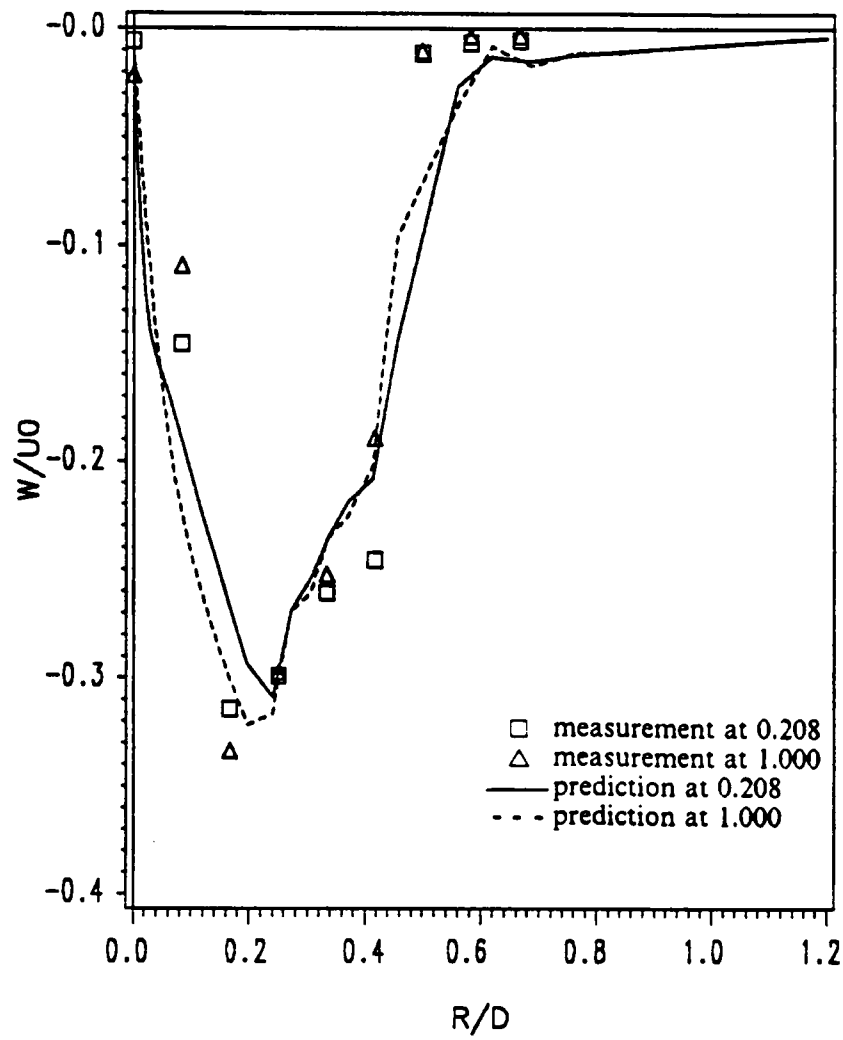

Figure 34. Over-thrusted: Comparison of swirl profiles along radial direction at two locations, x/D = 0.208 and 1.0.

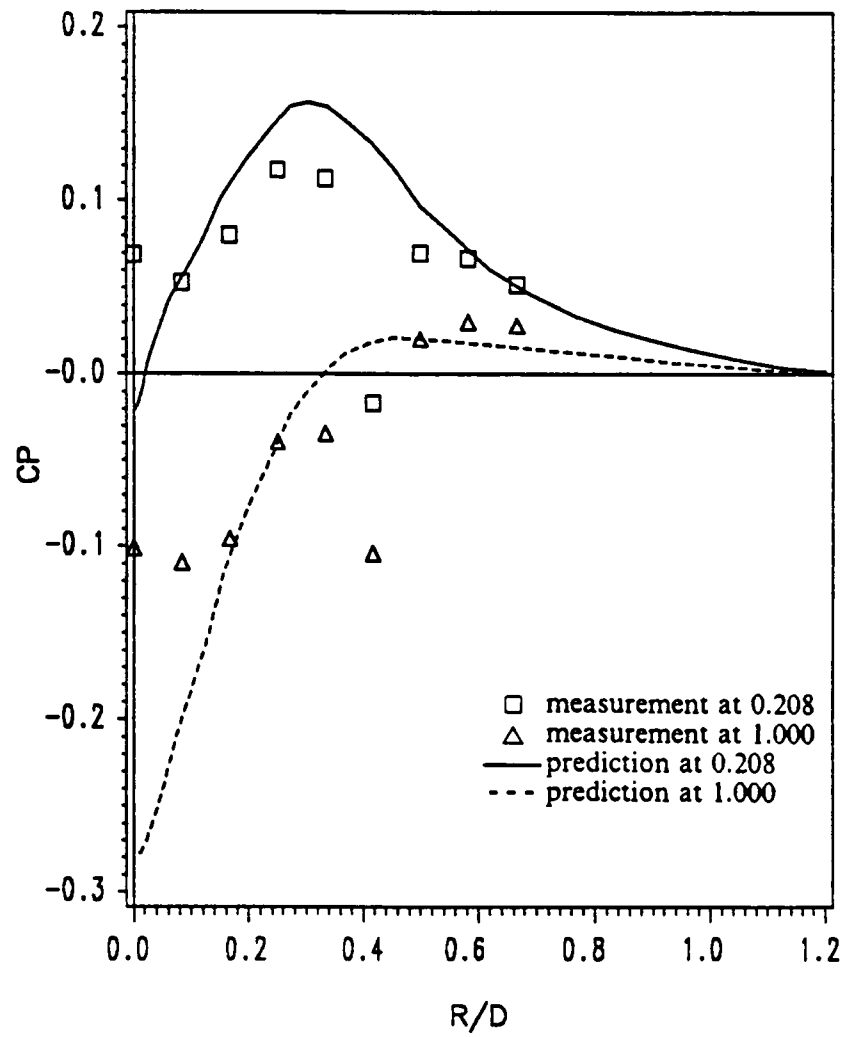

Figure 35. Over-thrusted: Comparison of pressure coefficient profiles along radial direction at two locations, x/D = 0.208 and 1.0.

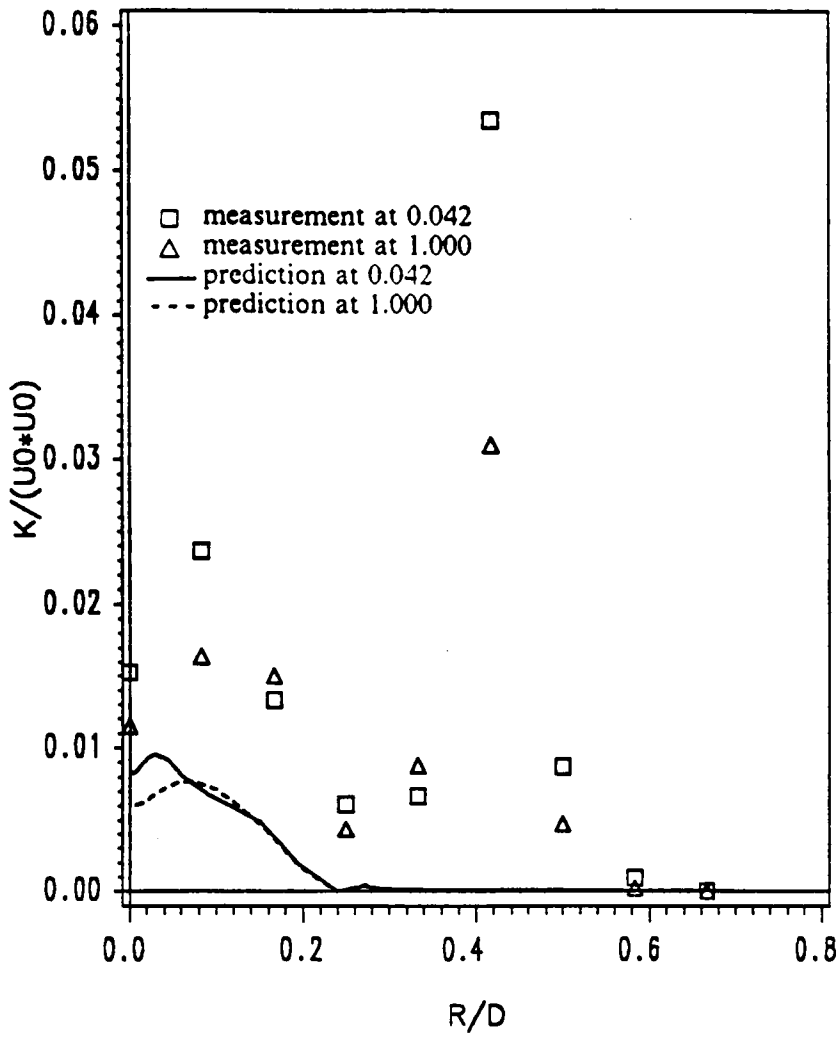

Figure 36. Over-thrusted: Comparison of turbulent kinetic energy profiles along radial direction at two locations, x/D = 0.208 and 1.0.

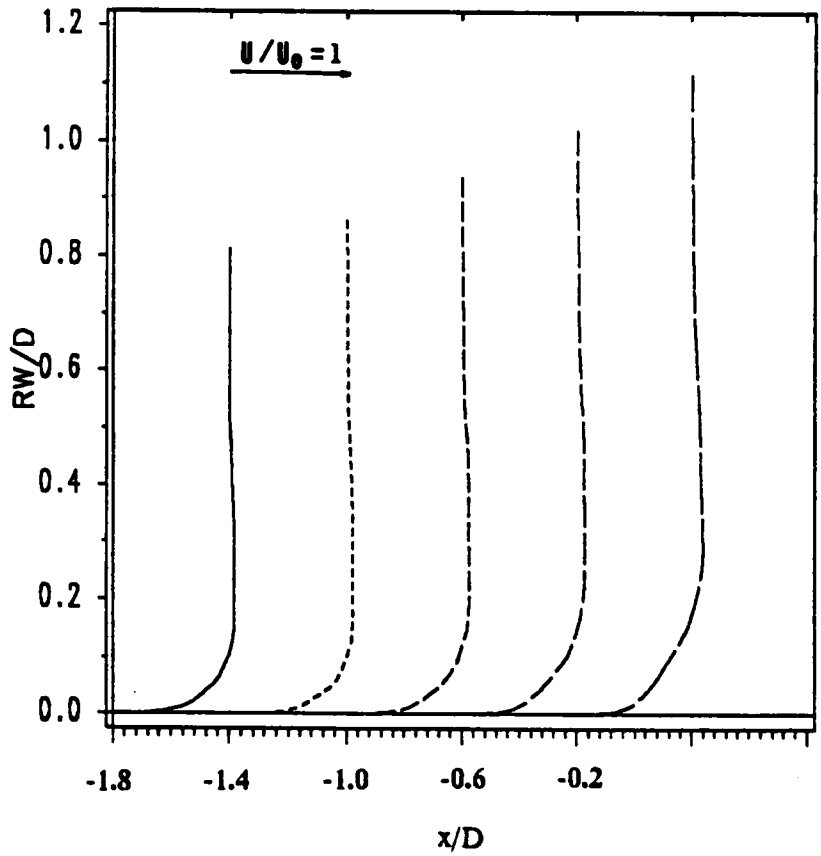

Figure 37. Over-thrusted: Prediction of axial velocity profiles in the boundary layer at five locations, x/D = -1.8, -1.4, -1.0, -0.6, and -0.2, on the body surface.

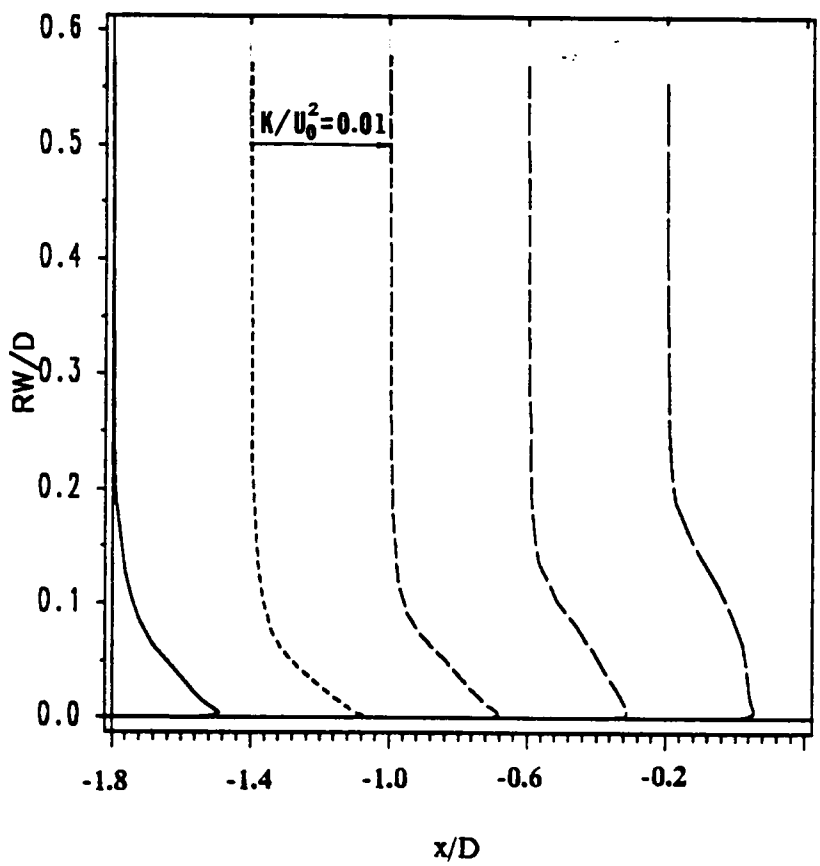

Figure 38. Over-thrusted: Prediction of turbulent kinetic energy profiles in the boundary layer at five locations, x/D = -1.8, -1.4, -1.0, -0.6, and -0.2, on the body surface.

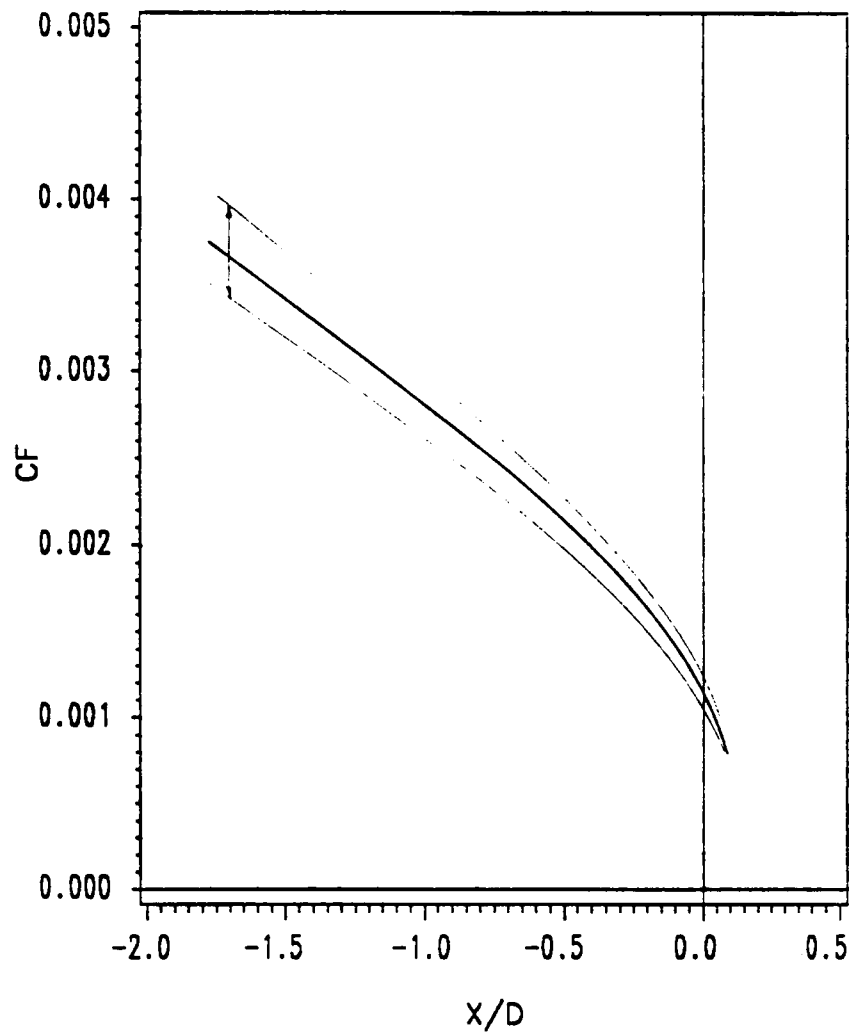

Figure 39. Over-thrusted: Prediction of skin friction coefficient on the body surface.

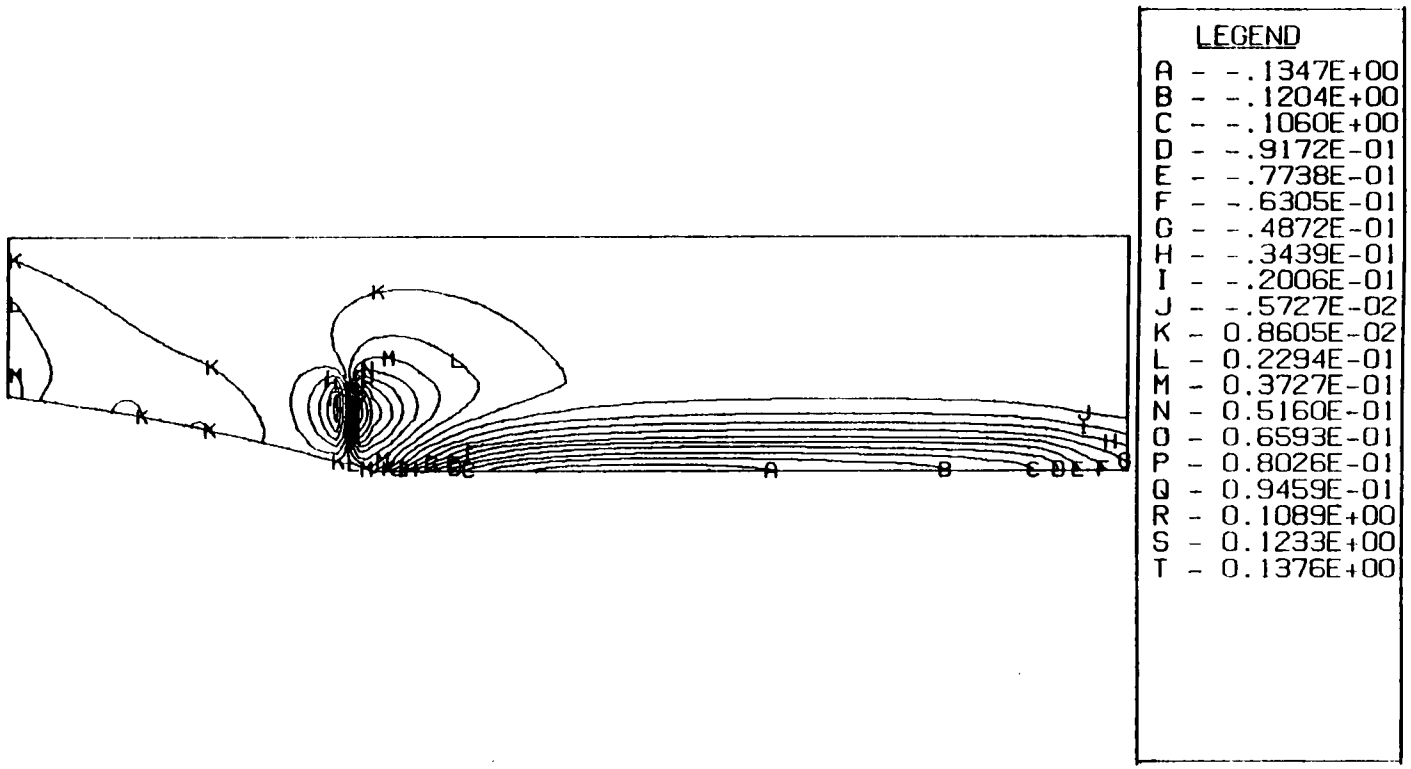

Figure 40. Over-thrusted: Pressure contours.

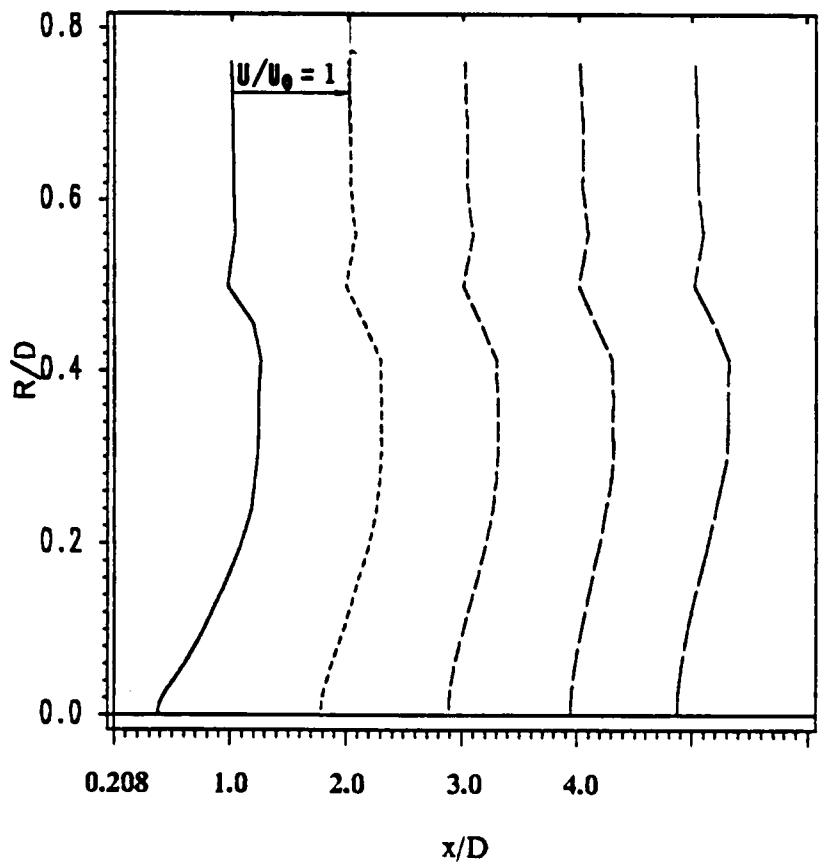

Figure 41. Over-thrusted: Prediction of axial velocity profiles along radial direction at five locations, x/D = 0.208, 1.0, 2.0, 3.0, 4.0, downstream of propeller

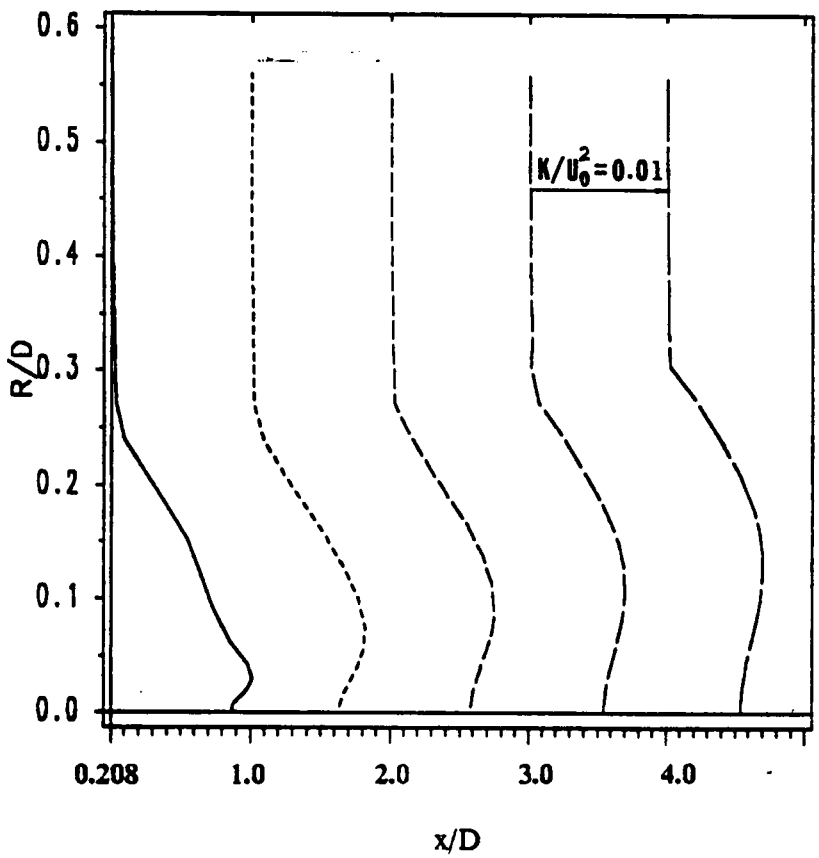

Figure 42. Over-thrusted: Prediction of turbulent kinetic energy profiles along radial direction at five locations, x/D = 0.208, 1.0, 2.0, 3.0, 4.0, downstream of proeller

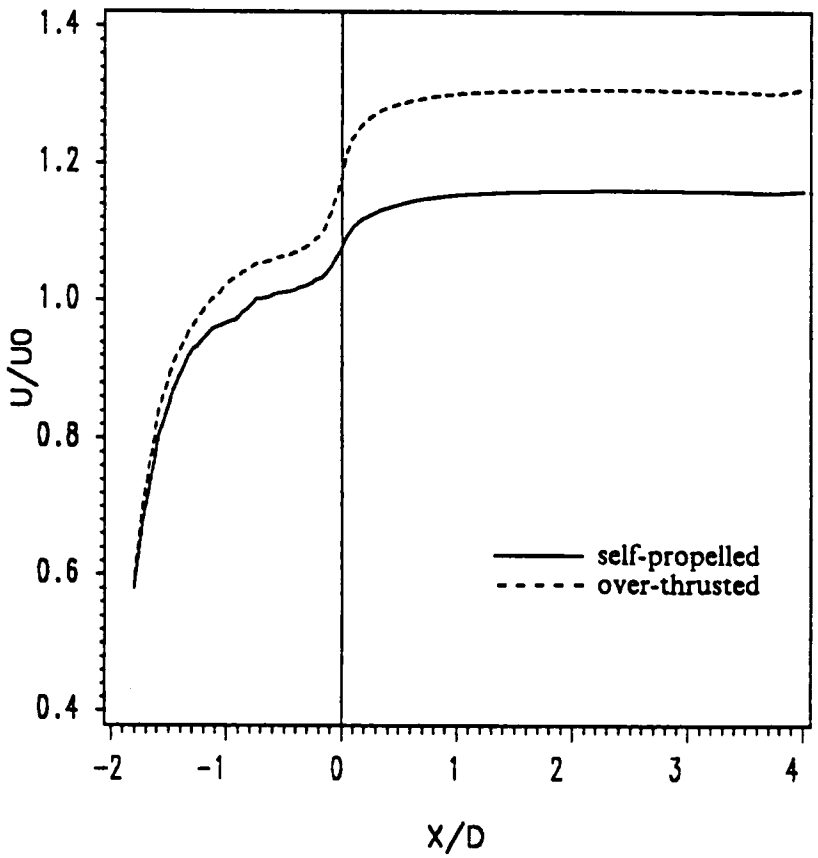

Figure 43. Self-propelled and over-thrusted: Prediction of axial velocity profile along $r/R_P = 0.8$.

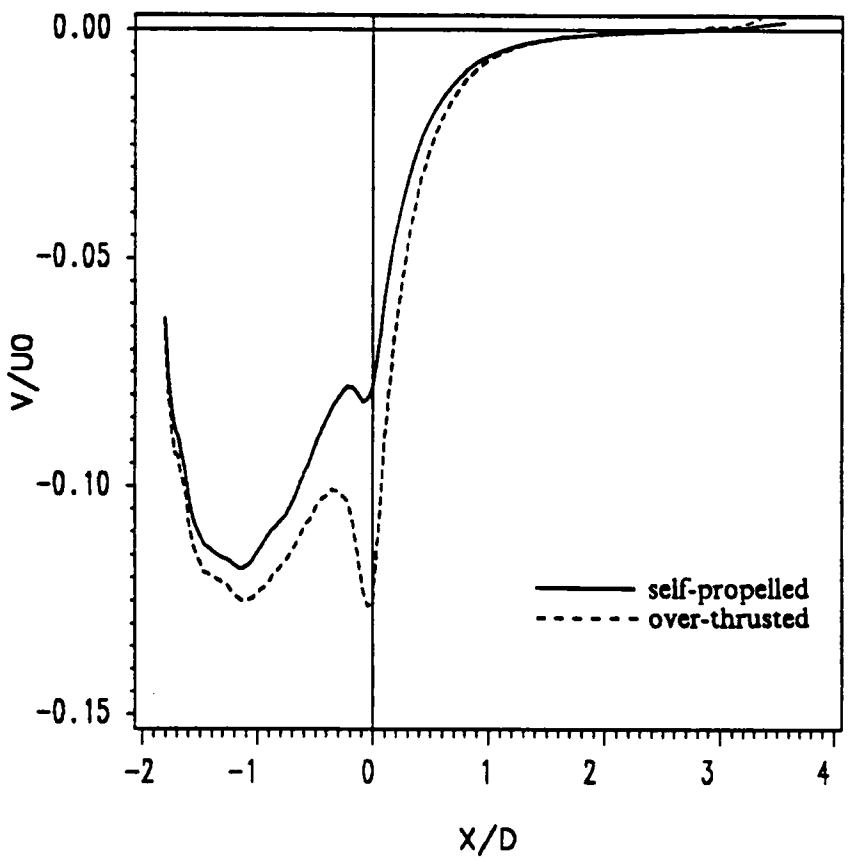

Figure 44. Self-propelled and over-thrusted: Prediction of radial velocity profile along $r/R_P = 0.8$.

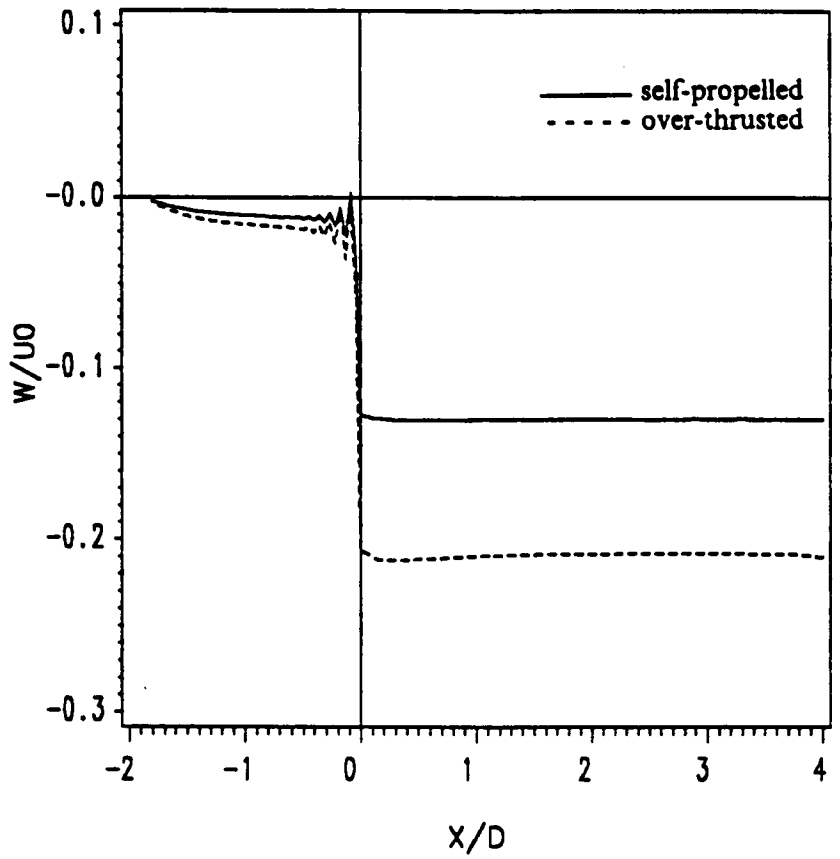

Figure 45. Self-propelled and over-thrusted: Prediction of swirl velocity profile along $r/R_P = 0.8$.

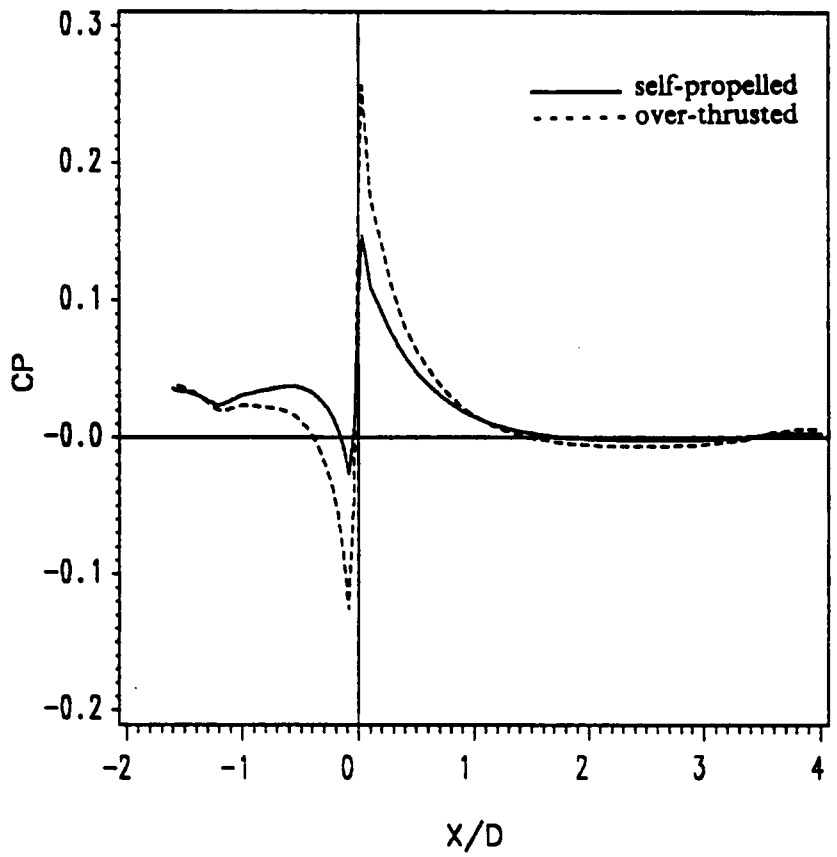

Figure 46. Self-propelled and over-thrusted: Prediction of pressure coefficient profile along $r/R_P = 0.8$.

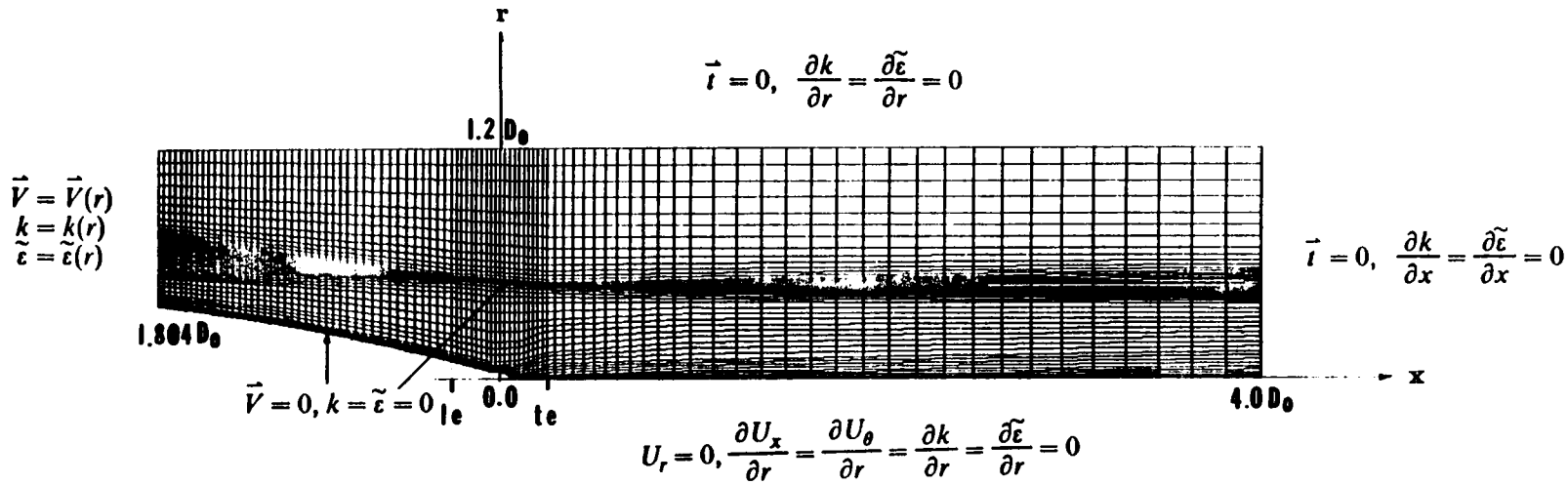

Figure 47. Ducted propeller: Generated mesh and boundary conditions.

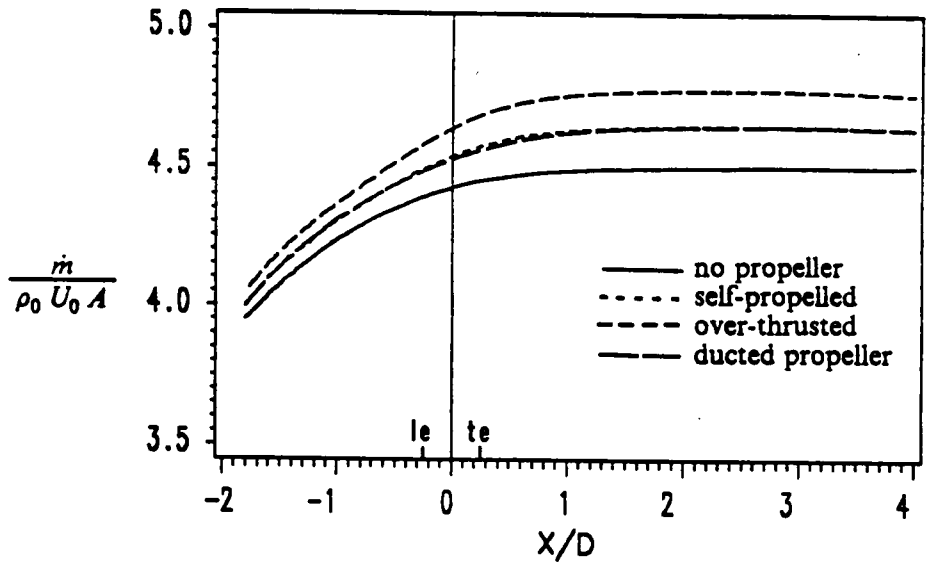

(a) mass flow rate

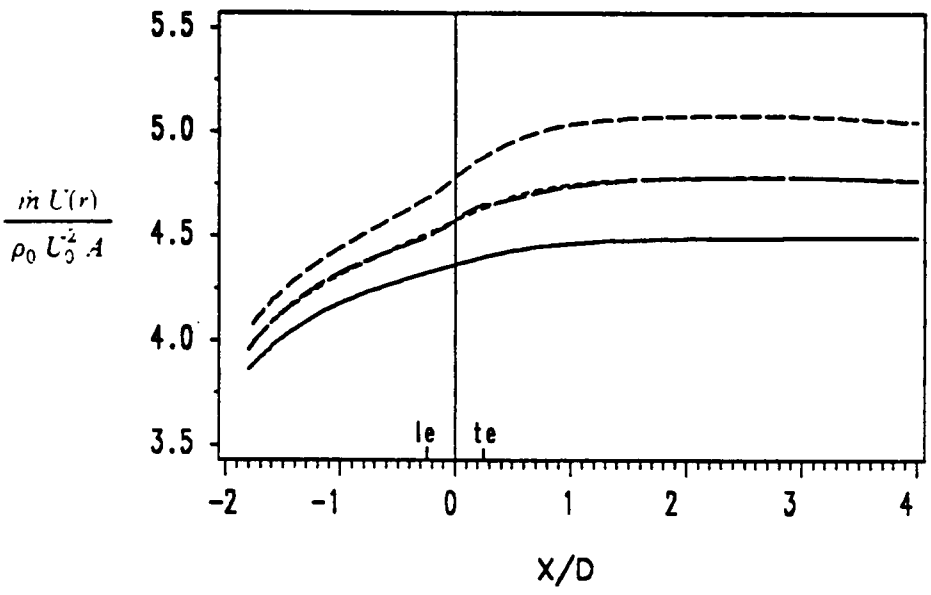

(b) momtum flux

Figure 48. Ducted propeller: Comparison of mass flow rate and momentum flux through a circular cross section of radius $1.2D_0$ for the non-propelled, self-propelled, over-thrusted, and ducted propeller cases.

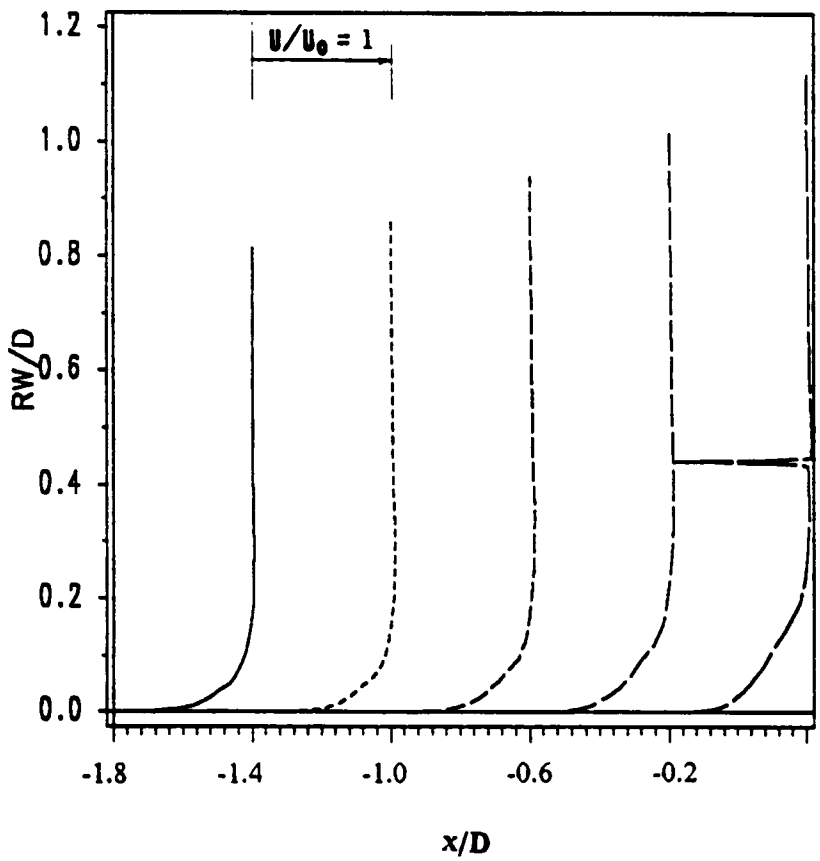

Figure 49. Ducted propeller: Prediction of axial velocity profiles in the boundary layer at five locations, x/D = -1.8, -1.4, -1.0, -0.6, and -0.2, on the body surface.

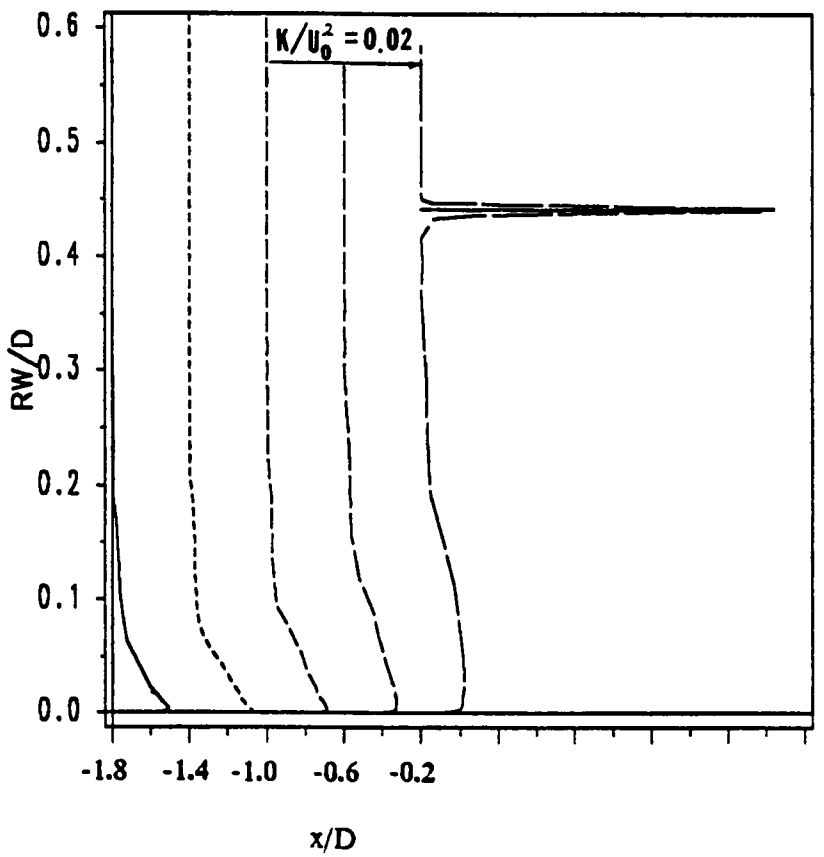

Figure 50. Ducted propeller: Prediction of the turbulent kinetic energy profiles in the boundary layer at five locations, x/D = -1.8, -1.4, -1.0, -0.6, and -0.2 on the body surface.

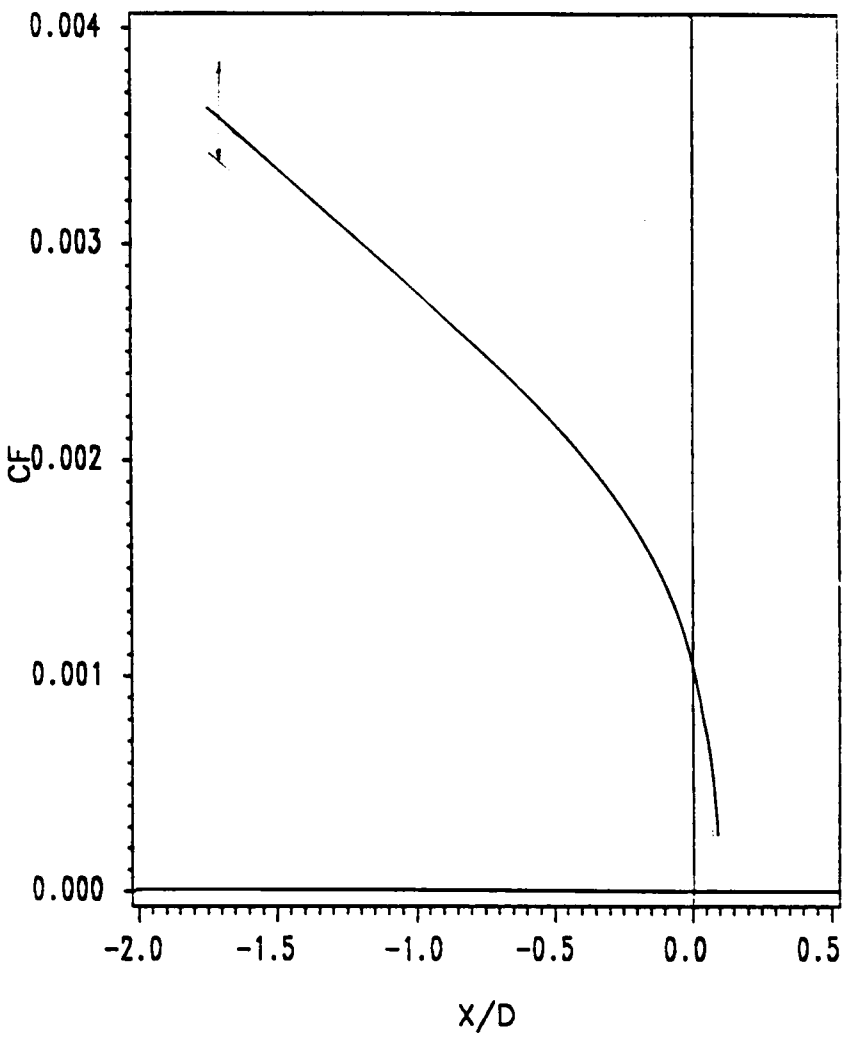

Figure 51. Ducted propeller: Prediction of friction coefficient on the slender body surface.

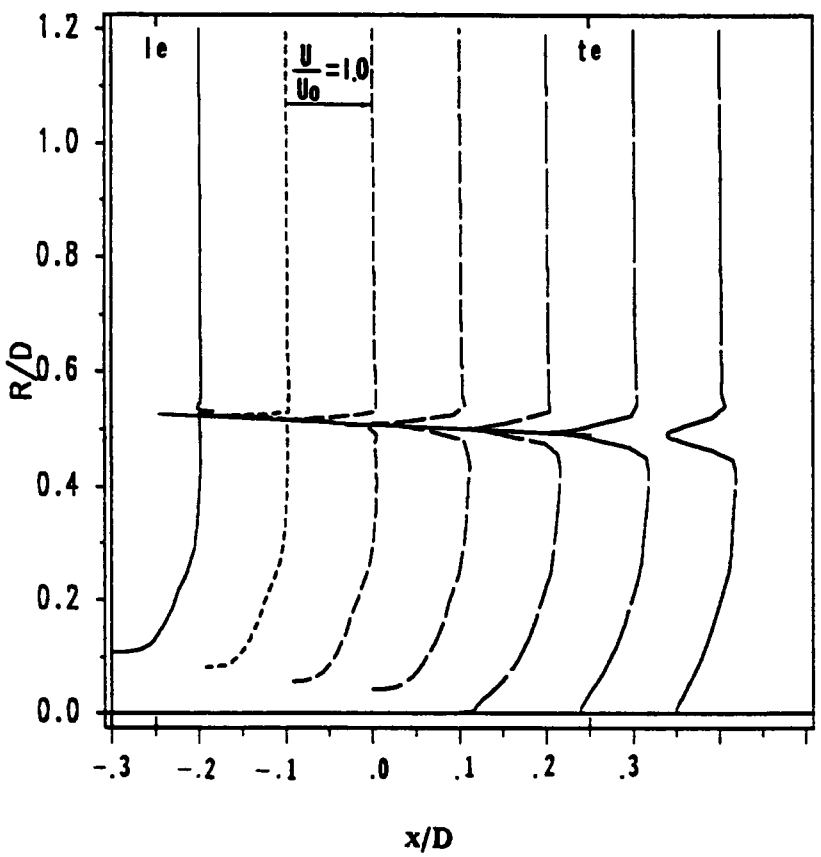

Figure 52. Ducted propeller: Prediction of axial velocity profiles around duct at seven locations, x/D = -0.3, -0.2, -0.1, 0.0, 0.1, 0.2, and 0.3.

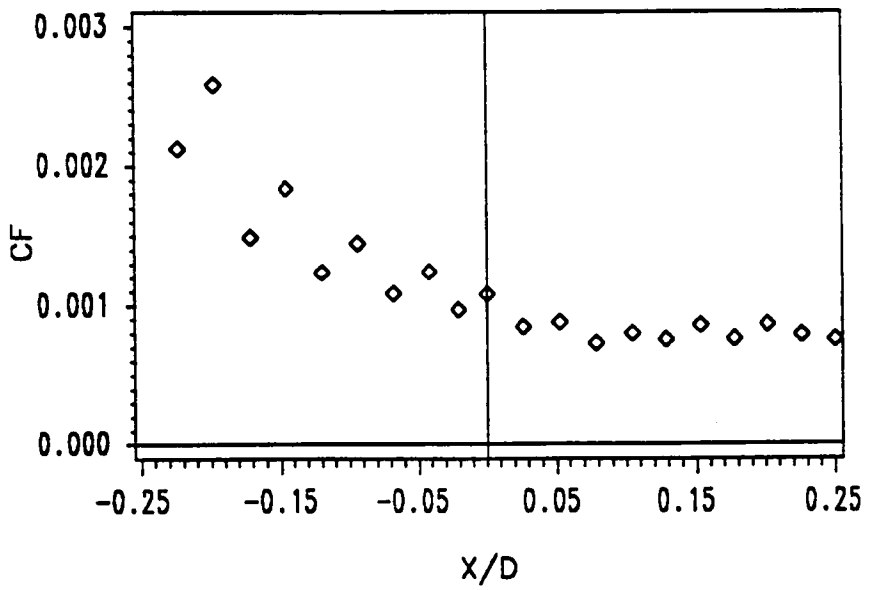

(a) outside surface

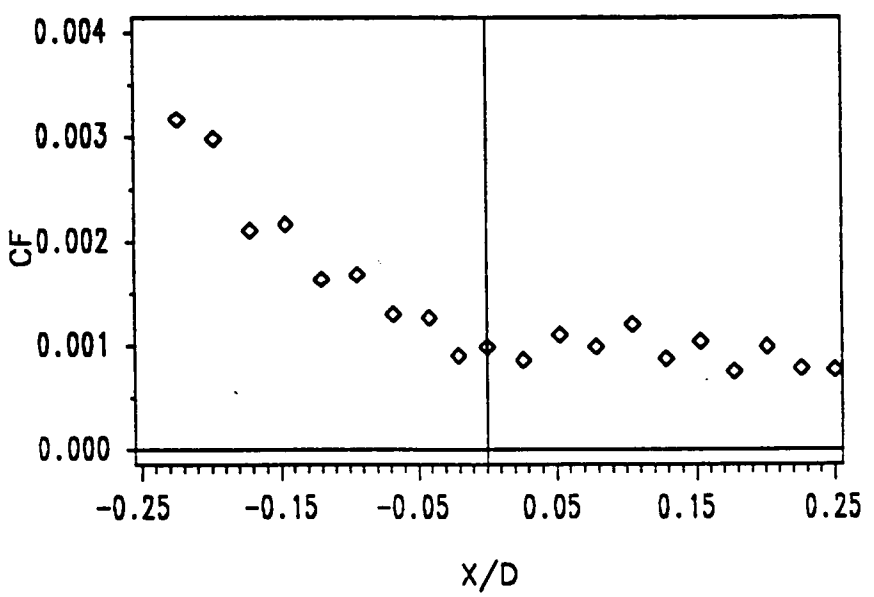

(b) inside surface

Figure 53. Ducted propeller: Prediction of the friction coefficients on the outside and inside surfaces of the duct.

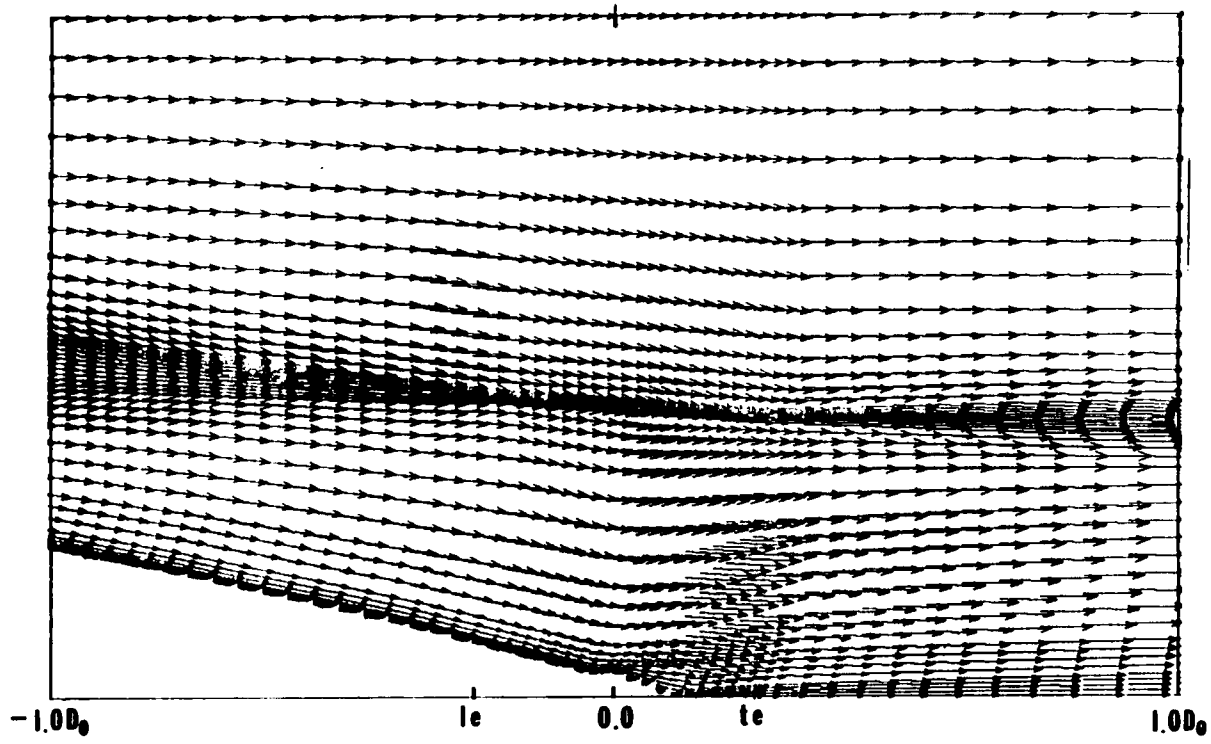

Figure 54. Ducted propeller: Predicted velocity vectors around the duct.

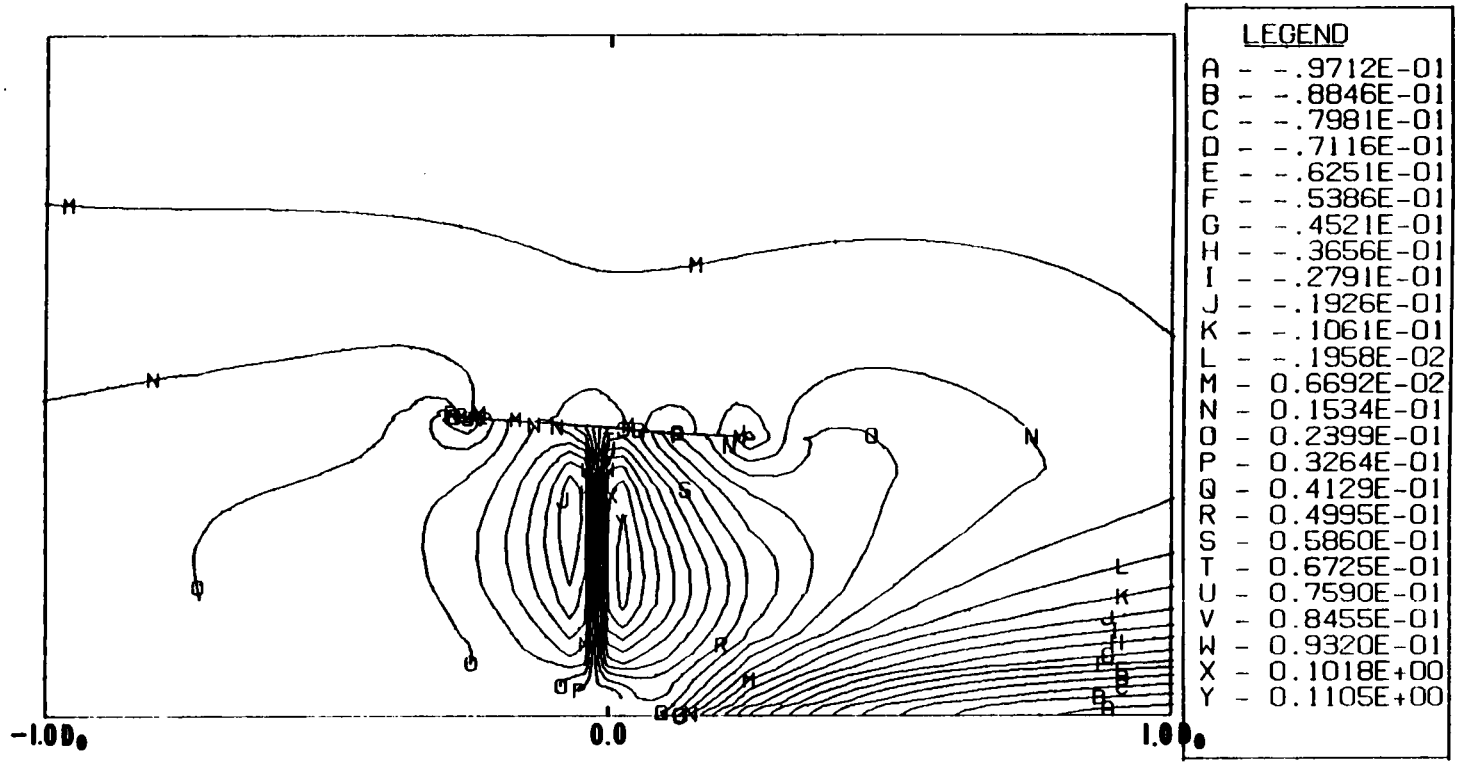

Figure 55. Ducted propeller: Predicted pressure contours around the duct.

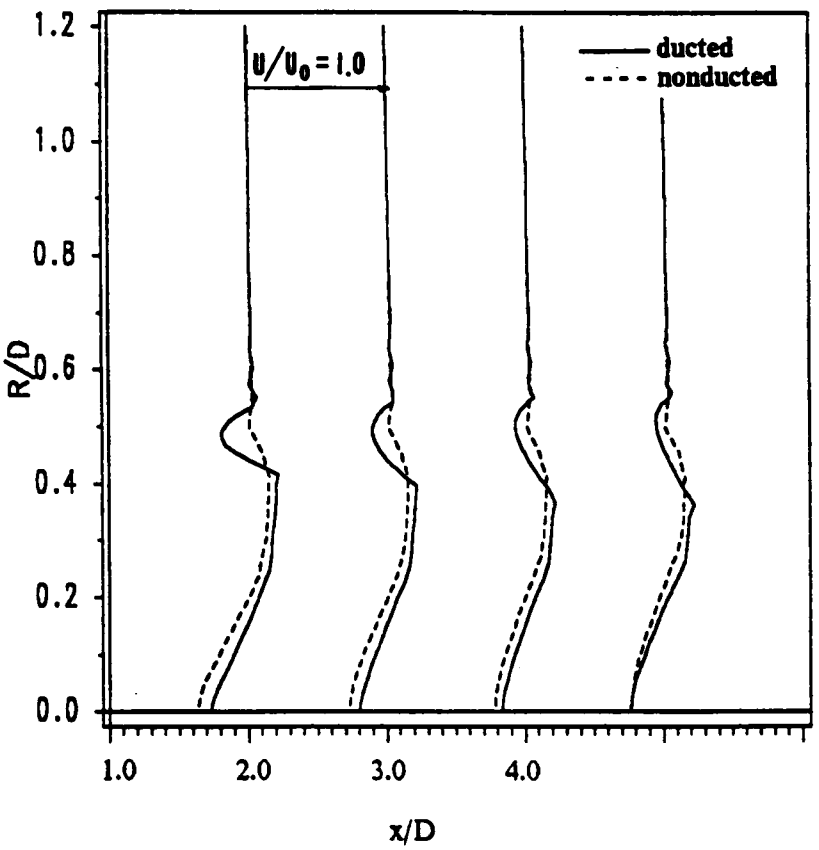

Figure 56. Ducted propeller: Prediction of axial velocity profiles along radial direction at four locations, x/D = 1.0, 2.0, 3.0, and 4.0, downstream of propeller.

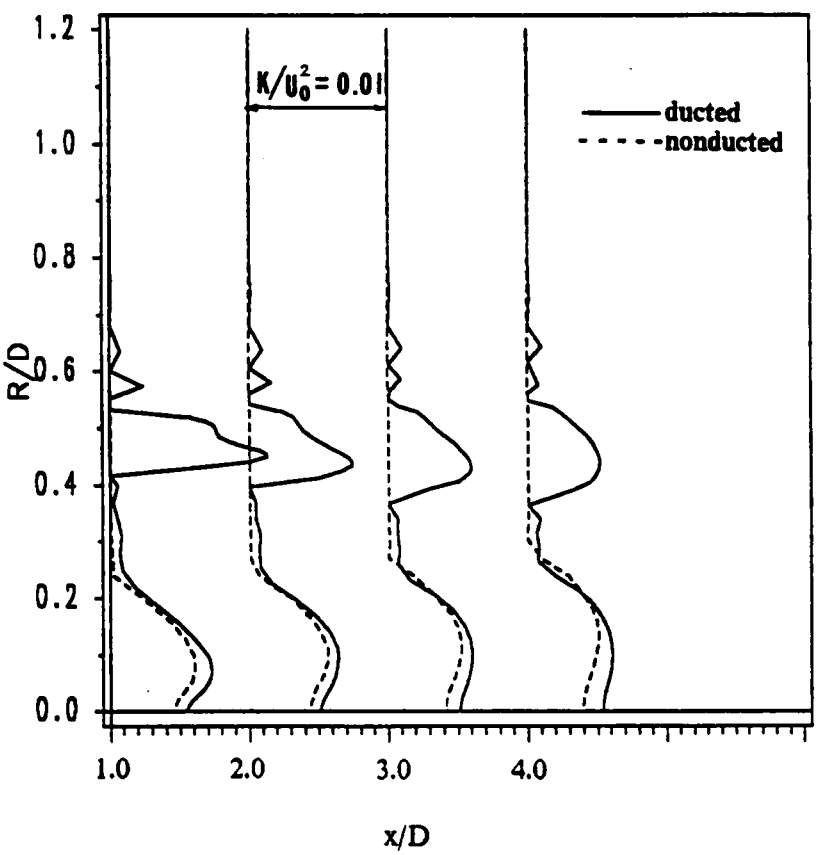

Figure 57. Ducted propeller: Prediction of turbulent kinetic energy profiles along radial direction at four locations, x/D = 1.0, 2.0, 3.0, and 4.0, downstream of propeller.

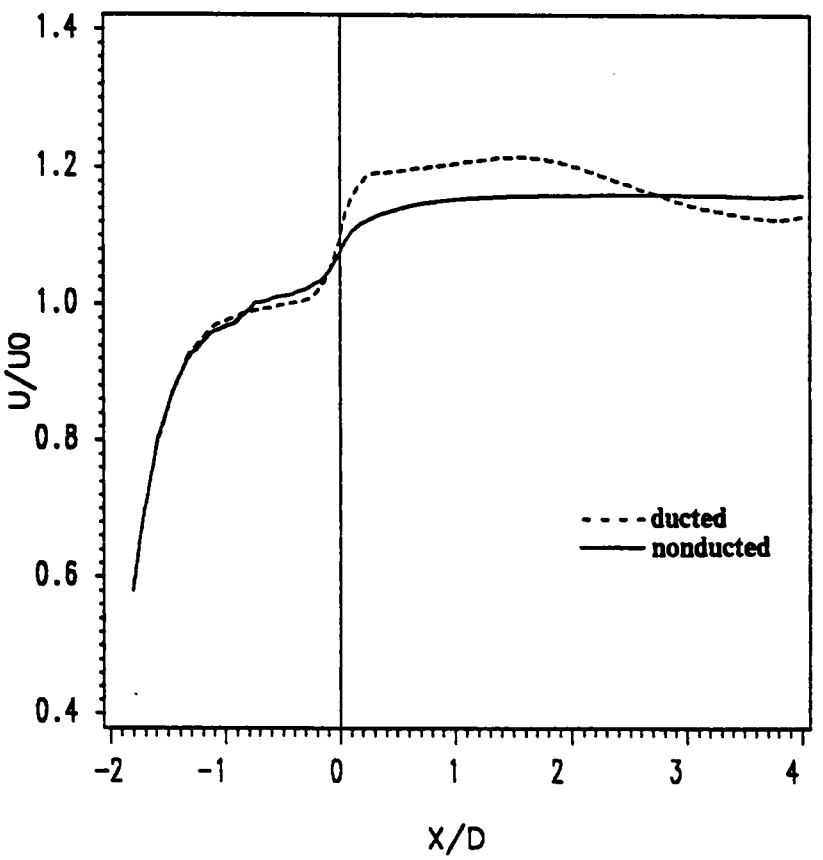

Figure 58. Ducted propeller: Comparison of axial velocity profiles along $r/R_p = 0.8$ for the ducted and nonducted propeller at the self-propelled condition.

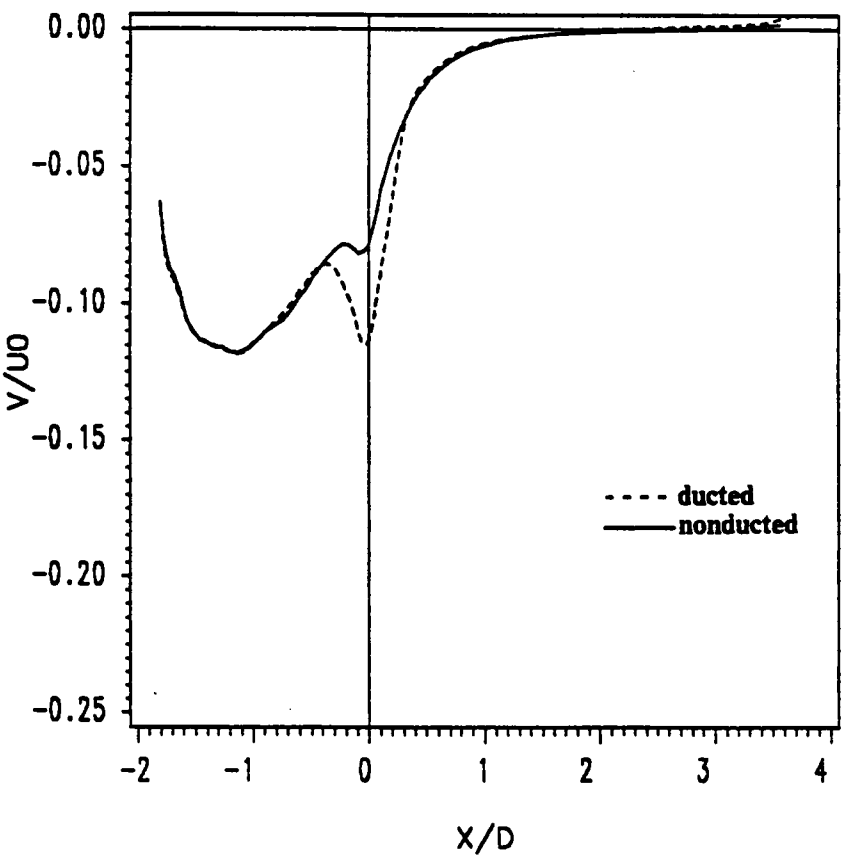

Figure 59. Ducted propeller: Comparison of radial velocity profiles along $r/R_p = 0.8$ for the ducted and nonducted propeller at the self-propelled condition.

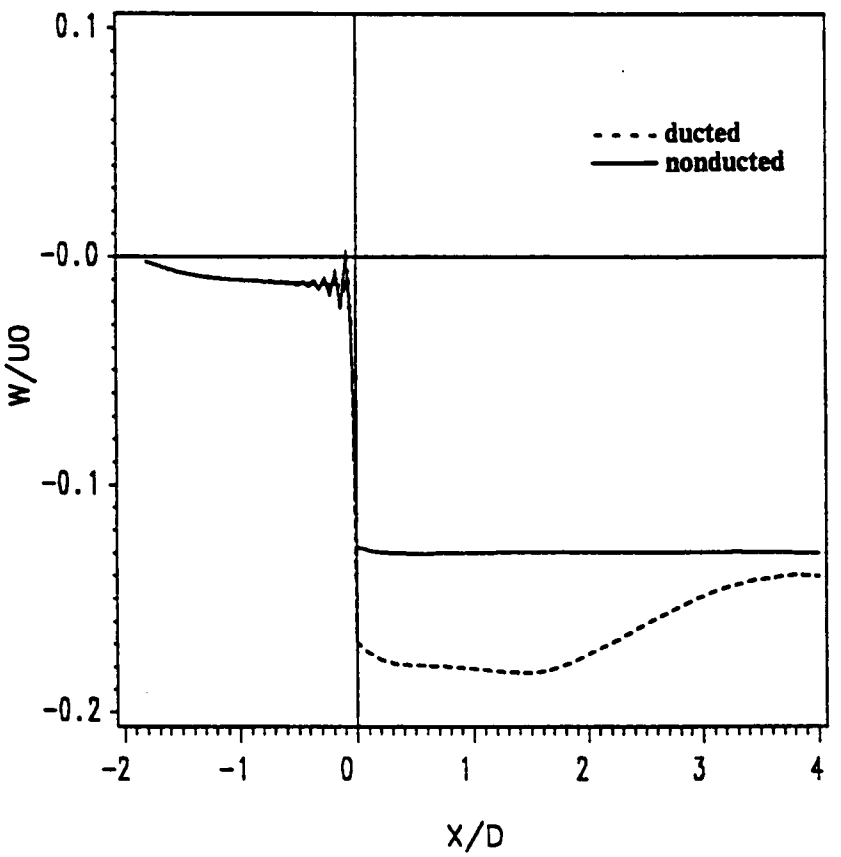

Figure 60. Ducted propeller: Comparison of swirl velocity profiles along $r/R_p = 0.8$ for the ducted and nonducted propeller at the self-propelled condition.

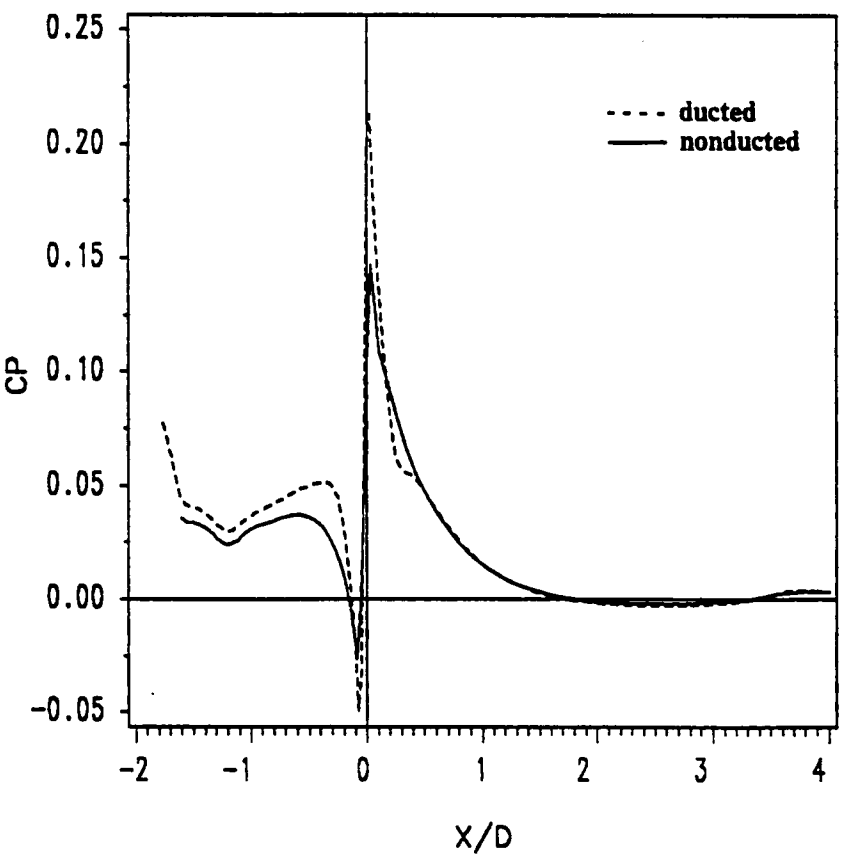

Figure 61. Ducted propeller: Comparison of pressure coefficient profiles along $r/R_p = 0.8$ for the ducted and nonducted propeller at the self-propelled condition.

The vita has been removed from the scanned document